Aus dem
Deutschen Schwindel- und Gleichgewichtszentrum, DSGZ,
und der Neurologischen Klinik und Poliklinik
der Ludwig-Maximilians-Universität München

Direktor: Prof. Dr. Marianne Dieterich

Diagnostik episodischer Schwindelsyndrome: Innenohr-MRT-Bildgebung bei vestibulärer Migräne und Morbus Menière

Dissertation
zum Erwerb des Doktorgrades der Medizin
an der Medizinischen Fakultät der
Ludwig-Maximilians-Universität zu München

vorgelegt von

Johannes Quirin Gerb

aus München

2024

Mit Genehmigung der Medizinischen Fakultät
der Universität München

Berichterstatterin:	Univ. Prof. Dr. med. Marianne Dieterich, FANA, FEAN
Mitberichterstatter:	PD Dr. Kariem-N. Sharaf
	PD Dr. Dr. Robert Stahl
Mitbetreuung durch die promovierte Mitarbeiterin:	Dr. med. Valerie Kirsch
Dekan:	Prof. Dr. med. Thomas Gudermann
Tag der mündlichen Prüfung:	10.10.2024

Affidavit

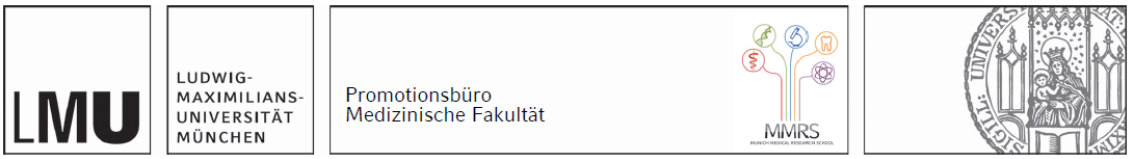

Eidesstattliche Versicherung

Gerb, Johannes

Name, Vorname

Ich erkläre hiermit an Eides statt, dass ich die vorliegende Dissertation mit dem Titel:

Diagnostik episodischer Schwindelsyndrome: Innenohr-MRT-Bildgebung bei vestibulärer Migräne und Morbus Menière

selbständig verfasst, mich außer der angegebenen keiner weiteren Hilfsmittel bedient und alle Erkenntnisse, die aus dem Schrifttum ganz oder annähernd übernommen sind, als solche kenntlich gemacht und nach ihrer Herkunft unter Bezeichnung der Fundstelle einzeln nachgewiesen habe.

Ich erkläre des Weiteren, dass die hier vorgelegte Dissertation nicht in gleicher oder in ähnlicher Form bei einer anderen Stelle zur Erlangung eines akademischen Grades eingereicht wurde.

München, 10.10.2024 — Johannes Gerb

Ort, Datum — Unterschrift Doktorandin bzw. Doktorand

Inhaltsverzeichnis

Abkürzungsverzeichnis

2D	zweidimensional
3D	dreidimensional
A.	Arteria
CT	Computertomographie
ELH	Endolymphhydrops
ELR	Endolymphatischer Raum
Gd	Gadolinium
HNO	Hals-Nasen-Ohren-Heilkunde
KM	Kontrastmittel
MM	Morbus Menière
MRT	Magnetresonanztomographie
PIVC	parieto-insulärer vestibulärer Cortex
PLR	Perilymphatischer Raum
RGB	Rot-Grün-Blau
ROI	region of interest
SI	Signalintensität
SNV	Signal-Rausch-Verhältnis
V.	Vena
VM	Vestibuläre Migräne
VOLT	volumetric local thresholding
VOR	Vestibulo-okulärer Reflex

Abbildungsverzeichnis

Publikationsliste

Die vorliegende kumulative Dissertation umfasst zwei bereits veröffentlichte Arbeiten:

Gerb J, Ahmadi SA, Kierig E, Ertl-Wagner B, Dieterich M, Kirsch V. VOLT: a novel open-source pipeline for automatic segmentation of endolymphatic space in inner ear MRI. J Neurol 2020; 267(Suppl 1):185–96.

Boegle R, Gerb J, Kierig E, Becker-Bense S, Ertl-Wagner B, Dieterich M, Kirsch V. Intravenous delayed Gadolinium-enhanced MR Imaging of the endolymphatic space: A methodological comparative study. Front Neurol 2021; 12:647296.

Andere bisherige Publikationen (chronologisch aufgeführt)

2015

Ertl M, Kirsch V, Gerb J, Boegle R, Krafczyk S, Dieterich M. Appraisal of the signal-to-noise-ratio of uni- and bipolar recordings of ocular vestibular evoked myogenic potentials. VES. 2015;25:9–14.

2018

Zwergal A, Kirsch V, Gerb J, Dlugaiczyk J, Becker-Bense S, Dieterich M. Neurootologie: Grenzfälle zwischen Ohr und Gehirn. Nervenarzt. 2018;89:1106–1114.

Kirsch V, Ertl-Wagner B, Berman A, Gerb J, Dieterich M, Becker-Bense S. High-resolution MRI of the inner ear enables syndrome differentiation and specific treatment of cerebellar downbeat nystagmus and secondary endolymphatic hydrops in a postoperative ELST patient. J Neurol. 2018;265:48–50.

2020

Boegle R, Kirsch V, Gerb J, Dieterich M. Modulatory effects of magnetic vestibular stimulation on resting-state networks can be explained by subject-specific orientation of inner-ear anatomy in the MR static magnetic field. J Neurol. 2020;267:91–103.

2021

Oh S-Y, Dieterich M, Lee BN, … Gerb J, …et al. Endolymphatic hydrops in patients with vestibular migraine and concurrent Meniere's disease. Front Neurol. 2021;12:594481.

2022

Gerb J, Brandt T, Dieterich M. Different strategies in pointing tasks and their impact on clinical bedside tests of spatial orientation. J Neurol. 2022;269:5738–5745.

Gerb J, Becker-Bense S, Zwergal A, Huppert D. Vestibular syndromes after COVID-19 vaccination: A prospective cohort study. Eur J Neurol. 2022;29:3693–3700.

2023

Kierig E, Gerb J, Boegle R, Ertl-Wagner B, Dieterich M, Kirsch V. Vestibular paroxysmia entails vestibular nerve function, microstructure and endolymphatic space changes linked to root-entry zone neurovascular compression. J Neurol. 2023;270:82–100.

Gerb J, Brandt T, Dieterich M. Different approaches to test orientation of self in space: comparison of a 2D pen-and-paper test and a 3D real-world pointing task. J Neurol. 2023;270: 642–650.

Dieterich M, Hergenroeder T, Boegle R, … Gerb J, … et al. Endolymphatic space is age-dependent. J Neurol. 2023;270:71–81.

Strupp M, Mandala M, Vinck AS, … Gerb J, …et al. The Semont-Plus maneuver or the Epley maneuver in posterior canal benign paroxysmal positional vertigo: A randomized clinical study. JAMA Neurol. 2023 Aug 1;80(8):798-804.

Gerb J, Brandt T, Huppert D. Historical descriptions of nystagmus and abnormal involuntary eye movements in various ancient cultures. Sci Prog. 2023 Jul-Sep; 106(3): 368504231191986.

Gerb J, Padovan L, Lehrer N, Brandt T, Dieterich M. Differential effects of gender and age on dynamic subjective visual vertical. Neurol Res Pract. 2023 Aug 24;5(1):37

Gerb J, Brandt T, Dieterich M. Shape configuration of mental targets representation as a holistic measure in a 3D real world pointing test for spatial orientation. Sci Rep. 2023 Nov 22;13(1):20449.

2024

Gerb J, Brandt T, Dieterich M. A clinical 3D pointing test differentiates spatial memory deficits in dementia and bilateral vestibular failure. BMC Neurol 24, 75 (2024).

Zusammenfassung

Bislang werden verschiedene neurootologische Diagnosen, wie z.B. der Morbus Menière oder die sog. Vestibuläre Migräne, allein auf der Basis einer Definition klinischer Symptome gestellt. Da sich diese bei beiden Krankheiten deutlich überlappen, ist eine eindeutige Zuordnung nicht immer möglich. Die Therapie beider Erkrankungen unterscheidet sich grundlegend, weshalb nach zusätzlichen Parametern gesucht wird, die eine genauere Diagnosestellung ermöglichen. So wird vermehrt z.B. die Bildgebung des Innenohrs mit der Magnetresonanztomographie (MRT) eingesetzt, um Pathologien im Innenohr aufzudecken wie u.a. eine Störung der Endolymph-Flüssigkeit. Ein Ungleichgewicht zwischen Endolymphbildung und Resorption kann zu einer Flüssigkeitsansammlung, dem sog. Endolymphhydrops (ELH), führen, welcher lange Zeit als pathognomonisch für den Morbus Menière gesehen wurde. Allerdings konnte inzwischen auch bei anderen neurootologischen Erkrankungen ein ELH nachgewiesen werden, weshalb exakte Auswertemethoden notwendig sind, um dessen pathologische Relevanz und krankheitstypische Muster besser zu verstehen.

Diese Dissertation befasst sich mit der Entwicklung, Testung und Anwendung einer quantifizierenden Methode der Innenohrbildgebung mit Hilfe kontrastmittelverstärkter, verzögerter MRT. Hiermit kann kontrastmittelangereicherte Perilymphflüssigkeit mit speziellen MRT-Sequenzen nachgewiesen werden. Basis der Quantifikation ist dabei ein dreidimensional und automatisch ablaufender Algorithmus, der die kontrastmittelverstärkte Perilymphe von der Endolymphe (welche kein KM aufnimmt) differenzieren kann. Ziel war es, in der Auswahl der verwendeten Software auf proprietäre, kommerziell vertriebene Software so weit wie möglich zu verzichten. Die entwickelten Lösungsansätze sollten für den klinischen Alltag praktikable Ansprüche bezüglich Rechenleistung und Bearbeitungszeit stellen.

Die Arbeit „VOLT: a novel open-source pipeline for automatic segmentation of endolymphatic space in inner ear MRI“ [1] befasst sich mit der semiautomatischen Auswertung von Innenohr-MRT-Aufnahmen. Auf Basis von *local-thresholding*-Algorithmen wurde eine valide Methode entwickelt, die bereits in Folgestudien [2] Anwendung fand. Zur Segmentation wurde eine Deep-Learning-Anwendung eingesetzt. Mit einem artifiziellen dreidimensionalen Testvolumen wurde die Leistung der Methode auf Rohdaten mit Bewegungs- oder Rauschartefakten geprüft. Es zeigte sich ein der manuellen Segmentation ebenbürtiges Ergebnis und eine Überlegenheit insbesondere bei artefaktreicheren Daten. Die berechneten Volumina korrelierten hochsignifikant mit den klinischen Graduierungen.

Ziel der Arbeit „Intravenous delayed gadolinium-enhanced MR imaging of the endolymphatic space: A methodological comparative study“ [3] war die klinische Anwendung der neuen semiquantitativen Methodik bei einem größeren Datensatz, um mögliche Fallstricke im alltäglichen Gebrauch zu testen und um die Leistungen im Vergleich zu etablierten schnittbasierten Quantifizierungs-methoden zu überprüfen. Dazu wurde VOLT bei insgesamt 216 Innenohren von 75 Menière-Patient:innen (55.2 ± 14.9 Jahre) sowie 33 gesunden Proband:innen (46.4 ± 15.6 Jahre) angewendet. Hier zeigte sich ein nur geringer Einfluss von Signal-Rausch-Verhältnis auf die Graduierungen und eine insgesamt gute Korrelation aus klinischer Graduierung und VOLT-Volumina. Für die klinische Einordnung der verschiedenen Krankheitsentitäten waren die ELH-Asymmetrie und die normalisierten ELH-Volumina am aussagekräftigsten.

Zusammengefasst behandelt diese Dissertation somit eine neuartige Quantifizierungsmethode zur Innenohrbildgebung, die schnell, einfach und günstig anwendbar ist und zur besseren Vergleichbarkeit von Innenohr-MRTs und damit zur besseren Abgrenzung verschiedener Erkrankungen beitragen kann.

Abstract

To date, various neuro-otological diagnoses, such as Meniere's disease or vestibular migraine, have been made solely on the basis of clinical symptoms. As these often overlap in both diseases, a clear classification is not always possible. The treatment of both diseases differs fundamentally, which is why additional parameters are being sought to enable a more precise diagnosis. For example, magnetic resonance imaging (MRI) is increasingly being used to detect pathologies in the inner ear, such as disorders of the endolymphatic fluid. An imbalance between endolymph formation and resorption can lead to an accumulation of fluid, the so-called endolymphatic hydrops (ELH), which for a long time was seen as pathognomonic for Meniere's disease. However, ELH has now also been demonstrated in other neuro-otologic diseases, which is why precise evaluation methods are necessary to better understand its pathological relevance and disease-typical patterns.

This dissertation deals with the development, testing and application of a quantifying method of inner ear imaging using contrast-enhanced delayed MRI. This allows contrast-enhanced perilymph fluid to be detected using special MRI sequences. The quantification is based on a three-dimensional and automatic algorithm that can differentiate the contrast-enhanced perilymph from the endolymph (which does not absorb contrast agent). The aim was to avoid proprietary, commercially marketed software as far as possible. The solutions developed were to meet practical requirements in terms of computing power and processing time for everyday clinical practice.

The study "VOLT: a novel open-source pipeline for automatic segmentation of endolymphatic space in inner ear MRI" [1] deals with the semi-automatic evaluation of inner ear MRI images. Based on local-thresholding algorithms, a valid method was developed, which has already been used in follow-up studies [2]. A deep learning application was used for segmentation. An artificial three-dimensional test volume was used to test the performance of the method on raw data with motion or noise artifacts. The results were on a par with manual segmentation and showed superior scores especially for data with more artifacts. The calculated volumes correlated highly significantly with the clinical graduations.

The aim of the study "Intravenous delayed gadolinium-enhanced MR imaging of the endolymphatic space: A methodological comparative study" [3] was the clinical application of the new semi-quantitative methodology on a larger data set to test potential pitfalls in everyday use and to verify the performance in comparison to established slice-based quantification methods. For this purpose, VOLT was applied to a total of 216 inner ears of 75 Meniere's patients (55.2 ± 14.9 years) and 33 healthy subjects (46.4 ± 15.6 years). Here, there was only a slight influence of signal-to-noise ratio on the graduations and an overall good correlation between clinical graduation and VOLT volumes. The ELH asymmetry and the normalized ELH volumes were the most meaningful for the clinical classification of the different disease entities.

In summary, this dissertation deals with a novel quantification method for inner ear imaging that is quick, easy and inexpensive to use and can contribute to better comparability of inner ear MRIs and thus to better differentiation of different diseases.

Einleitung

Das Symptom Schwindel ist in der (Akut-) Medizin oftmals schwer diagnostisch einzugrenzen, da Schwindel sowohl durch harmlose als auch lebensbedrohliche Ursachen ausgelöst werden kann, die aus Fachbereichen wie der Neurologie, der Hals-Nasen-Ohren-Heilkunde (HNO), der Inneren Medizin und der Psychiatrie stammen können [5]. Nach Kopfschmerz ist Schwindel das zweithäufigste Leitsymptom in der Neurologie; die Lebenszeitprävalenz beträgt 17-30% [6].

Schwindel als Leitsymptom im engeren Sinn (wie bei Drehschwindel) entsteht durch ein Ungleichgewicht im vestibulären System, welches periphere vestibuläre und zentrale vestibuläre Anteile besitzt. Entwicklungsgeschichtlich handelt es sich hier um ein altes System, welches teils seit frühen evolutionären Stufen konserviert und bei allen Säugetieren bezüglich der peripheren Sensororgane grundsätzlich ähnlich aufgebaut ist [7].

Es gibt verschiedene Ursachen für akute Schwindelepisoden peripherer und zentraler Natur. Eine mögliche Ursache für eine akute Drehschwindelattacke ist der „Morbus Menière“ (MM) mit der typischen Trias aus einseitiger Hörminderung, Tinnitus und Drehschwindel über einige Stunden. Pathophysiologisch wurde ein Endolymphhydrops (ELH) angenommen, d.h. eine übermäßige Ansammlung der Innenohrflüssigkeit Endolymphe. Die Diagnosestellung ist oft schwierig und es können Mischsyndrome mit einer weiteren Erkrankung mit Drehschwindelepisoden, der Vestibulären Migräne (VM), vorliegen. Ein unbehandelter MM führt zur Taubheit und einem Schaden des Vestibularorgans. Medikamentöse Therapien sowie invasive Therapien nach Eskalationsstufen können dies häufig verhindern, wenn die Erkrankung frühzeitig diagnostiziert und behandelt wird. Deshalb wird nach zusätzlichen Untersuchungsverfahren gesucht, die eine frühe Diagnose erlauben, möglichst so früh, dass noch keine bleibenden, neurophysiologisch messbaren Defizite bei den Höhr- und Gleichgewichtstests vorliegen.

Die erstmalige in-vivo-Darstellung der Innenohrflüssigkeitskompartimente per Magnetresonanz-tomographie (MRT) beim Menschen erfolgte in 2007 [8]. Durch die zunehmende Verfügbarkeit dieser Bildgebungsmethode zeigte sich, dass ein ELH auch bei anderen Schwindelerkrankungen vorliegen sowie auch ohne Krankheitswert oder jegliche Symptome bei gesunden Personen auftreten kann [9]. Um die pathophysiologische Relevanz eines ELH realistisch einschätzen und verlässlich vergleichen zu können, sind also Quantifizierungen der MRT-Befunde nötig. Ziel dieser Arbeit war daher die Entwicklung und Demonstration einer möglichen Quantifizierung per „volumetrischem local thresholding“, welche über die bisher bekannten, 2D-schnittbasierten Graduierungen hinausgeht und im Wesentlichen automatisch ohne subjektive Einschätzung funktioniert.

1.1 Hintergrund

1.1.1 Das zentral- und peripher-vestibuläre System

Das vestibuläre System dient der Haltungsregulation, der Blickstabilisation und der Bewegungswahrnehmung und besitzt periphere (Gleichgewichtsorgan, N. vestibulocochlearis) und zentrale (Ncl. vestibulares, Hirnstammbahnen, verschiedene Kortexregionen) Anteile. Die Signale des Gleichgewichtsorgans werden über den Nervus vestibulocochlearis, welcher gemeinsam mit dem N. facialis sowie der A. / V. labyrinthi durch den Meatus acusticus internus verläuft, in den Hirnstamm geleitet und dort in den Vestibulariskernen verschaltet. Innerhalb des Hirnstamms kommt es zu mehreren Kreuzungen, supratentoriell gibt es wohl sowohl intra- als auch extrathalamische Bahnen zu verschiedenen kortikalen Arealen. Der vestibuläre Kortex ist in der Inselregion lokalisiert mit einer Zentrale im parieto-insulären vestibulären Cortex (PIVC)[10]. Es bestehen Interaktionen mit modulierenden und einer reziproken Inhibition unterliegenden Einflüssen aus dem visuellen System sowie somatosensorischen und propriozeptiven Signalen aus der Haltungsmuskulatur und den Extremitäten.

1.1.2 Anatomie und Physiologie des vestibulären Endorgans

Das Gleichgewichtsorgan (Abbildung 1, [11]) ist im Felsenbein des Menschen lokalisiert und besteht aus dem knöchernen sowie dem membranösen Labyrinth, der Cochlea und dem Nervus vestibulocochlearis. Innerhalb des mit Perilymphe gefüllten knöchernen Labyrinths befindet sich das membranöse, mit Endolymphe gefüllte Labyrinth, ein schlauchartiges System, das in die drei c-förmig vom Vestibulum ausgehenden Bogengänge hineinreicht, die Makulaorgane Utriculus und Sacculus über den Ductus reuniens miteinander verbindet und mit der Scala media in der Cochlea in Verbindung steht. In den hier lokalisierten Zellen der Stria vascularis wird die Endolymphe produziert, füllt das membranöse Labyrinth und fließt über den Ductus endolymphaticus in den blind endenden endolymphatischen Sack (ES), von wo sie sowohl resorbiert wird als auch in die äußeren Liquorräume des Gehirns diffundiert [12]. Der ES kann offenbar die Endolymphmenge regulieren [13,14]. Chemisch ähnelt die Perilymphe der Extrazellulärflüssigkeit und ist natriumreich, während die Endolymphe Intrazellulärflüssigkeit ähnelt und kaliumreich ist. Diese unterschiedliche Ionenkonzentration führt zu einem positiven elektrischen Potential der Endolymphe gegenüber der Perilymphe. Die Perilymphe ist ein Ultrafiltrat des Liquors und steht über den Aquaeductus cochleae mit dem Liquorraum in Verbindung. Die drei mit Endolymphe gefüllten Bogengangsanteile des membranösen Labyrinths enden in Aufweitungen, an denen jeweils ein Sinnesorgan liegt. Bei Drehbewegungen kommt es aufgrund der Trägheit der Flüssigkeiten sowie der gallertigen Masse zu Auslenkungen der Sinneszellen und einer Zunahme der Basisaktivität der Haarzellen. Nach einem ähnlichen Prinzip funktionieren die Makulaorgane, die beiden Otolithen Sacculus und Utriculus, in denen auf einer Epithelschicht mit Kino- u. Stereozilien die sog. Otokonien aus Calcium-Carbonat ($CaCO3$) heften [15]. Die Makulaorgane detektieren mittels in der jeweiligen Raumachse angeordneten Kino- u. Stereozilien vertikale (Sacculus) und horizontale (Utriculus) Bewegungen. Über den Nervus vestibulocochlearis (bestehend aus N. vestibularis superior für den Utriculus, Teile des Sacculus sowie die Signale des anterioren und des lateralen Bogengangs, und dem N.

vestibularis inferior für den Sacculus sowie dem posterioren Bogengang), werden die Signale des vestibulären Endorgans in den Hirnstamm geleitet.

Die Innenohranatomie als biologisches System ist variabel mit teils signifikanten inter- und intraindividuellen Unterschieden in Bogengangsradius, -planarität und -winkel [16]. Ein Zusammenhang zwischen dem bereits pränatal ausgebildeten knöchernen Labyrinth und der Gleichgewichtsfunktion wurde i.R. dieser Variabilität nicht festgestellt. Es bestehen jedoch auch Anlageeinschränkungen, die mit einer vestibulären (oder cochleären) Unterfunktion einhergehen, beispielsweise beim CHARGE-Syndrom [17], bei dem es aufgrund einer CHD7-Genmutation oftmals zu Bogengangsdefekten kommt [18].

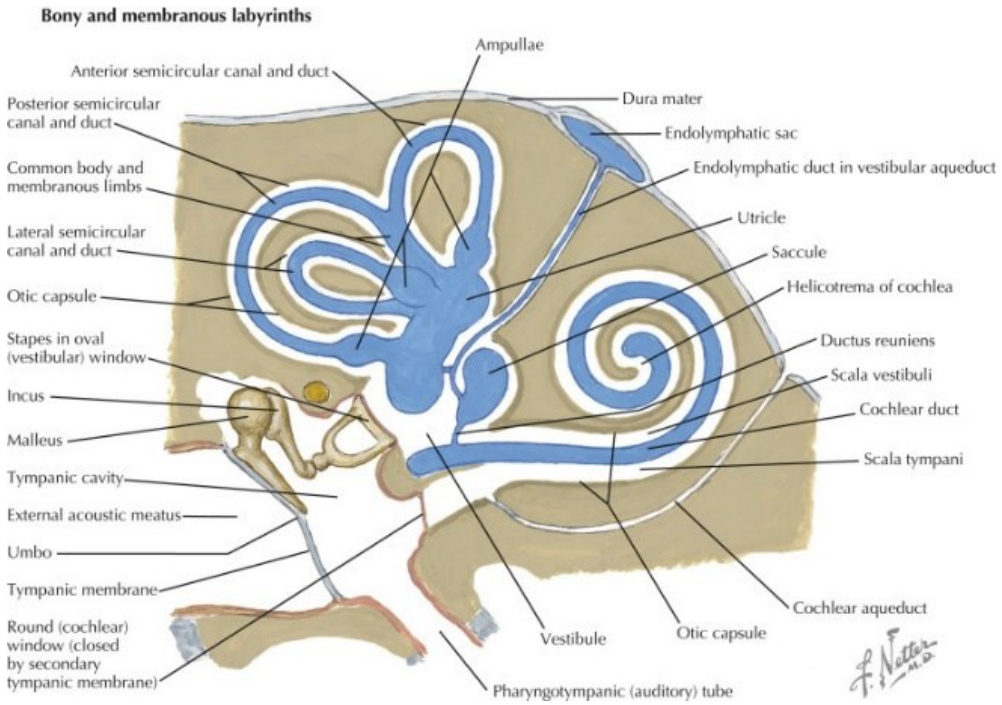

Abbildung 1: Überblick Innenohranatomie (aus ‚Netter's atlas of neuroscience', Felten et al., 2016)

1.1.3 Vestibuläre Funktionsdiagnostik

Verschiedene Tests existieren, um das vestibuläre System zu untersuchen. Bereits im frühen 20. Jahrhundert wurde der kalorische Nystagmus (durch Irrigation des horizontalen Bogengangs per warmem und kaltem Wasser) von Robert Bárány (dem späteren Nobelpreisträger für Medizin und Physiologie 1914) beschrieben[19]. Mit diesem, auch heute noch standardmäßig durchgeführtem Test lässt sich der Niederfrequenzbereich des Vestibulo-Okulären-Reflexes testen, während schnelle Kopfdrehungen zur Seite bei simultaner visueller Fixation eines Punktes den Hochfrequenzbereich überprüfen (Kopfimpulstest, auch Halmagyi-Curthoys-Test [20]). Eine weitere, heute nur noch seltener durchgeführte Untersuchungsmethode ist die Drehstuhluntersuchung, bei der Dauer und Intensität eines postrotatorischen Nystagmus beurteilt werden können [21]. Durch zervikal und okulär abgeleitete vestibulär evozierte Potentiale lassen sich die Otolithenorgane testen [22] und beispielsweise Störungen der knöchernen Bedeckung einzelner Bogengänge diagnostizieren [23]. Zentral-vestibuläre Störungen führen oftmals zu Auffälligkeiten in der

Neuroorthoptik und können durch Augenfehlstellungen diagnostiziert werden[24]. Als Akutzeichen einer vestibulären Tonusimbalance ist eine *ocular tilt reaction* möglich, eine Auge-Kopf-Neigung um die Sehlinie als Achse, wodurch eine topodiagnostische Einordnung erfolgen kann [25]. Während durch eine ausführliche klinische Untersuchung sowie eine strukturierte Anamnese viele Schwindelerkrankungen bereits diagnostiziert werden können (und die Kombination klinischer Zeichen einem frühen cMRT bei akuten zentralen vestibulären Syndromen gar überlegen ist, [26]), braucht es dennoch oftmals Bildgebung, um andere Pathologien auszuschließen oder die Lokalisation genauer einzugrenzen.

1.1.4 Endolymphhydrops und episodische Schwindelerkrankungen

Differentialdiagnostisch zu bedenkende Krankheiten, die mit Drehschwindel von bis zu mehreren Stunden Dauer einhergehen können, sind - wie oben erwähnt - der Morbus Menière (MM, [27]) sowie die Vestibuläre Migräne (VM, [28]). Während bei beiden Erkrankungen oftmals wegweisende Begleitsymptome vorhanden sind, die eine Unterscheidung ermöglichen (bspw. Phono-/Photophobie, Kopfschmerz, Aurasymptomatik bei VM [29], cochleäre Symptomatik und Hörminderung bei MM [27], siehe Abbildung 2), kann sich das klinische Bild auch stark ähneln, insbesondere wenn Begleitsymptome weniger stark wahrgenommen oder erinnert werden. Zudem kommen cochleäre Begleitsymptome auch bei ca. 38% der Attacken einer VM vor [30] und können in etwa 30% der Attacken über Stunden anhalten [31].

Pathophysiologisch wurde beim MM das rezidivierende Einreißen der Reißnerschen Membran aufgrund einer übermäßigen Endolymphansammlung, die damit einhergehende Vermischung von kaliumarmer Perilymphe und kaliumreicher Endolymphe sowie die daraus folgende Depolarisation von vestibulären und cochleären Haarzellen [32] angenommen. Ob das Flüssigkeitsungleichgewicht aufgrund einer Überproduktion, einer Abflussstörung oder einer anderen Pathogenese entsteht, ist weiterhin nicht eindeutig geklärt [33]. Der Vestibulären Migräne liegt hingegen, vergleichbar zur Kopfschmerzmigräne, eine sowohl konstitutionelle als auch trigemino-vaskulär-modulierte vestibuläre Hyperexzitabilität zugrunde [34–36].

Die Therapie der beiden Krankheiten unterscheidet sich erheblich: während bei der VM Migräneprophylaktika eingesetzt werden (bspw. Betablocker, Antikonvulsiva, Antidepressiva oder Calciumkanalblocker [37]) und auch durch Lebensstilanpassungen [38] oder Nahrungs-ergänzungsmittel [39] eine Reduktion der Attackenfrequenz herbeigeführt werden kann, werden beim MM überwiegend der inverse H3-Rezeptor-Agonist (Betahistin [40]) sowie im Falle eines Nichtansprechens lokal invasive Maßnahmen (intratympanale Gentamicin-, Kortikosteroidinstillation [41]) verwendet. Operative Möglichkeiten sind die erstmals 1927 beschriebene Sakkotomie [42] oder als ultima ratio die Durchführung einer Labyrinthektomie oder einer Neurektomie. Andere operative Ansätze wie die Tenotomie der M. stapedius-/M. tensor tympani-Sehnen [43] oder die Anlage eines Endolymph-Perilymph-Shunts werden heute kaum mehr verwendet [44].

Betahistin greift agonistisch an Histamin-H1-Rezeptoren und antagonistisch an Histamin-H3-Rezeptoren an, welche bspw. im endolymphatischen Sack exprimiert werden [45]. Eine Fehldiagnose und eine daraus folgende inadäquate Behandlung eines MM kann zu dauerhaften Innenohrschäden (bis hin zur völligen Ertaubung und dem Ausfall der Gleichgewichtsfunktion auf der betroffenen Seite) führen. Da ein MM auch beidseitig auftreten kann, ist dies eine häufige Ursache einer beidseitigen Vestibularisschädigung, der bilateralen Vestibulopathie (BVP) [46].

Da sich beide Erkrankungen – besonders in frühen Krankheitsstadien, in denen wir sie erkennen wollen - nicht immer gut anhand der Symptome und der neurootologischen Befunde differenzieren lassen, wird nach weiteren und verlässlicheren Biomarkern gesucht. Hier könnte das Innenohr MRT mit Quantifizierung der Innenohrstrukturen zur Frage des ELH hilfreich sein.

	Definitive VM	Definitiver MM
Attackendauer	5 Minuten – 72 Stunden	20 Minuten – 12 Stunden
Attackenanzahl	>5	>2
Cochleäre Beteiligung	-	Tieftonsenke >30dB
Ohrsymptome	-	Tinnitus o. Völlegefühl, fluktuierend
Migränesymptome	>50% der Attacken	-
Migräneanamnese	Ja (aktuell o. in Vorgeschichte)	-

Abbildung 2: Diagnosekriterien der Bárány-Society für VM, MM nach Lempert et al., 2012 u. Lopez-Escamez et al., 2015

1.2 Zeitverzögerte, kontrastmittel-verstärkte MRT Bildgebung des Innenohrs

1.2.1 Grundlagen der Magnetresonanztomographie

Die Bildgebung per Magnetresonanz wurde erstmals in 1973 vorgestellt [47] , die erste Darstellung des menschlichen Gehirns in vivo per MRT erfolgte 1982 [48]. Seit Mitte der 1980er Jahre werden auch paramagnetische Gadolinium-Verbindungen als intravenös verabreichte Kontrastmittel eingesetzt [49,50].

Die Kernspintomographie funktioniert, indem die Rotationsachse des Spins von Atomkernen mit einer ungeraden Neutronen- o. Protonenanzahl durch ein starkes Magnetfeld ausgerichtet wird und die um diese Achse präzessierenden Kerne mittels eines elektromagnetischen Hochfrequenz-impulses einer entsprechenden Frequenz (Lamor-Frequenz) auf ein höheres Energieniveau ausgelenkt werden, weiterhin werden die Präzessionsbewegungen phasensynchronisiert. Die hierbei aufgenommene Energie wird je nach Protonendichte des untersuchten Materials unterschiedlich schnell wieder abgegeben, während sich die Kerne wieder im statischen Magnetfeld ausrichten (Längsmagnetisierung, T1-Relaxation) bzw. die Synchronisation der Präzessionsbewegung abnimmt (T2-Relaxation, Transversalmagnetisierung). Dies kann mittels Spulen detektiert werden. Durch Verwendung eines Magnetengradienten kann eine genaue räumliche Lokalisation des Signals und aufbauend hierauf die Bildgebung erfolgen [51]. Dies kann sowohl zur Materialanalyse von bspw. Festkörpern eingesetzt werden, ist jedoch auch zur Unterscheidung verschiedener biologischer Gewebe verwendbar. Gegenüber CT-Untersuchungen sind vor allem die fehlende Strahlenbelastung und eine bessere Weichteilauflösung als Vorteile zu nennen, wohingegen knöcherne Strukturen per CT genauer darzustellen sind.

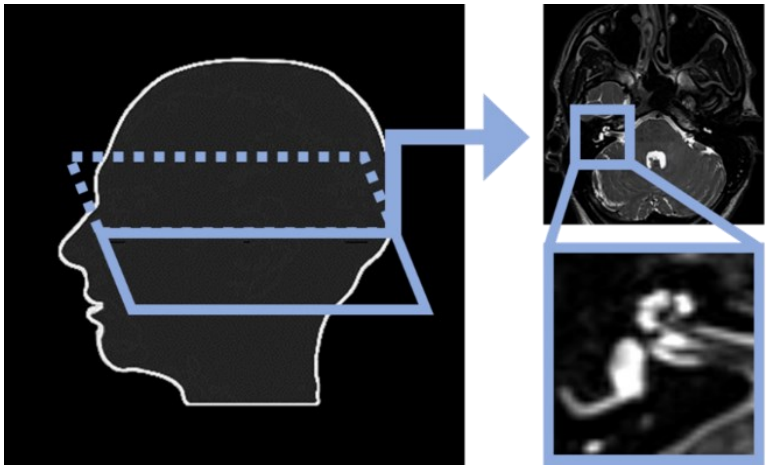

Abbildung 3: T2-Aufnahme eines rechten Innenohrs. Gemäß radiologischer Konvention beschreibt die linke Bildseite die rechte Patientenseite.

1.2.2 Vorteile multisequentieller MRT des Innenohrs

Erkrankungen, die durch strukturelle Veränderungen (bspw. lokal raumfordernde Effekte wie beim Vestibularisschwannom) zu Schwindel führen, können durch Schnittbildgebung sicher erkannt und therapiert werden; kontrastmittelverstärkte Sequenzen erreichen eine Sensitivität und Spezifität von annähernd 100% [52]. Fälle von bereits ausgedehnter lokaler Raumforderung mit Hirnstamm-kompression und Inoperabilität [53] sind heute eine Ausnahme [54]. Viele Schwindelerkrankungen gehen jedoch nicht mit einer rein strukturellen Schädigung einher und erfordern daher multisequentielle Bildgebung. Während eine kontrastmittelverstärkte T1-Sequenz Entzündungen, Tumoren und Blutgefäße deutlich darstellt, können bspw. Gefäß-Nerven-Kontakte durch den Kontrast zum (hyperintensen) Liquor besser in hochaufgelösten T2-Sequenzen visualisiert werden [55], insbesondere in Kombination mit Gefäßdarstellungen (bspw. mittels time-of-flight-Angiographie). Für die Diagnostik verschiedener zentraler Schwindelerkrankungen können weiterhin Protonenwichtung[56] oder Diffusionssequenzen[57] hilfreich sein.

1.2.3 Arten verzögert kontrastverstärkter MRT des Innenohrs

Die verschiedenen Innenohrkompartimente sind einerseits biophysikalisch zu ähnlich, um in einer nativen MRT-Untersuchung grundsätzlich verschiedene Signalintensitäten zu erzeugen und andererseits in ihrer Ausdehnung so gering, dass eine direkte Darstellung der begrenzenden Strukturen derzeit unterhalb der MRT-Nachweisgrenze, d.h. der kleinsten, MR-tomographisch erreichbaren Auflösung liegt. Trotz vieler Fortschritte bezüglich MR-Sequenzen, Feldstärken etc. ist die räumliche Auflösungsgrenze im Submillimeterraum [58]. Daher konnte ein MM bislang nicht in der strukturellen MRT dargestellt werden. Andere diffusionsbasierte Ansätze zur indirekten Darstellung biologischer Mikrostrukturen werden bislang noch nicht klinisch angewendet [59]. Zur Beurteilung des Endolymphraums ist aktuell daher eine indirekte, kontrastmittelverstärkte, strukturelle Methodik notwendig. In den Erstbeschreibungen [8] wurde eine lokale Kontrastmittel-applikation gewählt (Instillation durch das Trommelfell, Seitlagerung des Patienten und dadurch

ermöglichte Diffusion des Kontrastmittels durch das runde Fenster in die Perilymphe), die MRT-Bildgebung erfolgte dann 24h später. Eine lokal-toxische Wirkung der verwendeten Gadolinium-Lösungen konnte bislang weder bestätigt noch sicher widerlegt werden, elektrophysiologische Veränderungen waren jedoch zumindest im Tierversuch nachweisbar [60].

Grundlegend limitierend kann auf diese Weise jedoch stets nur ein Innenohr untersucht werden. Weiterhin ist die lokale Verteilung des Kontrastmittels oftmals inhomogen. Aus diesen Gründen wurde die intratympanale Kontrastmittelgabe inzwischen überwiegend zugunsten der intravenösen Applikation verlassen, welche 2010 erstmals beschrieben wurde [61]. Hier besteht typischerweise eine Zeitspanne von 4-5 Stunden zwischen KM-Gabe und Bildakquise, in der eine Kontrastmittelanreicherung in der Perilymphe erfolgt, während die Endolymphe als eigens in der Stria vascularis produzierte Flüssigkeit kein KM anreichert.

Ein weiteres grundsätzliches Problem der indirekten Endolymphdarstellung im MRT ist die Abhängigkeit von einer gleichbleibenden und vergleichbaren KM-Aufnahme in der Perilymphe. Da die untersuchte Struktur nur über die Kontrastmittelaufnahme der Umgebungsflüssigkeit dargestellt wird, beeinflussen Faktoren, die die dortige KM-Aufnahme beeinträchtigen, auch das Abbildungsergebnis. Durch die systemische i.v.-Applikation sind methodenbedingt lokale Inhomogenitäten zwar theoretisch ausgeschlossen, im Falle lokalisierter bzw. entzündlicher Prozesse aber dennoch möglich. Mögliche Faktoren, die die Innenohrhomöostase (und damit KM-Anreicherung in der Perilymphe) beeinflussen können, sind vielfältig [62–64] und noch nicht abschließend erforscht. Eine endgültig verallgemeinerbare Pharmakokinetik der Innenohrkontrastierung kann derzeit noch nicht angenommen werden. Über den Zeitraum von 4-5 Stunden zwischen KM-Applikation und Bildakquise sind viele individuelle Einflussfaktoren anzunehmen.

Durch die zunehmende Verfügbarkeit der MRT zeigte sich, dass ein ELH jedoch auch bei anderen Schwindelerkrankungen vorliegen sowie auch ohne Krankheitswert oder jeglicher Symptome bei gesunden Personen auftreten kann [9]. Weiterhin fand sich eine zeitliche Dynamik mit schwankender Ausdehnung des ELH [65]. Um die pathophysiologische Relevanz eines ELH realistisch einschätzen und verlässlich vergleichen zu können, sind also Quantifizierungen der MRT-Befunde nötig. Ziel dieser Arbeit war daher die Entwicklung und Demonstration einer möglichen Quantifizierung per volumetrischem *local thresholding*, welche über die bisher bekannten, 2D-schnittbasierten Graduierungen hinausausgeht und im Wesentlichen ohne menschlichen Input und damit ohne subjektiv variable Auswerteparameter funktioniert.

1.3 Quantifizierung des endolymphatischen Raums

1.3.1 Bestehende Ansätze (semi-quantitativ, atlas-basiert, semi-automatisiert)

Die radiologisch erhobenen Daten des Innenohr-MRTs können nach verschiedenen Gesichtspunkten ausgewertet werden. Zur exakten Ausmessung des ELR ist eine manuelle Segmentation notwendig, welche zeitaufwendig und subjektiv ist. Aus diesem Grund wurden verschiedene Systeme zur Graduierung eines ELH etabliert, wobei die verbreitetsten in [66] beschrieben sind. Allen Systemen gemeinsam ist die 2D-schnittbasierte Auswertung sowie ihre Komplexität, welche einerseits eine große Erfahrung der Untersucher:innen erfordert und andererseits die Vergleichbarkeit der Ergebnisse reduziert. Eine verbreitete Quantifizierung [67] verwendet einen midmodiolaren Schnitt (d.h., auf Höhe des modiolus cochleae, also der knöchernen Achse, um welche sich die Cochlea windet) und teilt sowohl Cochlea als auch Vestibulum nach festgelegten Kriterien in ELH dreier Schweregrade (Abbildung 4).

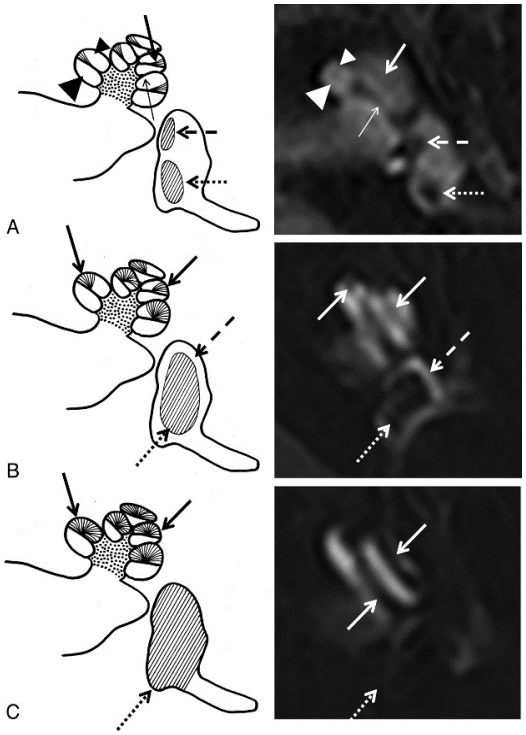

Abbildung 4: 2D-basierte Graduierung (Abbildung aus [Baráth et al., 2014]). A: Normalbefund mit interscalar septum (dünner Pfeil), scala tympani (große Pfeilspitze), osseous spiral lamina/cochlear duct (dicker Pfeil), scala vestibuli (kleine Pfeilspitze), Sakkulus (gestrichelter Pfeil), Utrikulus (gepunkteter Pfeil). B. cochleärer Hydrops Grad 1 mit Erweiterung und teilweiser Verlegung der scala vestibuli (dicke, durchgezogene Pfeile). Bei einem vestibulären Hydrops Grad 1 füllt der erweiterte Endolymphraum (gepunkteter Pfeil) über 50% des Vestibulums aus, ein Perilymphsaum (gestrichelter Pfeil) bleibt sichtbar. C. cochleärer Hydrops Grad 2 mit vollständiger Verlegung der scala vestibuli (dicke, durchgezogene Pfeile). Bei einem vestibulären Hydrops Grad 2 ist aufgrund der Erweiterung des Endolymphraums kein Perilymphraum mehr sichtbar (gepunkteter Pfeil).

Ein erster Ansatz zur computergestützten Analyse wurde 2015 von Gürkov et al. [68] beschrieben. Andere Ansätze zur quantitativen Auswertung wie *Radiomics* wurden ebenfalls erprobt [69].

1.3.2 Herausforderungen einer automatisierten Auswertung des Innenohrs

Die indirekte Endolymphdarstellung im MRT hängt von der KM-Aufnahme der Perilymphe ab. Im Falle einer insgesamt schwachen Kontrastierung kann insbesondere ein vollautomatisches System nicht sicher den Unterschied zwischen einer Signalauslöschung durch einen ELH oder aber einer messtechnisch bedingten Minderkontrastierung beurteilen, auch die radiologische Beurteilung kann sich hier oftmals nur schwerlich festlegen.

Die individuell variable Innenohranatomie darf ebenfalls nicht unterschätzt werden. Jegliche Ansätze zur Automatisierung müssen diese Variabilität sowohl in der Verarbeitung als auch in der Auswertung integrieren, um individuelle Abweichungen von der Durchschnittsanatomie nicht zu pathologisieren, relevante Befunde jedoch auch nicht zu übersehen.

Ein weiteres Problem der in-vivo-MRT-Visualisierung der Innenohrflüssigkeiten stellt der fehlende Goldstandard dar. In post-mortem Präparaten ist eine Beeinflussung des Endolymphraum bzw. der begrenzenden Strukturen durch unvermeidbare bspw. Gefrierartefakte der standardmäßigen histologischen Aufarbeitung [70] zu erwarten. Auch ist aufgrund der Dynamik des ELH mit noch überwiegend unerforschtem zeitlichem Verlauf [71,72] selbst bei Vorliegen von post-mortem Präparaten kein direkter Vergleich der in-vivo und ex-vivo Methoden möglich. Tierversuche mit experimentell herbeigeführtem ELH [73] können zwar Bildgebung und Euthanasie u. post-mortem-Beurteilung zeitlich abstimmen [74], stellen jedoch eine artifizielle Situation dar und sind nur begrenzt auf den Menschen übertragbar.

1.3.3 Grundlagen Bildverarbeitung: globale und lokale Binarisierung

Thresholding beschreibt in der digitalen Bildverarbeitung eine Methode zur Binarisierung von Daten [75] anhand eines Schwellwerts. Ein Bild in Graustufen (bzw. ein in die einzelnen Farbkanäle gesplittetes buntes RGB-Bild) lässt sich auf diese Weise in Vordergrund (weiß, 1) und Hintergrund (schwarz, 0) aufteilen. Der einfachste denkbare Algorithmus würde etwa alle Bildintensitäten oberhalb eines globalen Mittelwerts t (± einer optionalen Konstante *c*) als Vordergrund sowie alle Intensitäten unterhalb dieses Wertes als Hintergrund einteilen (Abbildung 5).

```
pixel = ( pixel > mean - c ) ? object : background
```

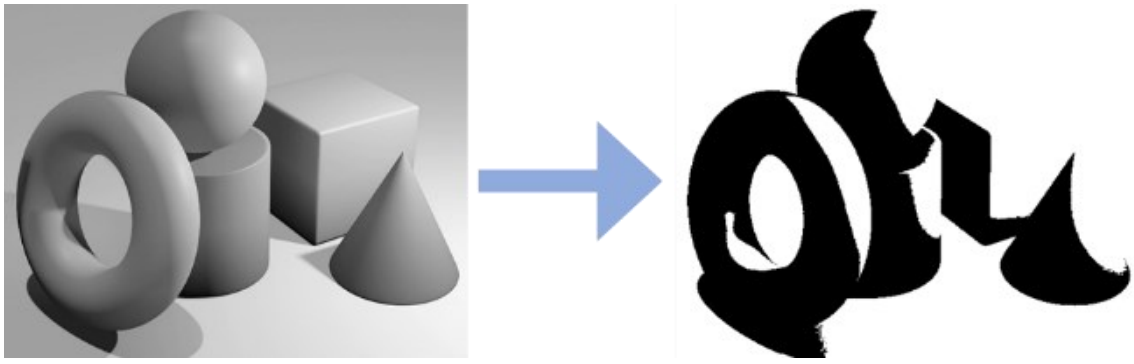

Abbildung 5: Anwendungsbeispiel eines globalen thresholds (mean)

Elaboriertere Algorithmen arbeiten beispielsweise histogrammbasiert oder verwenden komplexere Formeln zur Berechnung eines globalen *threshold*-Wertes t als Cutoff [76]. Bei Rohdaten, deren Intensität je nach Bildbereich heterogen ist, können lokale Algorithmen angewendet werden, die jeweils nur einen frei definierbaren Bildausschnitt für einen lokalen Grenzwert verwenden [77]. Der *local-thresholding* Algorithmus nach Bernsen [78] arbeitet bspw. mit einem frei definierbaren *local contrast threshold*. Wenn der *local contrast* (lokales Maximum – lokales Minimum) in einer bestimmten Bildregion größer oder gleich diesem Wert ist, wird der lokale t-Wert dem *local midgray value* gleichgesetzt, also dem Mittel aus lokalem Minimum und lokalem Maximum. Ist der *local contrast* unterhalb des *contrast thresholds*, wird die gesamte Region je nach Mittelwert aus lokalem Minimum und lokalem Maximum entweder in Vordergrund oder in Hintergrund eingeteilt (Abbildung 6).

```
if ( local_contrast < contrast_threshold )
 pixel = ( mid_gray >= 128 ) ? object :  background
else
 pixel = ( pixel >= mid_gray ) ? object : background
```

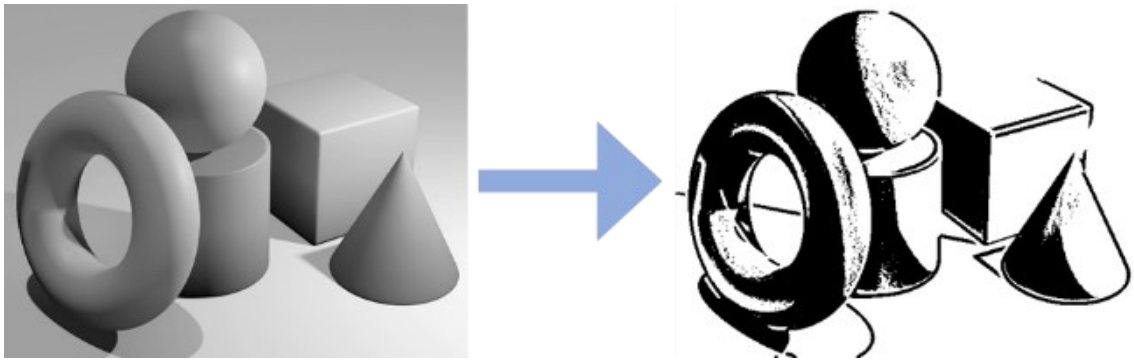

Abbildung 6: Anwendungsbeispiel eines lokalen thresholds (Bernsen)

Wichtig ist die Anpassung der verwendeten Bildausschnitte je nach räumlicher Ausdehnung der Zielstruktur, um Klassifizierungsfehler zu vermeiden. Ein zu kleiner Radius führt insbesondere bei höherem Bildrauschen zu einer fehlerhaften Unterteilung und Pseudokontrastierung eigentlich homogener Bildareale, ein zu großer Radius kann kleinere Strukturen hingegen nicht mehr auflösen und liefert dann nur noch einem globalen threshold vergleichbare Ergebnisse. Unabhängig vom verwendeten Radius kommt es zur Ausbildung eines Halos um klare Kanten zwischen homogenen

Flächen verschiedener Intensitäten mit der Ausdehnung des verwendeten Radius r (siehe Abbildung 7).

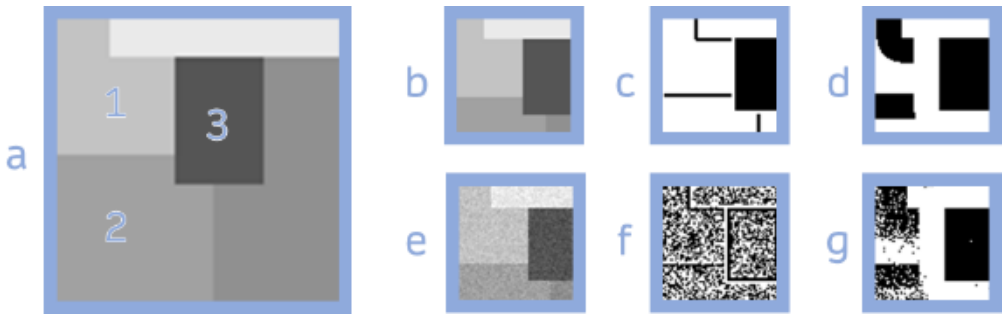

Abbildung 7: Beispiele fehlerhafter Klassifikationen, gezeigt anhand des Bildausschnitts (b) eines Testquadrats (a). Da Fläche 2 dunkler als Fläche 1, jedoch heller als Fläche 3 ist, entsteht bei Verwendung eines großen Radius ein deutlicher Halo (siehe d) mit der Ausdehnung r, welcher bei Verwendung eines kleinen Radius (siehe c) weniger stört. Bei verrauschten Bildern (e) kann ein kleiner Radius jedoch keine Flächen mehr darstellen (f); der größere Radius ist hier zuverlässiger (g).

2. Paper I: VOLT: a novel open-source pipeline

Der Inhalt dieses Kapitels wurde als „VOLT: a novel open-source pipeline for automatic segmentation of endolymphatic space in inner ear MRI" veröffentlicht in:

Gerb J, Ahmadi SA, Kierig E, Ertl-Wagner B, Dieterich M, Kirsch V. VOLT: a novel open-source pipeline for automatic segmentation of endolymphatic space in inner ear MRI. J Neurol 2020; 267(Suppl 1):185–96.

2.1 Kurzzusammenfassung

Um einen ELH im Innenohr-MRT vergleichen zu können, müssen die Ergebnisse quantifiziert und objektiviert werden. In dieser Arbeit wird eine neuartige Methode zur automatischen volumetrischen Auswertung von kontrastmittelverstärkter zeitverzögerter Innenohrbildgebung (iMRI) namens VOLT demonstriert.

VOLT (aus „Volumetric Local Thresholding") wurde auf einem Datensatz von Patient:innendaten D1 (bestehend aus 210 Innenohren von 105 Patient:innen, mittleres Alter 50.4 ± 17.1 Jahre) entwickelt und im Anschluss an einem künstlichen Testdatensatz D2 (bestehend aus einem Dummyvolumen (bestehend aus einem 8Bit-Körper mit definierter geometrischer Binnenstruktur) mit artifiziellen Bildartefakten verschiedener Ausprägung und einem zur Entwicklung ungenutzen Patient:innen-datensatz D3 (aus 20 händisch segmentierten Innenohren von 10 Patient:innen, mittleres Alter 46.8 ± 14.4 Jahre) validiert. Zur Beurteilung wurde einerseits der Sørensen-Dice-Koeffezient [79] errechnet, weiterhin wurde die Segmentationsgenauigkeit durch den Vergleich der jeweiligen Volumina von Endolymphraum (ELR) und Perilymphraum (PLR) in manueller und VOLT-Segmentation untersucht.

VOLT konnte insbesondere bei verrauschten Bildern eine bessere Segmentationsrate als ein validierter Goldstandard liefern. Die errechneten Volumina korrelierten signifikant mit der klinischen semiquantitaven Graduierung. Die Rechenzeit lag durchschnittlich unter 60 Sekunden.

VOLT ist somit ein zuverlässiges Werkzeug zur Objektivierung von iMRI und kann einen wichtigen Beitrag in Big-Data-Analysen von Innenohr-MRT bei Patient:innen mit episodischen Schwindel-erkrankungen liefern.

2.2 Beitrag zu Paper I

JG: Studiendesign, Datenakquise, Programmierung, Algorithmuserstellung, statistische Auswertung, Abbildungserstellung, Manuskriptentwurf und -korrektur. AA: Mitarbeit Algorithmus-erstellung, Manuskriptentwurf und -korrektur, EK: Datenakquise, BEW: Datenakquise, radiologische Beurteilung, MD: Studiendesign, Finanzierung, Manuskriptentwurf und -korrektur, VK: Studiendesign, Abbildungserstellung, Manuskriptentwurf und -korrektur.

2.3 Paper I (Volltext)

Journal of Neurology (2020) 267 (Suppl 1):S185–S196
https://doi.org/10.1007/s00415-020-10062-8

ORIGINAL COMMUNICATION

VOLT: a novel open-source pipeline for automatic segmentation of endolymphatic space in inner ear MRI

J. Gerb[1,2] · S. A. Ahmadi[1,3] · E. Kierig[1,2] · B. Ertl-Wagner[4,5] · M. Dieterich[1,2,3,6] · V. Kirsch[1,2,3]

Received: 7 April 2020 / Revised: 2 June 2020 / Accepted: 6 July 2020 / Published online: 14 July 2020

Abstract

Background Objective and volumetric quantification is a necessary step in the assessment and comparison of endolymphatic hydrops (ELH) results. Here, we introduce a novel tool for automatic volumetric segmentation of the endolymphatic space (ELS) for ELH detection in delayed intravenous gadolinium-enhanced magnetic resonance imaging of inner ear (iMRI) data.

Methods The core component is a novel algorithm based on Volumetric Local Thresholding (VOLT). The study included three different data sets: a real-world data set (D1) to develop the novel ELH detection algorithm and two validating data sets, one artificial (D2) and one entirely unseen prospective real-world data set (D3). D1 included 210 inner ears of 105 patients (50 male; mean age 50.4 ± 17.1 years), and D3 included 20 inner ears of 10 patients (5 male; mean age 46.8 ± 14.4 years) with episodic vertigo attacks of different etiology. D1 and D3 did not differ significantly concerning age, gender, the grade of ELH, or data quality. As an artificial data set, D2 provided a known ground truth and consisted of an 8-bit cuboid volume using the same voxel-size and grid as real-world data with different sized cylindrical and cuboid-shaped cutouts (signal) whose grayscale values matched the real-world data set D1 (mean 68.7 ± 7.8; range 48.9–92.8). The evaluation included segmentation accuracy using the Sørensen-Dice overlap coefficient and segmentation precision by comparing the volume of the ELS.

Results VOLT resulted in a high level of performance and accuracy in comparison with the respective gold standard. In the case of the artificial data set, VOLT outperformed the gold standard in higher noise levels. Data processing steps are fully automated and run without further user input in less than 60 s. ELS volume measured by automatic segmentation correlated significantly with the clinical grading of the ELS ($p < 0.01$).

Conclusion VOLT enables an open-source reproducible, reliable, and automatic volumetric quantification of the inner ears' fluid space using MR volumetric assessment of endolymphatic hydrops. This tool constitutes an important step towards comparable and systematic big data analyses of the ELS in patients with the frequent syndrome of episodic vertigo attacks. A generic version of our three-dimensional thresholding algorithm has been made available to the scientific community via GitHub as an ImageJ-plugin.

Keywords Endolymphatic hydrops · Inner ear · MRI · Intravenous application · Contrast agent · Volumetric · Local thresholding · Automatic segmentation

✉ V. Kirsch
valerie.kirsch@med.lmu.de

[1] Department of Neurology, University Hospital, Ludwig-Maximilians-Universität München, Marchioninistraße 15, 81377 Munich, Germany

[2] German Center for Vertigo and Balance Disorders – IFB-LMU, University Hospital, Ludwig-Maximilians-Universität München, Munich, Germany

[3] Graduate School of Systemic Neuroscience (GSN), Ludwig-Maximilians-Universität München, Munich, Germany

[4] Department of Radiology, University Hospital, Ludwig-Maximilians-Universität München, Munich, Germany

[5] Department of Radiology, The Hospital for Sick Children, University of Toronto, Toronto, Canada

[6] Munich Cluster for Systems Neurology (SyNergy), Munich, Germany

Abbreviations

3D	Three-dimensional
Bl	Blurriness
BPPV	Benign paroxysmal positional vertigo
BVP	Bilateral vestibulopathy
CISS	Constructive interference in steady-state
DS	Dice score
DSGZ	Interdisciplinary German Center for Vertigo and Balance Disorders
EF	Endolymphatic fluid
ELH	Endolymphatic hydrops
ELS	Endolymphatic space
FLAIR	Fluid-attenuated inversion recovery
GRAPPA	Generalized auto-calibrating partially parallel acquisition
iMRI	Delayed intravenous gadolinium-enhanced magnetic resonance imaging of the inner ear
iv	Intravenous
L	Left
R	Right
MD	Menière's disease
MRI	Magnetic resonance imaging
NEF	Non–endolymphatic fluid
ROC	Receiver operating characteristics
Sc	Scatter
SD	Standard deviation
SVV	Subjective visual vertical
TLS	Total fluid space
U	Unclear
V_E	Volume of the endolymphatic space
V_T	Volume of the total fluid space
vHIT	Videooculography during the head-impulse test
VM	Vestibular migraine
VN	Vestibular neuritis
VP	Vestibular paroxysmia

Introduction

Delayed intravenous gadolinium-enhanced magnetic resonance imaging of the inner ear (iMRI) enables direct, in-vivo, non-invasive verification of endolymphatic hydrops (ELH) simultaneously in both inner ears [1]. This reasonably recent methodical development introduced a broader, more structured investigation to the clinical syndromes associated with ELH, which up to then was thought to be pathognomonic to Menière's disease (MD) [2]. Today, the relationship between ELH and MD symptoms (for review cp [3]), as well as the specificity of ELH for MD, has come under scrutiny. The underlying reason is that different ELH patterns can be found not only in MD [4, 5], but also so far in 3.3–28% of healthy ears [6, 7], various inner ear [8–10] and central [11–14] pathologies, as well as in anatomic or vascular abnormalities affecting endolymph resorption [15–17].

Because of this, objective and volumetric quantification is considered a necessary step to assess and compare ELH results. So far, the clinical gold standard assessment of the endolymphatic space (ELS) is based on a semi-quantitative and subjective grading reliant on a few MR slices in a transversal plane. Current ELS MR volumetric assessment approaches propose either manual or semi-automatic segmentation [18]. Already a considerable improvement, these approaches lack normalization and require lengthy user interaction that is not suitable for use in more extensive group studies or clinical routine.

Here, we introduce a novel tool for automatic volumetric segmentation of the ELS for ELH detection in iMRI data. The core component is a novel three-dimensional algorithm based on Volumetric Local Thresholding (VOLT). The tool was validated on artificial and prospective real-world data sets.

Materials and methods

Data sets

The study included three different data sets: data set 1 (D1, *development data set*) was used to develop the novel ELH detection algorithm based on Volumetric Local Thresholding (VOLT). Data set 2 (D2, artificial validation data set) and data set 3 (D3, prospective validation data set) were used to validate VOLT on entirely unseen data.

D1 and D3 included real-world data sets from consecutive patients from the interdisciplinary German Center for Vertigo and Balance Disorders (DSGZ) of the Munich University Hospital (LMU) between 2015 and 2019. Institutional Review Board approval was obtained before the initiation of the study (no 64115). Included patients had presented with episodic vertigo attacks [19] and undergone iMRI as part of their indicated clinical diagnostic workup to evaluate their ELS. Their data sets were included after they had given oral and written consent following the Declaration of Helsinki. The inclusion criteria were age above 18 years. Exclusion criteria were any MR-related contraindications [20], poor image quality, or missing MR sequences. D1 included 210 inner ears of 105 consecutive patients (50 male; aged 19–84 years, mean age 50.4 ± 17.1 years), and D3 included 20 inner ears of 10 consecutive patients (5 male, aged 31–69 years, mean age: 46.8 ± 14.4 years). D1 and D3 did not differ significantly concerning age, gender, the grade of endolymphatic hydrops (ELH), or data quality (intensity, mean grayscale value). A detailed description of D1and D3 is given in Table 1.

Journal of Neurology (2020) 267 (Suppl 1):S185–S196

Table 1 Description of the real-world data sets

	N (gender)	Age	Diagnosis	ELH	ELH grade	Data Quality
D1	105 (50 male)	50.4 ± 17.1 range 19–84	32% VM (*n* = 33) 28% MD (*n* = 29) 18% NV (*n* = 19) 17% VP (*n* = 18) 3% BVP (*n* = 4) 2% BPPV (*n* = 2)	97 out of 210 ears 46.2%	0.7 ± 0.8 Range 0–3	1.1 ± 0.3 Range 0.3–2.3
D3	10 (5 male)	46.8 ± 14.4 range 31–69	10% VM (*n* = 1) 70% MD (*n* = 7) 10% NV (*n* = 1) 10% BPPV (*n* = 1)	7 out of 20 ears 35%	0.7 ± 0.9 Range 0–2.5	1.1 ± 0.3 Range 0.3–1.6

D1 and D3 included data sets from consecutive patients from the interdisciplinary German Center for Vertigo and Balance Disorders (DSGZ), Munich, Germany. Included patients had presented with episodic vertigo attacks and undergone delayed intravenous gadolinium-enhanced magnetic resonance imaging of the inner ear (iMRI) as part of their indicated clinical diagnostic workup. Patients were clinically diagnosed according to the several international guidelines, most of the classification committee of the international Bárány Society (https://www.jvr-web.org/ICVD.html or https://www.baranysociety.nl) and included the diagnosis of VM [23], MD [24], VP [25], BPPV [26], BVP [1] and acute unilateral vestibulopathy/vestibular neuritis [2]. Grading of the ELH in the vestibulum and cochlea was based on criteria described previously [3], which constitutes a fusion of two classification systems [4, 5]. D1 and D3 did not differ significantly concerning age, gender, the grade of ELH, or data quality

±standard deviation, *BPPV* benign paroxysmal positional vertigo, *BVP* bilateral vestibulopathy, *ELH* endolymphatic hydrops, *ELS* endolymphatic space, *iMRI* delayed intravenous gadolinium-enhanced magnetic resonance imaging of the inner ear, *MD* Menière's disease, *N* number of participants, *VM* vestibular migraine, *VP* vestibular paroxysmia

As an artificial data set, D2 provided a known ground truth to test and compare VOLT's performance to an adapted version of Otsu's method [21], which is a recognized foreground/background segmentation algorithm based on global thresholding at an optimal histogram-derived cutoff. D2 consisted of an 8-bit cuboid volume using the same voxel-size and grid as real-world data with different sized cylindrical and cuboid-shaped cutouts (signal) whose grayscale values matched the real-world data set D1 (mean 68.7 ± 7.8; range 48.9–92.8). To this structural basis signal, two types of noise were added, which imitate the real-world variability of MRI signals [22]. The noise was added stepwise in the form of increasing blurriness noise (Gaussian blur kernel, SD range 1–6 voxel in x/y/z-direction; SD = standard deviations) or increasing scatter noise (Gaussian, SD range of intensity variation: 0–50 SD). D2 and its varying levels of noise can be viewed in Fig. 1a.

D1 and D3–Clinical diagnosis and measurement of the auditory, semicircular canal, and otolith functions

Patients were clinically diagnosed according to the international guidelines, most of the classification committee of the international Bárány Society (www.jvr-web.org/ICVD.html or www.baranysociety.nl) for the diagnosis of vestibular migraine [23], Menière's disease [24], vestibular paroxysmia [25], bilateral vestibulopathy [26], acute unilateral vestibulopathy/vestibular neuritis [27] and benign paroxysmal positional vertigo [28]. The diagnoses of the patients within D1 and D3 can be viewed in Table 1.

Diagnostic workup included a careful neurological and neuro-otological examination including neuro-orthoptic assessment (e.g., Frenzel goggles; fundus photography and adjustments of the subjective visual vertical (SVV) for graviceptive vestibular function, for methods, see [29]), video-oculography during the head-impulse test (vHIT) for dynamic vestibular function (for methods, see [30, 31]), audiometry, and MR imaging of the whole brain including the cerebellopontine angle and brainstem.

D1 and D3–Sequence protocol and grading of the delayed gadolinium-enhanced ivMRI of the inner ear

Four hours after intravenous injection of a standard dose (0.1 ml/kg body weight, i.e., 0.1 mmol/kg body weight) of Gadobutrol (Gadovist®, Bayer, Leverkusen, Germany), MR imaging data were acquired in a whole-body 3 T MR scanner (Magnetom Skyra, Siemens Healthcare, Erlangen, Germany) with a 20-channel head coil. Head movements were minimalized in all three axes using a head positioning system for MRI (Crania Adult 01, Pearl Technology AG, Schlieren, Switzerland). A 3D-FLAIR sequence was used to differentiate endolymph from perilymph and bone, and a CISS sequence to delineate the total inner ear fluid space from the surrounding bone. A T2-weighted, three-dimensional, fluid-attenuated inversion recovery sequence

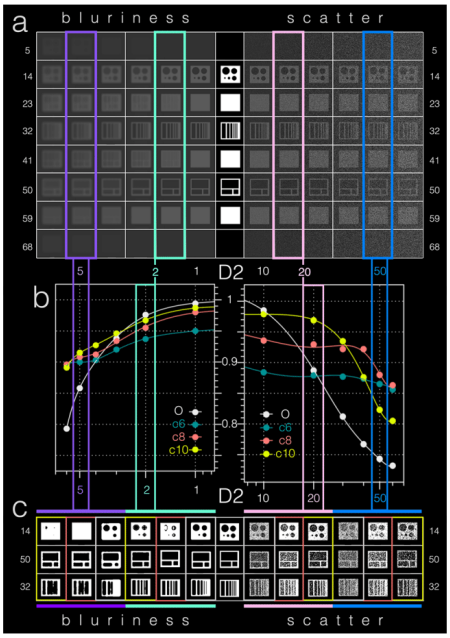

Fig. 1 D2 artificial data set–visualization and results. As an artificial data set, D2 provided a known ground truth to test and compare VOLT cutoff versions to Otsu's method. **a** A transversal slice-wise visualization of D2 in the middle. D2 can be viewed in the very middle and included an 8-bit cuboid volume with different sizes of cylindrical and cuboid-shaped cutouts (signal). To this signal different types of real-world MRI imitating noise were added stepwise in the form of increasing blurriness (Gaussian blur kernel, SD range 1–6 voxel in x/y/z-direction; SD = standard deviations, visualized to the left) and increasing scatter (SD range of intensity variation: 0–50 SD, visualized to the right). **b** Based on empirical observations in the development data set (D1), VOLT was compared to Otsu's method (O = grey) at three cutoff variations (c6 = forest green, c8 = red, c10 = yellow). Both VOLT cutoff versions and Otsu's method fared better with blurriness noise (*x*-axis of the left graph) in comparison with scatter noise (*x*-axis of the right graph). More specifically, VOLT cutoff versions showed a high level of agreement in terms of Dice overlap (*y*-axis within the graphs) with Otsu's scores in data sets with low noise levels (please compare blurriness 2, framed in mint green and scatter 20, framed in pink). The higher the noise level, the more VOLT cutoff versions outperformed Otsu's method (please note blurriness 5, framed in purple and scatter 50, framed in blue). The corresponding output (**c**) can easily be compared with the ground-truth by following said color frames. *D2* data set 2, *c6* cutoff 6, *c8* cutoff 8, *c10* cutoff 10, *O* Otsu's method

(3D-FLAIR) with the following parameters: TR 6000 ms, TE 134 ms, TI 2240 ms, FOV 160 × 160 mm^2, 36 slices, base resolution 320, averages 1, acceleration factor of 2 using a parallel imaging technique with a generalized auto-calibrating partially parallel acquisition (GRAPPA) algorithm, slice thickness 0.5 mm, acquisition time 15:08 min was carried out. A high-resolution, strongly T2-weighted, 3D constructive interference steady state (CISS) sequence of the temporal bones was performed to evaluate the anatomy of the whole-fluid-filled labyrinthine spaces with the following parameters: TR 1000 ms, TE 133 ms, FA 100°, FOV 192 × 192 mm^2, 56 slices, base resolution 384, averages 4, acceleration factor of 2 using GRAPPA algorithm, slice thickness of 0.5 mm and acquisition time 8:36 min. The presence of ELH was observed on the 3D-FLAIR images as enlarged negative-signal spaces inside the labyrinth, according to a previously reported method [32, 33]. The decision to apply a single-dose contrast agent was made because of the ongoing discussion about gadolinium deposition within the dentate nucleus and globus pallidus after repeated administration of gadolinium-based contrast agents [34–37]. It was not considered ethical to apply higher doses of contrast agent if not necessary. Accordingly, only patients with a diagnostic benefit were included in the study.

Evaluation of the iMRI and grading of the ELS was performed independently by two experienced head and neck radiologists and a neurologist who was blinded to the clinical patient data. If discrepancies arose, a consensus was reached by discussion. The characterization of the ELS in the vestibulum and cochlea was based on criteria previously described [12], which constitutes a fusion of two classification systems [38, 39]. D1 and D3 did not differ significantly concerning the grade of ELH. An overview of ELH grade and data quality for data sets D1 and D3 can be viewed in Table 1.

D1–Development of the automatic segmentation tool for ELH detection based on Volumetric Local Thresholding (VOLT)

VOLT was developed on the real-world data set D1 using exclusively universal access software, namely 3D Slicer version 4.11 toolbox [40] including the TOMAAT plugin [15], as well as ImageJ Fiji [41] including the "Fuzzy and artificial neural networks image processing toolbox" [42] and the "MorphoLibJ Toolbox" [43](see an overview of the overall pipeline including VOLT-based ELS segmentation in Fig. 2a, b).

Data pre-processing included the following steps

VOLT operates on a pre-segmented region-of-interest (ROI) of the inner ear, which requires a series of data pre-processing steps. First, FLAIR and CISS sequences were interpolated to a voxel size of 0.25 mm × 0.25 mm × 0.25 mm using a bicubic interpolation algorithm in ImageJ. Then, left and

Journal of Neurology (2020) 267 (Suppl 1):S185–S196

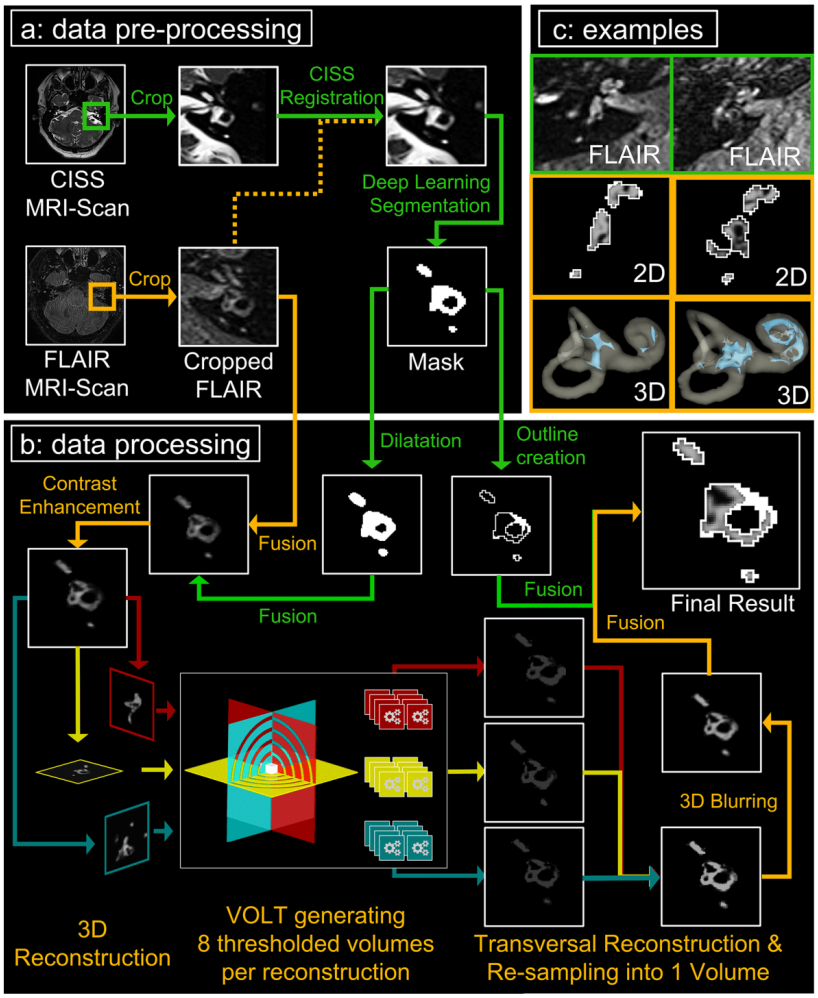

Fig. 2 VOLT flowchart and output examples. The flowchart shows a step-by-step overview of the VOLT processing pipeline of a left inner ear. The different steps correspond to the boxes in a counterclockwise fashion (a, b, c). **a** Describes data pre-processing, **b** data processing, and **c** shows output examples. Within each box, processing steps following orange arrows indicate the order of the main program steps, and green arrows indicate supporting steps. Data pre-processing (a) consists of cropping the inner ear from CISS and FLAIR MR images (only step requiring user input), co-registration, and using a cloud-based deep convolutional neural network (CNN) to create a mask of the inner ear. During data processing, (b) the mask is dilated to include a small seam around the inner ear region-of-interest (ROI). Then, a fusion volume is created, contrast-enhanced, and the fusion volume is 3D reconstructed. VOLT is performed, volumes are reconstructed into a transversal plane and re-sampled into one volume. After 3D blurring, single-voxel noise is removed, and a three-dimensional outline based on the mask is added to the final result. (c) depicts two output examples of the right inner ear. The upper row shows the corresponding cropped FLAIR-MR image; the middle row shows a 2D depiction of the VOLT output, and the lower row shows the 3D visualization of VOLT-output. The inner ear to the left displays no endolymphatic hydrops (ELH). The inner ear to the right displays an ELH grade 2. *CISS* constructive interference in steady-state, *MR* magnetic resonance, *FLAIR* fluid-attenuated inversion recovery, *VOLT* volumetric local thresholding

right inner ears were cropped using a rectangular selection, converted to nrrd-files, and imported into 3D-Slicer. To obtain an ROI of the overall inner ear region, a voxel-wise segmentation of this cropped region needed to be obtained. To this end, we applied a recently proposed deep convolutional neural network (CNN), deployed via the TOMAAT module in 3D–Slicer [44]. This step first normalizes the orientation of the cropped volume by affine image registration (BRAINSFit toolkit [45]) and then applies a pre-trained volumetric CNN with V-net architecture [46]. The V-net output yields a segmentation into two labels, either inner ear or background. The "inner-ear" segmentation, hereafter referred to as "mask", was converted into an 8-bit binary volume and volumetrically dilated using 3D morphological filtering. As dilation adds a thin shell of anatomy surrounding the inner ear, this step allows the amount of false-negative classifications by the VOLT segmentation algorithm to be reduced. An overview of the pre-processing required for VOLT-based ELS segmentation can be viewed in Fig. 2a.

Data processing included the following steps

Two locally adaptive thresholding algorithms ("Bernsen" [47] and "Mean") were used in the three planes, and in four varying radii, respectively, to differentiate between endolymphatic fluid (EF) and non–endolymphatic fluid (NEF). These intermediate segmentations were then reconstructed in a transversal plane and aggregated into one final segmentation volume. Close attention was paid to avoid the inclusion of false positives into the ELS, by considering only voxels within a volumetrically strict outer shell of the inner ear (see pre-processing). As a next step, single-voxel-noise was reduced using a 3D Gaussian blurring algorithm. The first mask was used to create a single pixel-sized borderline (= 0.25 mm) in all three planes to ultimately avoid false-positive classifications in the corner regions of these three planes. The resulting 3D volume can then be regarded as a probabilistic map of the inner ear, which included the classification into its two different compartments (endolymphatic and perilymphatic space). The final classification then strongly depends on the chosen cutoff. Each cutoff matches a percentage of positive classifications. For example, cutoff 6 (c6) corresponds to 79.2%, cutoff 8 (c8) to 70.8% and cutoff 10 (c10) to 62.5% classifications into endolymphatic space. Based on empirical observations in the development data set (D1), VOLT was validated at three cutoff variations (c6, c8, c10; Fig. 2b).

Automatization and pipeline creation

A script written in the IJ1M-macro-language was used to automate pre-processing and processing in FIJI. User input was required solely for supervision purposes during cropping, registration, and segmentation. The remaining features (pre-processing, volumetric reconstruction, contrast enhancement, fusion, thresholding, and post-processing) work automatically.

D1, D2 and D3–Methods for validation

VOLT with three different cutoffs (c6, c8, c10) was validated on the artificial data set D2 and the prospective real-world data set D3. Segmentation accuracy was evaluated using the Sørensen-Dice overlap coefficient, which is defined as $2 * |X \cap Y|/|X| + |Y|$ for segmentations X and Y [48], as a measure of region overlap between gold standard segmentation and the automatically obtained segmentations from the VOLT pipeline.

Segmentation precision was estimated by comparing the volume of the ELS (V_E) between segmentation methods. Structurally, the human inner ear can be pictured as an external, bony hose system (called the bony labyrinth, containing perilymph) and an inner hose system (called the membranous labyrinth, containing endolymph). The total lymph fluid space includes the inner hose system's ELS and the surrounding perilymphatic space.

Receiver operating characteristics (ROC) analysis was used to show the (in)dependence of the performance of the methods from the grade of the ELH or the distribution of the fluids within the total fluid space (TFL) and the SNR of the iMRI data set.

D1, D2 and D3 statistics and map display

The data were analyzed with SPSS 20.0 (SPSS, Chicago, IL, USA). Differences between data sets overall were assessed using a paired t-test, which was Bonferroni-corrected for multiple testing and viewed at $p < 0.01$ and $p < 0.05$. Linear agreement between parameter pairs was calculated for each method separately using the two-sided Spearman's correlation coefficient and reported at a significance level of $p < 0.01$ and $p < 0.05$. For Receiver operating characteristics (ROC) analysis, the original Fortran program JLABROC4 (by Charles Metz and colleagues, Department of Radiology, University of Chicago; Java translation by John Eng, Russel H Morgan Department of Radiology and Radiological Science, Johns Hopkins University, Baltimore, Maryland, USA, Version 2.0, March 2017) was used.

Results

VOLT implementation on D1

After implementation on data set D1, the novel tool for automatic segmentation of the endolymphatic space (ELS) with

a novel algorithm based on Volumetric Local Thresholding (VOLT) ran smoothly and showed no operational or stability issues. VOLT does not require especially powerful hardware or closed-source software. The only prerequisite is the installation of universal access software, namely 3D Slicer toolbox [40] including the TOMAAT plugin [15], as well as ImageJ Fiji [41] including the "Fuzzy and artificial neural networks image processing toolbox" [42] and the "MorphoLibJ Toolbox" [43].

The only step requiring user input was the cropping step. While this step required a rough selection of the inner ear and could easily be automatized, it allowed a quick and easy visual assessment of the source images and was therefore considered a suitable quality control mechanism. Cropping was performed in order to reduce computation time as well as allow for easier registration of the inner ears; the registration step was necessary to ensure correct positioning of the CISS-based hull relative to the FLAIR. For both registration and CNN segmentation, the necessary user input was limited to entering parameters and starting the process. After the CNN segmentation the user had to save the segmentations as a new file manually. As an orientation, pre-processing steps of one single-subject data set can be performed in less than ten minutes by an experienced user on a standard consumer laptop (Windows10 (64Bit), Intel® Core i5-4200U @1,6 GHz, 8 GB RAM).

Data processing steps are fully automated and run without further user input in less than 60 s. Volumetric local thresholds can be adapted to signal-to-noise ratio (SNR) of different data sets. Output files include 3D volumetric quantification of TLS and ELS in mm^3 and a 3D visualization of the inner ear. Examples of single-subject VOLT-based inner ear segmentations show different grades of ELH (Fig. 2c).

VOLT performance on artificial data set D2

D2 was created to have a ground truth data set featuring challenges found in inner ear imaging, namely low contrast and high noise. Similar to actual iMRI, the regions of interest were three-dimensional volumes of different sizes. This proofed to be difficult for 2D-algorithms, whereas three-dimensional methods could analyze the data set better.

As an artificial data set, D2 provided a known ground truth to test and compare VOLT's performance to an adapted version of Otsu's method (O) [21], which is a recognized foreground/background segmentation algorithm based on global thresholding at an optimal histogram-derived cutoff. Based on empirical observations in the development data set (D1), VOLT was compared to O at three cutoff variations (c6, c8, c10). On average, over all noise conditions, the Dice score (DS) of VOLT cutoff versions (c6: 90%, c8: 92%; c10: 92%) outperformed Otsu's method (82%). Both VOLT cutoff versions and Otsu's method fared better with blurriness noise (DS:O: 91%; c6: 92%, c8: 93%; c10: 94%) in comparison with scatter noise (DS O: 82%; c6: 87%, c8: 91%; c10: 90%). More specifically, VOLT cutoff versions showed a high level of agreement in terms of Dice overlap with Otsu's scores in data sets with low noise levels (Bl 1–4; Sc 10). The higher the noise level, however, the more VOLT cutoff versions outperformed Otsu's method (Bl 5–6; Sc 20–60), with c8 showing an overall best performance independent of noise levels. All results are presented in Table 2 and Fig. 1b, c.

VOLT performance on prospective real-world data set D3

D3 included previously entirely unseen real-world data sets from 10 consecutive patients (=20 inner ears) and was used to validate VOLT on entirely unseen data. Ear-specific segmentation accuracy was evaluated using the Sørensen-Dice overlap coefficient (DS), and segmentation precision were estimated by comparing the volume of the ELS (V_E). Performance (DS) of VOLT with the three different cutoffs c6: 97.0% ± 0.7, c8: 96.6% ± 0.8, c10: 95.9% 97% ± 0.9) highly overlapped with the manual segmentation. On average, c8 gave a close representation of the actual volume seen in the manual segmentation, while c6 tended to underestimate and c10 to overestimate the endolymphatic space volume methodically. Note that the grade of ELH correlated significantly with the endolymphatic volume of both the manual segmentation method (two-sided, $r(18)=0.475$, $p=0.034$) and with VOLT cutoff variations c6 (two-sided, $r(18)=0.553$, $p=0.011$)–c8 (two-sided, $r(18)=0.566$, $p=0.009$)–c10 (two-sided, $r(18)=0.569$, $p=0.009$). Receiver operating characteristics (ROC) analysis showed the grade of the ELH to be a good classifier for the computed volume of the ELS (fitted ROC area: 0.9). Table 2 shows an overview of the performance and accuracy results of each segmentation method. Figure 3 gives an ear-specific overview of each validation parameter.

Discussion

An open-source tool for automatic volumetric segmentation of the endolymphatic space (ELS) for endolymphatic hydrops (ELH) detection in intravenous, delayed, gadolinium-enhanced magnetic resonance imaging of the **i**nner ear (iMRI) data was developed on a real-world data set including 210 inner ears. The core component is a novel algorithm based on Volumetric Local Thresholding (VOLT). Tool validation in two data sets, one artificial data set that provided a known ground truth and one real-world that included 20 previously unseen inner ears, resulted in a high level of performance and accuracy in comparison with the respective

Table 2 Overview of results

A

Data set	Noise	Scale	Otsu's	Cutoff 6	Cutoff 8	Cutoff 10
D2	BI	1	99.4%	95.0%	98.0%	98.7%
		2	97.6%	93.7%	95.5%	96.7%
		3	93.8%	92.0%	93.4%	94.6%
		4	90.3%	90.3%	91.2%	92.7%
		6	85.8%	90.0%	90.8%	91.5%
	Sc	10	98.5%	88.4%	93.6%	97.9%
		20	88.7%	87.9%	93.0%	96.9%
		30	81.2%	87.7%	92.2%	93.5%
		40	76.7%	87.4%	90.5%	87.6%
		50	74.3%	86.5%	88.0%	82.3%
		60	73.2%	85.6%	86.3%	80.5%

B

Data set	Validation	M	Cutoff 6	Cutoff 8	Cutoff 10
D3	DS	Gold standard	97.0% ± 0.7 range 95.6–97.9	96.6% ± 0.8 range 95.0–97.7	95.9% ± 0.9 range 93.8–97.2
	V_E	16.7 mm^3 ± 5.5 range 8.8–30.7	11.5 mm^3 ± 5.7 range 5.0–25.5	17.1 mm^3 ± 7.4 range 8.4–33.6	23.3 mm^3 ± 8.7 range: 13.0–41.0
	V_E/M	1	0.7 ± 0.2 range 0.4–0.9	1 ± 0.2 range 0.7–1.5	1.4 ± 0.3 range 1.0–2.1
	V_T	276.2 mm^3 ± 37.6 (range 223.6–347.6)			

As an artificial data set, D2 provided a known ground truth to test and compare VOLT cutoff versions to Otsu's method (O). **A** shows an overview of the Dice scores (DS) of each segmentation method (Otsu's, cutoff 6, cutoff 8, cutoff 10) concerning the real-world MRI imitating noise that was added stepwise in the form of increasing blurriness noise (Bl, Gaussian blur kernel, SD range 1–6 voxel in x/y/z-direction; SD = standard deviations) or increasing scatter noise (Sc, SD range of intensity variation: 0–50 SD). For visualization of the added noise and results, see Fig. 1a. D3 included real-world data sets from consecutive patients from the interdisciplinary German Center for Vertigo and Balance Disorders, Munich, Germany. Part **B** shows an overview of the results' mean of each segmentation method (manual segmentation that was considered as the gold standard and VOLT with three different cutoffs 6, 8, 10). Segmentation accuracy was evaluated using the Sørensen-Dice overlap coefficient, and segmentation precision were estimated by comparing the volume of the ELS (V_E). The ratio V_E/M was supplied to show the deviation of each cutoff from the gold standard, which was the manual segmentation. The V_E ranges include all different grades of endolymphatic hydrops

± standard deviation, *Bl* blurriness, *DS* Dice score, *Sc* scatter, V_E volume of the endolymphatic space, V_T volume of the total fluid space

gold standard (Otsu's method and manual segmentation). In the case of the artificial data set, VOLT outperformed the gold standard in higher noise levels. VOLT endolymph volume significantly correlated with the clinical grading of the ELS. VOLT operates on a pre-segmented region-of-interest (ROI) of the inner ear, which requires a series of data preprocessing steps (duration < 10 min). Data processing steps are fully automated and run without further user input in less than 60 s.

VOLT–performance and usability

Objective and volumetric quantification is a necessary step to assess and compare ELH results between studies and hospitals. So far, the clinical gold standard assessment of the ELS is based on a semi-quantitative and subjective grading reliant on a few MR slices in the transversal plane. In addition, different ELH classifications are being used in parallel [38, 39, 49, 50]. While manual volumetric segmentation is the gold standard for volumetric quantification, it is highly subjective and dependent on the rater's experience and knowledge, not to mention time-consuming. VOLT allows objective, easily reproducible, and reliable stand-alone volumetric ELH quantification and grading, which closely matches manual segmentation, highly correlates with clinical ELH grading, and performs particularly well in data with a low signal-to-noise ratio.

The main advantage of VOLT is its local thresholding algorithm, which enables more flexible and stable results in comparison to global thresholding algorithms (such as Otsu's method). Inhomogeneous image intensities and local brightness variations are adequately compensated for [48, 51]. The robustness and flexibility of VOLT to image artifacts can be further increased using different radius sizes. Importantly, results in Fig. 1 demonstrate that VOLT does not yield perfect segmentation in the absence of noise (not probable in real-world data), but instead

Journal of Neurology (2020) 267 (Suppl 1):S185–S196

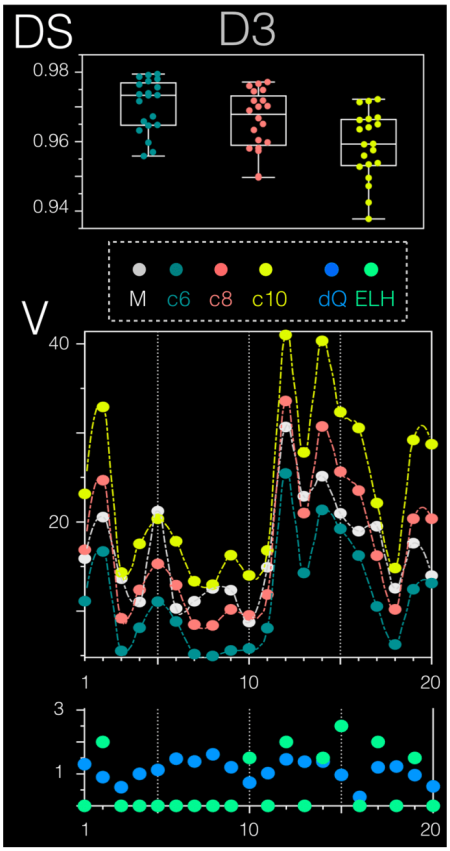

Fig. 3 D3 prospective validation data set results. D3 was used to validate VOLT on entirely unseen real-world data (20 inner ears). VOLT with the three variations cutoff 6 (c6 = dark green), cutoff 8 (c8 = red), and cutoff 10 (c10 = yellow) were compared to manual (M) segmentation (= grey, that was considered the gold standard). Ear-specific segmentation accuracy was evaluated using the Sørensen-Dice overlap coefficient (DS, upper graph), and segmentation precision were estimated by comparing the volume of the ELS (V, middle graph). Overall, DS of all three VOLT variations was high (c6: 97.0%± 0.7, c8: 96.6%± 0.8, c10: 95.9% 97%± 0.9). The influence of endolymphatic hydrops (ELH = colored light green) and data quality (dQ = colored blue) can easily be seen in the lowest graph. Data quality was defined as mean the greyscale value (or intensity). Note that the grade of ELH correlated significantly with the endolymphatic volume of both the manual segmentation method ($p < 0.05$) and VOLT cutoff variations c6-8–10 ($p < 0.01$). *c*6 cutoff 6, *c*8 cutoff 8, *c*10 cutoff 10, *D*3 data set 3, *dQ* data quality, *DS* Dice score, *M* manual segmentation

performs more favorably and more stably in the presence of increased noise (very probable in real-world data).

Current ELS MR volumetric assessment approaches remain few and involve a manual or semi-automatic segmentation [6, 18, 50, 52]. Already a considerable improvement, these approaches require lengthy user interaction that is not suitable for use in more extensive group studies or clinical routine. Also, the software used tends to be attached to expensive software, and the uncompiled source is not available for public review.

VOLT runs smoothly and does not require especially powerful hardware or closed-source software. As an orientation, pre-processing steps of one data set can be performed in less than ten minutes by an experienced user on a standard consumer laptop. Data processing steps are fully automated and run without further user input in less than 60 s. Volumetric local thresholds can be adapted to the signal-to-noise ratio (SNR) of different data sets. Output files include 3D volumetric quantification of TLS and ELS in mm^3 and a 3D visualization of the inner ear. The endolymphatic volumes conformed to those previously reported [53, 54].

VOLT flexibility–deep learning is beneficial but not a requirement

Inner ear segmentation is a prerequisite step for VOLT-based ELH segmentation and is currently performed via a novel CNN-based deep learning approach [43], which is deployed as a module in 3D-Slicer [40]. This CNN was trained in-house at our department, on a separate iMRI data set obtained on the same MRI scanner and with the same imaging sequence parameters as our study. As such, this method was a natural choice for inner ear ROI segmentation in our data set, especially because segmentations were not only highly accurate but also obtainable in comparably fast execution time (< 5 s). A downside is that this network likely has difficulties in generalizing to data from other scanners or imaging sequence settings, e.g., from other clinics. Therefore, we do not assume a TOMAAT/V-Net segmentation as a fixed component of the current ELH segmentation pipeline. The inner ear ROI can also be obtained by other segmentation approaches, most prominently using atlas-based registration. Recently, two in-vivo MRI atlases and templates were proposed, one offering a probabilistic segmentation of the inner ear's bony labyrinth [46], the other offering a high-resolution multivariate template for T1-, T2- and CISS-weighted MRI imaging [41]. Both atlases can yield accurate segmentation of the inner ear ROI while being much more generalizable to MRI data from previously unseen scanners or acquisition sites, in particular, if multivariate MRI appearances are available as in [41]. The downside of atlas-based segmentation is the high computational complexity of deformable atlas registration algorithms that align the atlas

to the target volume. With carefully tuned parametrizations, such algorithms can achieve highly accurate segmentation, but segmentations can take 10 min to 2 h per volume [47], compared to < 5 s computation time for deep neural nets such as [43]. Overall, we, therefore, recommend the usage of deep neural nets for inner ear segmentation predictions; however, the correct way to generalize the network to new sites, e.g., via transfer learning, remains to be established in future work.

Methodical limitations

There are methodical limitations in the current study that need to be considered in the interpretation of the data. First, the performance of VOLT is highly dependent on the segmentation of the inner ear. An inner ear mask that includes parts of the dark background voxels surrounding the inner ear structures would lead to a false-positive attribution to the ELS. VOLT's high performance and accuracy values are probably in part attributable to the novel CNN-based deep learning approach. Second, VOLT does not include any anatomical knowledge. In the best case, this means that the algorithm is entirely unbiased, i.e., not influenced by any prior morphological assumptions. The downside is a lack of exclusion of apparent errors that would be noticed by the human examiner.

An example would be segmentation errors that included surrounding structures into the ROI. A human examiner would know not to expect endolymph in the outermost tips of the cochlea or vestibulum. However, an algorithm does not. This is one reason VOLT is designed unusually strict in margin areas. Finally, VOLT (or any ELS segmentation method) is by nature highly dependent upon the resolution and contrast of the MRI raw data to be able to distinguish between endolymphatic and perilymphatic space.

Conclusion

We propose a novel pipeline for the automatic segmentation of endolymphatic hydrops in inner ear MRI. The core component is a novel algorithm based on Volumetric Local Thresholding (VOLT). Tool validation on artificial and real-world data resulted in a high level of performance and accuracy, in particular in low signal-to-noise ratio. ELS volume significantly correlated ($p < 0.01$) with the clinical grading of the ELS. A generic version of our three-dimensional thresholding algorithm has been made available to the scientific community via GitHub as an ImageJ-Plugin (https://github.com/j-gerb/3d-thresholding/tree/master).

Acknowledgements Open Access funding provided by Projekt DEAL. Partially funded by the Friedrich-Baur-Stiftung (FBS), the Graduate School of Systemic Neurosciences (GSN), the German Federal Ministry of Education and Research (BMBF) in connection with the foundation of the German Center for Vertigo and Balance Disorders (DSGZ), grant number 01 EO 0901. This is part of the dissertation of Johannes Gerb. We thank K. Göttlinger for copyediting the manuscript.

Compliance with ethical standards

Conflicts of interest The authors declare they have no competing financial interests.

References

1. Sano R, Teranishi M, Yamazaki M et al (2012) Contrast enhancement of the inner ear in magnetic resonance images taken at 10 minutes or 4 hours after intravenous gadolinium injection. Acta Otolaryngol (Stockh) 132:241–246. https://doi.org/10.3109/00016489.2011.639085
2. Nakashima T, Pyykkö I, Arroll MA et al (2016) Meniere's disease. Nat Rev Dis Primer 2:16028. https://doi.org/10.1038/nrdp.2016.28
3. Ishiyama G, Lopez IA, Sepahdari AR, Ishiyama A (2015) Meniere's disease: histopathology, cytochemistry, and imaging. Ann N Y Acad Sci 1343:49–57. https://doi.org/10.1111/nyas.12699
4. Zhang W, Hui L, Zhang B et al (2020) The correlation between endolymphatic hydrops and clinical features of Meniere disease. The Laryngoscope. https://doi.org/10.1002/lary.28576
5. Lopez-Escamez JA, Attyé A (2019) Systematic review of magnetic resonance imaging for diagnosis of Meniere disease. J Vestib Res Equilib Orientat 29:121–129. https://doi.org/10.3233/VES-180646
6. Ito T, Kitahara T, Inui H et al (2016) Endolymphatic space size in patients with Meniere's disease and healthy controls. Acta Otolaryngol (Stockh) 136:879–882. https://doi.org/10.3109/00016489.2016.1169556
7. Liu F, Huang W, Wang Z et al (2011) Non-invasive evaluation of endolymphatic space in healthy volunteers using magnetic resonance imaging. Acta Otolaryngol (Stockh) 131:247–257. https://doi.org/10.3109/00016489.2010.524938
8. Wang F, Yoshida T, Sugimoto S et al (2019) Clinical features of ears with otosclerosis and endolymphatic hydrops. Otol Neurotol Off Publ Am Otol Soc Am Neurotol Soc Eur Acad Otol Neurotol 40:441–445. https://doi.org/10.1097/MAO.0000000000002175
9. Lobo D, Tuñón M, Villarreal I et al (2018) Intratympanic gadolinium magnetic resonance imaging supports the role of endolymphatic hydrops in the pathogenesis of immune-mediated inner-ear disease. J Laryngol Otol 132:554–559. https://doi.org/10.1017/S0022215118000749

10. Eliezer M, Hautefort C, Van Nechel C et al (2020) Electrophysiological and inner ear MRI findings in patients with bilateral vestibulopathy. Eur Arch Oto-Rhino-Laryngol Off J Eur Fed Oto-Rhino-Laryngol Soc EUFOS Affil Ger Soc Oto-Rhino-Laryngol Head Neck Surg. https://doi.org/10.1007/s00405-020-05829-8
11. Fukushima M, Matsukawa N, Akahani S, Inohara H (2019) Secondary endolymphatic hydrops associated with spontaneous intracranial hypotension. JAMA Otolaryngol Head Neck Surg 145:191–193. https://doi.org/10.1001/jamaoto.2018.3073
12. Kirsch V, Becker-Bense S, Berman A et al (2018) Transient endolymphatic hydrops after an attack of vestibular migraine: a longitudinal single case study. J Neurol 265:51–53. https://doi.org/10.1007/s00415-018-8870-3
13. Ranieri A, Cavaliere M, Sicignano S et al (2017) Endolymphatic hydrops in idiopathic intracranial hypertension: prevalence and clinical outcome after lumbar puncture. Preliminary data. Neurol Sci Off J Ital Neurol Soc Ital Soc Clin Neurophysiol 38:193–196. https://doi.org/10.1007/s10072-017-2895-8
14. Murofushi T, Tsubota M, Kitao K, Yoshimura E (2018) Simultaneous presentation of definite vestibular migraine and definite Ménière's disease: overlapping syndrome of two diseases. Front Neurol 9:749. https://doi.org/10.3389/fneur.2018.00749
15. Ralli M, Greco A, Altissimi G et al (2017) Vestibular schwannoma and ipsilateral endolymphatic hydrops: an unusual association. Int Tinnitus J 21:128–132. https://doi.org/10.5935/0946-5448.20170024
16. Eliezer M, Poillon G, Lévy D et al (2020) Clinical and radiological characteristics of patients with collapse or fistula of the saccule as evaluated by inner ear MRI. Acta Otolaryngol (Stockh). https://doi.org/10.1080/00016489.2020.1713396
17. Kirsh ER, Kozin ED, Knoll RM et al (2018) Sequential imaging in patient with suspected Menière's disease identifies endolymphatic sac tumor. Otol Neurotol Off Publ Am Otol Soc Am Neurotol Soc Eur Acad Otol Neurotol 39:e856–e859. https://doi.org/10.1097/MAO.0000000000001952
18. Gürkov R, Berman A, Dietrich O et al (2015) MR volumetric assessment of endolymphatic hydrops. Eur Radiol 25:585–595. https://doi.org/10.1007/s00330-014-3414-4
19. Neuhauser HK (2007) Epidemiology of vertigo. Curr Opin Neurol 20:40–46. https://doi.org/10.1097/WCO.0b013e328013f432
20. Dill T (2008) Contraindications to magnetic resonance imaging. Heart 94:943–948. https://doi.org/10.1136/hrt.2007.125039
21. Otsu N (1979) A threshold selection method from gray-level histograms. IEEE Trans Syst Man Cybern 9:62–66. https://doi.org/10.1109/TSMC.1979.4310076
22. Stöcker T, Vahedipour K, Pflugfelder D, Shah NJ (2010) High-performance computing MRI simulations. Magn Reson Med 64:186–193. https://doi.org/10.1002/mrm.22406
23. Lempert T, Olesen J, Furman J et al (2012) Vestibular migraine: diagnostic criteria. J Vestib Res Equilib Orientat 22:167–172. https://doi.org/10.3233/VES-2012-0453
24. Lopez-Escamez JA, Carey J, Chung W-H et al (2015) Diagnostic criteria for Menière's disease. J Vestib Res Equilib Orientat 25:1–7. https://doi.org/10.3233/VES-150549
25. Strupp M, Lopez-Escamez JA, Kim J-S et al (2016) Vestibular paroxysmia: diagnostic criteria. J Vestib Res Equilib Orientat 26:409–415. https://doi.org/10.3233/VES-160589
26. Strupp M, Mandalà M, López-Escámez JA (2019) Peripheral vestibular disorders: an update. Curr Opin Neurol 32:165–173. https://doi.org/10.1097/WCO.0000000000000649
27. Strupp M, Brandt T (2009) Vestibular neuritis. Semin Neurol 29:509–519. https://doi.org/10.1055/s-0029-1241040
28. von Brevern M, Bertholon P, Brandt T et al (2017) Benign paroxysmal positional vertigo: diagnostic criteria consensus document of the committee for the classification of vestibular disorders of the Bárány society. Acta Otorrinolaringol Esp 68:349–360. https://doi.org/10.1016/j.otorri.2017.02.007
29. Dieterich M, Brandt T (1993) Ocular torsion and tilt of subjective visual vertical are sensitive brainstem signs. Ann Neurol 33:292–299. https://doi.org/10.1002/ana.410330311
30. Schneider E, Villgrattner T, Vockeroth J et al (2009) EyeSeeCam: an eye movement-driven head camera for the examination of natural visual exploration. Ann N Y Acad Sci 1164:461–467. https://doi.org/10.1111/j.1749-6632.2009.03858.x
31. Jongkees LB, Maas JP, Philipszoon AJ (1962) Clinical nystagmography. A detailed study of electro-nystagmography in 341 patients with vertigo. Pract Otorhinolaryngol (Basel) 24:65–93
32. Naganawa S, Suzuki K, Yamazaki M et al (2014) Time course for measuring endolymphatic size in healthy volunteers following intravenous administration of gadoteridol. Magn Reson Med Sci MRMS Off J Jpn Soc Magn Reson Med 13:73–80. https://doi.org/10.2463/mrms.2013-0080
33. Naganawa S, Yamazaki M, Kawai H et al (2010) Visualization of endolymphatic hydrops in Ménière's disease with single-dose intravenous gadolinium-based contrast media using heavily T(2)-weighted 3D-FLAIR. Magn Reson Med Sci MRMS Off J Jpn Soc Magn Reson Med 9:237–242. https://doi.org/10.2463/mrms.9.237
34. Barbieri S, Schroeder C, Froehlich JM et al (2016) High signal intensity in dentate nucleus and globus pallidus on unenhanced T1-weighted MR images in three patients with impaired renal function and vascular calcification. Contrast Media Mol Imaging 11:245–250. https://doi.org/10.1002/cmmi.1683
35. Stojanov D, Aracki-Trenkic A, Benedeto-Stojanov D (2016) Gadolinium deposition within the dentate nucleus and globus pallidus after repeated administrations of gadolinium-based contrast agents-current status. Neuroradiology 58:433–441. https://doi.org/10.1007/s00234-016-1658-1
36. Moser FG, Watterson CT, Weiss S et al (2018) High signal intensity in the dentate nucleus and globus pallidus on unenhanced T1-weighted MR images: comparison between gadobutrol and linear gadolinium-based contrast agents. AJNR Am J Neuroradiol 39:421–426. https://doi.org/10.3174/ajnr.A5538
37. Boyken J, Frenzel T, Lohrke J et al (2018) Gadolinium accumulation in the deep cerebellar nuclei and globus pallidus after exposure to linear but not macrocyclic gadolinium-based contrast agents in a retrospective pig study with high similarity to clinical conditions. Invest Radiol 53:278–285. https://doi.org/10.1097/RLI.0000000000000440
38. Baráth K, Schuknecht B, Naldi AM et al (2014) Detection and grading of endolymphatic hydrops in Menière disease using MR imaging. AJNR Am J Neuroradiol 35:1387–1392. https://doi.org/10.3174/ajnr.A3856
39. Nakashima T, Naganawa S, Pyykko I et al (2009) Grading of endolymphatic hydrops using magnetic resonance imaging. Acta Oto-Laryngol Suppl. https://doi.org/10.1080/00016480902729827
40. Fedorov A, Beichel R, Kalpathy-Cramer J et al (2012) 3D slicer as an image computing platform for the quantitative imaging network. Magn Reson Imaging 30:1323–1341. https://doi.org/10.1016/j.mri.2012.05.001
41. Schindelin J, Arganda-Carreras I, Frise E et al (2012) Fiji: an open-source platform for biological-image analysis. Nat Methods 9:676–682. https://doi.org/10.1038/nmeth.2019
42. Nizamutdinov V (2015) Neural network and fuzzy logic based plugins for imagej. GitHub repository. https://github.com/astartes91/imagej-neural-fuzzy-plugins
43. Legland D, Arganda-Carreras I, Andrey P (2016) MorphoLibJ: integrated library and plugins for mathematical morphology with ImageJ. Bioinforma Oxf Engl 32:3532–3534. https://doi.org/10.1093/bioinformatics/btw413

44. Milletari F, Frei J, Aboulatta M et al (2019) Cloud deployment of high-resolution medical image analysis with TOMAAT. IEEE J Biomed Health Inform 23:969–977. https://doi.org/10.1109/JBHI.2018.2885214
45. Johnson HJ, Harris G, Williams K (2007) BRAINSFit: mutual information registrations of whole-brain 3D images, using the Insight Toolkit. Insight J 57:180
46. Milletari F, Navab N, Ahmadi S-A (2016) V-Net: fully convolutional neural networks for volumetric medical image segmentation. 2016 Fourth International Conference on 3D Vision (3DV). IEEE, Stanford, pp 565–571
47. Bernsen, J (1986) Dynamic thresholding of gray level images. In: Proceedings of the International Conference on Pattern Recognition. pp 1251–1255
48. Zou KH, Warfield SK, Bharatha A et al (2004) Statistical validation of image segmentation quality based on a spatial overlap index. Acad Radiol 11:178–189. https://doi.org/10.1016/s1076-6332(03)00671-8
49. Hornibrook J, Coates M, Goh T, Bird P (2010) MRI imaging of the inner ear for Meniere's disease. N Z Med J 123:59–63
50. Homann G, Vieth V, Weiss D et al (2015) Semi-quantitative vs. volumetric determination of endolymphatic space in Menière's disease using endolymphatic hydrops 3T-HR-MRI after intravenous gadolinium injection. PLoS ONE 10:e0120357. https://doi.org/10.1371/journal.pone.0120357
51. Yang W, Cai L, Wu F (2020) Image segmentation based on gray level and local relative entropy two dimensional histogram. PLoS ONE 15:e0229651. https://doi.org/10.1371/journal.pone.0229651
52. Inui H, Sakamoto T, Ito T, Kitahara T (2016) Volumetric measurements of the inner ear in patients with Meniere's disease using three-dimensional magnetic resonance imaging. Acta Otolaryngol (Stockh) 136:888–893. https://doi.org/10.3109/00016489.2016.1168940
53. Morita N, Kariya S, Farajzadeh Deroee A et al (2009) Membranous labyrinth volumes in normal ears and Ménière disease: a three-dimensional reconstruction study. The Laryngoscope 119:2216–2220. https://doi.org/10.1002/lary.20723
54. Kendi TK, Arikan OK, Koc C (2005) Volume of components of labyrinth: magnetic resonance imaging study. Otol Neurotol Off Publ Am Otol Soc Am Neurotol Soc Eur Acad Otol Neurotol 26:778–781. https://doi.org/10.1097/01.mao.0000169635.25322.9e

3. Paper II: Intravenous Delayed Gd-Enhanced MRI

Der Inhalt dieses Kapitels wurde als “Intravenous Delayed Gadolinium-Enhanced MR Imaging of the Endolymphatic Space: A Methodological Comparative Study” veröffentlicht in:

Boegle R, Gerb J, Kierig E, Becker-Bense S, Ertl-Wagner B, Dieterich M, Kirsch V. Intravenous Delayed Gadolinium-Enhanced MR Imaging of the Endolymphatic Space: A Methodological Comparative Study. Front Neurol 2021; 12:647296.

3.1 Kurzzusammenfassung

Komparative Studien, welche Akquiseprotokolle von Innenohr-MRT (iMRI) vergleichen, fehlen bislang. In dieser Arbeit wurden 75 Patient:innen mit MM (mittleres Alter: 55.2 ± 14.9 Jahre) und 33 gesunde Probanden (mittleres Alter: 46.4 ± 15.6 Jahre) untersucht, um die MR-Eigenschaften des Endolymphraums abhängig von der Bilderstellung sowie in Zusammenschau mit den klinischen und neurophysiologischen Testergebnissen zu beurteilen sowie zu analysieren, inwieweit ein ELH selbst das MR-Signal beeinflussen kann.

Alle Probanden wurden neuro-otologisch untersucht (inklusive Wasserkalorik, Kopfimpulstest u. Hörtest). Die MRT-Daten wurden sowohl semiquantitativ als auch mittels VOLT ausgewertet.

In der Studie konnte gezeigt werden, dass Signal-Rausch-Verhältnis (SNV) und Signalintensität (SI, gemessen an mehreren manuell ausgewählten Regionen im endo- und perilymphatischen Raum, Hirnparenchym, Felsenbeingewebe sowie der Umgebung außerhalb des Schädels) weder ELH-2D- noch 3D-Quantifizierungen beeinflussen und beide miteinander hochsignifikant korrelieren, wobei die 3D-Auswertung weniger Varianz zeigte. Als klinische Parameter waren Asymmetrie-Index und räumlich normalisierter ELH (d.h. Endolymphvolumen/Innenohrvolumen) am aussagekräftigsten.

Zusammenfassend sollten 3D-Auswertungen oder international etablierte semiquantitative Methoden angewandt werden. Für die Auswertung klinischer Verlaufsparameter sind 3D-Quantifikationen am geeignetsten und damit künftig zu fordern.

3.2 Beitrag zu Paper II

RB: Studiendesign, Datenanalyse, Manuskriptentwurf. JG, EK, SB-B, und BE-W: Datenakquise, Datenanalyse, Manuskriptentwurf. MD: Studiendesign, Finanzierung, Manuskriptentwurf. VK: Studiendesign, Datenakquise, Datenanalyse, Manuskriptentwurf, Finanzierung.

3.3 Paper II (Volltext)

frontiers in Neurology

ORIGINAL RESEARCH
published: 22 April 2021
doi: 10.3389/fneur.2021.647296

Intravenous Delayed Gadolinium-Enhanced MR Imaging of the Endolymphatic Space: A Methodological Comparative Study

Rainer Boegle[1,2,3], *Johannes Gerb*[1,2], *Emilie Kierig*[1,2], *Sandra Becker-Bense*[1,2], *Birgit Ertl-Wagner*[4,5], *Marianne Dieterich*[1,2,3,6] *and Valerie Kirsch*[1,2,3]*

[1] Department of Neurology, University Hospital, Ludwig-Maximilians-Universität, Munich, Germany, [2] German Center for Vertigo and Balance Disorders-IFB (Integriertes Forschungs- und Behandlungszentrum), University Hospital, Ludwig-Maximilians-Universität, Munich, Germany, [3] Graduate School of Systemic Neuroscience (GSN), Ludwig-Maximilians-Universität, Munich, Germany, [4] Department of Radiology, The Hospital for Sick Children, University of Toronto, Toronto, ON, Canada, [5] Department of Radiology, University Hospital, Ludwig-Maximilians-Universität, Munich, Germany, [6] Munich Cluster for Systems Neurology (SyNergy), Munich, Germany

OPEN ACCESS

Edited by:
Stefan K. Plontke, Martin Luther University of Halle-Wittenberg, Germany

Reviewed by:
Alexander Gussew, Universitätsklinikum Halle, Germany
Arne Ernst, Unfallkrankenhaus Berlin, Germany

***Correspondence:**
Valerie Kirsch
valerie.kirsch@med.lmu.de

Specialty section:
This article was submitted to Neuro-Otology, a section of the journal Frontiers in Neurology

Received: *29 December 2020*
Accepted: *24 February 2021*
Published: *22 April 2021*

Citation:
Boegle R, Gerb J, Kierig E, Becker-Bense S, Ertl-Wagner B, Dieterich M and Kirsch V (2021) Intravenous Delayed Gadolinium-Enhanced MR Imaging of the Endolymphatic Space: A Methodological Comparative Study. Front. Neurol. 12:647296. doi: 10.3389/fneur.2021.647296

In-vivo non-invasive verification of endolymphatic hydrops (ELH) by means of intravenous delayed gadolinium (Gd) enhanced magnetic resonance imaging of the inner ear (iMRI) is rapidly developing into a standard clinical tool to investigate peripheral vestibulo-cochlear syndromes. In this context, methodological comparative studies providing standardization and comparability between labs seem even more important, but so far very few are available. One hundred eight participants [75 patients with Meniere's disease (MD; 55.2 ± 14.9 years) and 33 vestibular healthy controls (HC; 46.4 ± 15.6 years)] were examined. The aim was to understand (i) how variations in acquisition protocols influence endolymphatic space (ELS) MR-signals; (ii) how ELS quantification methods correlate to each other or clinical data; and finally, (iii) how ELS extent influences MR-signals. Diagnostics included neuro-otological assessment, video-oculography during caloric stimulation, head-impulse test, audiometry, and iMRI. Data analysis provided semi-quantitative (SQ) visual grading and automatic algorithmic quantitative segmentation of ELS area [2D, mm^2] and volume [3D, mm^3] using deep learning-based segmentation and volumetric local thresholding. Within the range of 0.1–0.2 mmol/kg Gd dosage and a 4 h ± 30 min time delay, SQ grading and 2D- or 3D-quantifications were independent of signal intensity (SI) and signal-to-noise ratio (SNR; FWE corrected, $p < 0.05$). The ELS quantification methods used were highly reproducible across raters or thresholds and correlated strongly (0.3–0.8). However, 3D-quantifications showed the least variability. Asymmetry indices and normalized ELH proved the most useful for predicting quantitative clinical data. ELH size influenced SI (cochlear basal turn $p < 0.001$), but not SNR. SI could not predict the presence of ELH. In conclusion, (1) Gd dosage of 0.1–0.2 mmol/kg after 4 h ± 30 min time delay suffices for ELS quantification. (2) A consensus is needed on a clinical SQ grading classification including a standardized level of evaluation reconstructed to anatomical fixpoints. (3) 3D-quantification methods of the ELS are best

suited for correlations with clinical variables and should include both ears and ELS values reported relative or normalized to size. (4) The presence of ELH increases signal intensity in the basal cochlear turn weakly, but cannot predict the presence of ELH.

Keywords: endolymphatic hydrops, endolymphatic space, inner ear imaging, gadolinium based contrast agent, intravenous, convolutional neural network, deep learning, volumetric local thresholding

INTRODUCTION

In-vivo non-invasive verification of endolymphatic hydrops (ELH) by means of delayed gadolinium (Gd) enhanced magnetic resonance imaging of the inner ear (iMRI) is rapidly developing into a standard clinical tool to investigate episodic vertigo (1–3). This is due to iMRI allowing pre-mortem detection of ELH for the first time (4, 5), demonstrating that ELH is not pathognomonic to Menière's disease (MD) (6–8), but rather a concomitant that can be found in various etiologies of episodic vertigo (9–13). Consequently, the clinical prevalence and pathophysiological significance of ELH has yet to be conclusively clarified. Understanding the underpinnings of the ELH syndrome requires a systematic investigation of pathologies involving endolymphatic space (ELS) changes as well as its base physiological condition.

Data acquisition protocols have undergone a continuous optimization of MR sequences (14, 15), as well as a steady minimization of procedural invasiveness (via a shift from intratympanic to intravenous application), duration and Gd dosage (16–18). A variety of cochlear and vestibular ELH quantification conventions have been suggested, including ELS semi-quantitative visual grading (19–25), manual measurement (26–28), semi-automatic (29, 30), and automatic algorithmic area ratio (AR), and volumetric segmentation (31, 32).

Given the plurality of approaches (some manual, some algorithmic), not all published results are inherently comparable. ELH features may vary greatly depending on ELS classification (for an overview, see **Table 1**) and data analysis choices. In this context, methodological comparative studies providing normalization and standard values between the methods and classifications used seem all the more important but still remain rare. On this note, this study aims to investigate the following questions:

(i) How variations in data acquisition protocols, such as Gd dosage or time delay, influence signal intensity (SI) and signal-to-noise ratio (SNR) within the ELS.

(ii) How ELH measures correlate with each other, as well as with clinical symptoms or neurophysiological testing.

(iii) How ELH influences SNR and SI within the ELS.

Abbreviations: ±, standard deviation; 2D, two-dimensional; 3D, three-dimensional; AR, area ratio; AI, asymmetry index; B, bilateral; c, cochlea; contra, contralateral; CEMD, central eye movement disorder; CISS, constructive interference in steady-state; d, definite; Diff-ER, ELS ratio of the side difference; DL, deep learning; ELH, endolymphatic hydrops; ELS, endolymphatic space; ER, ELS ratio; FLAIR, fluid-attenuated inversion recovery; Gd, gadolinium; GBCA, Gd-based contrast agents; Gd-DOTA, gadoteric acid (trade name: Dotarem®); Gd-Do3A, gadobutrol (trade name: Gadovist®); Gd-DTPA-BM, gadodiamide (trade name: Omniscan®); Gd-DTPA, gadopentetic acid (trade name: Magnevist®); Gd-HP-DO3A, gadoteridol (trade name: ProHance®); GLM, general linear model; GRAPPA, generalized auto-calibrating partially parallel acquisition; HC, healthy controls; HIT, head-impulse test; iMRI, delayed intravenous gadolinium-enhanced MRI of the inner ear; ipsi, ipsilateral; iv, intravenous; L, left; R, right; MD, Meniere's disease; minEn, minimum energy statistic; MMD, maximum mean discrepancy; MRI, magnetic resonance imaging; n, number; p, possible; ROI, region-of-interest; std, standard deviation; SNR, signal-to-noise ratio; SVV, subjective visual vertical; TFS, total fluid space; v, vestibulum; vHIT, video-oculography during head-impulse test; VM, vestibular migraine; VOG, video-oculography.

MATERIALS AND METHODS

Setting and Institutional Review Board Approval

All data was acquired at the Interdisciplinary German Center for Vertigo and Balance Disorders (DSGZ) and the Department of Neurology of Munich University Hospital (LMU) between 2016 and 2019. Institutional Review Board approval was obtained before the initiation of the study (no. 641-15). All participants provided informed oral and written consent in accordance with the Declaration of Helsinki before inclusion in the study.

Study Population

One hundred eight consecutive participants [75 patients with Meniere's disease (MD) and 33 vestibular healthy controls (HC)] underwent delayed intravenous gadolinium-enhanced magnetic resonance imaging (iMRI) for exclusion or verification of ELH. The diagnosis of Meniere's disease (MD) was based on the Classification Committee of the Bárány Society 2015 (33). HC were inpatients of the Department of Neurology without symptoms or underlying pathologies of the peripheral and central vestibular and auditory system that underwent MRI with a contrast agent as part of their diagnostic workup and agreed to undergo iMRI sequences after 4 h. HC underwent audio-vestibular testing to confirm the soundness of their peripheral end organs. The reasons for their admission to the clinic included movement disorders ($n = 6$), epilepsy ($n = 5$), optic neuritis ($n = 4$), trigeminal neuralgia ($n = 4$), headache ($n = 4$), idiopathic facial nerve palsy ($n = 3$), viral meningitis ($n = 3$), subdural hematoma ($n = 2$), spinal inflammatory lesion ($n = 1$), and decompensated esophoria ($n = 1$). The laterality quotient for right-handedness was assessed with the 10-item inventory of the Edinburgh test (34, 35). The inclusion criterion was age between 18 and 85 years. The exclusion criteria were other neurological or psychiatric disorders, as well as any MR-related contraindications (36), poor image quality, or missing MR sequences.

TABLE 1 | Semi-quantitative (SQ) grading conventions at a glance.

	Nakashima et al. (19)	**Gürkov et al. (24) Yang et al. (25)**	**Baráth et al. (20)**	**Attyé et al. (81)**	**Kirsch et al. (22) Boegle et al. (present data)**	**Bernaerts et al. (21) Bernaerts and de Foer (23)**
COCHLEA						
Slice of evaluation	*Midmodiolar level*	*Not specified*	*Midmodiolar level*	*Same as Nakashima et al. (19)*	*Midmodiolar level*	*Midmodiolar level*
Grade 0	No displacement of RM, interscalar septum, scala tympani, cochlear duct, scala vestibuli visible	No enlargement of ELS, PLS is clearly visible	No displacement of RM, interscalar septum, scala tympani, cochlear duct, scala vestibuli visible		**"X-mas tree"** made of circles with **"very thin, clear, hypointense line"** (cp. **Figure 1A**).	**"Very thin, clear, hypointense line"** (=non-enhancing scala media or ELS) between clearly enhancing scala vestibuli and scala tympani (=PLS)
Grade 1	Displacement of RM, cochlear duct < scala vestibuli	ELS is enlarged and bulging into PLS	Irregular dilation and partial obstruction of the scala vestibuli, cochlear duct indirectly visible as nocular black cut-out of the scala vestibuli		**"X-mas tree"** with **"X-mas lights"**, where ELS is slightly enlarged and indirectly visible as a nodular black cut out (cp. **Figure 1B**).	**"X-mas tree"** (=enhancing scala vestibuli and scala tympani) with **"X-mas balls"** (=nodular enlargement non-enhancing scala media)
Grade 2	Displacement of RM, cochlear duct > scala vestibuli	Scala media is scalloping into the scala tympani, PLS has a semicircular appearance			**"X-mas tree"** with **"X-mas balls"**, where ELS is bulding into scala tympani whilst giving the PLS a semicircular appearance (cp. **Figure 1C**).	
Grade 3		A severely distended scala media causes a flattened appearance of the perilymph space	No scala vestibuli visible		**"X-mas tree"** with **"X-mas garlands"**, where ELS is distended and causes a flattened appearance of the PLS (cp. **Figure 1D**).	**"X-mas tree"** (=enhancing scala vestibuli and scala tympani) with **"X-mas garlands"** (=linear enlarged non-enhancing scala media)
VESTIBULUM						
Slice of evaluation	*Lowest slice of vestibulum L-SCC still visible*	*Same as Nakashima et al. (19)*	*Midmodiolar level*	*Axial slice through inferior part of vestibulum*	*Vestibulum inferior part; L-SCC still visible*	*Vestibulum inferior part*
Grade 0	AR <33.3%		AR <50%, sacculus and utriculus are distinguishable	SURI <1, no saccular abnormality	Sacculus < utriculus, otoliths still distinguishable (cp. **Figure 1A**).	AR <50%,sacculus < utriculus, otoliths are distinguishable
Grade 1	33.3%< AR <50%			SURI ≥1	Sacculus (sign should remain as is) utriculus, otoliths are still distinguishable (cp. **Figure 1B**).	Sacculus ≥ utriculus, otoliths are distinguishable
Grade 2	AR >50%		AR >50%, PLS remains visible with circular rim enhancement	No sacculus visible	Sacculus & utriculus are confluent, PLS rim visible (cp. **Figure 1C**).	Sacculus and utriculus are confluent, PLS remains visible with circular rim enhancement
Grade 3			No PLS visible		No otolith organs distinguishable, no PLS visible (cp. **Figure 1D**).	No PLS visible

AR, area ratio; ELS, endolymphatic space; L-SCC, lateral semicircular canal; PLS, perilymphatic space; SURI, ratio ≥ 1 between the area of the sacculus and the area of the utriculus, RM, Reissner's membrane. The bold text highlights the main or most important characteristics.

Nomenclature

In the following, "ipsilateral" refers to the clinically leading side (or affected side) and "contralateral" to the opposite side (or non-affected side). In the case of patients presenting without a leading clinical side, a pseudorandom number generator ["Mersenne Twister" algorithm (37), uniform distribution] was used to generate a random number between 1 (=minimum value) and 9 (=maximum value). Even numbers meant "left side = ipsilateral side" and uneven numbers indicated "right = ipsilateral side." "Vegetative symptoms" refers to nausea and/or vomiting due to the episodic vertigo attack. "Ear symptoms" includes attack-associated tinnitus, hearing loss, ear pressure, and/or ear pain both uni- and bilaterally that fit the criteria for MD. "Other ear symptoms" refers to non-MD ear symptoms.

Measurement of the Auditory, Semicircular Canal, and Otolith Functions

Diagnostic workup included a thorough neurological workup (e.g., history-taking, clinical examination), neuro-orthoptic assessment [e.g., Frenzel glasses, fundus photography, and adjustments of the subjective visual vertical (SVV)], video-oculography (VOG) during caloric stimulation and head impulse test (HIT), as well as ocular (o) and cervical (c) vestibular evoked myogenic potentials (VEMPs) and pure tone audiometry (PTA).

A tilt of the SVV is a sensitive sign of a graviceptive vestibular tone imbalance. SVV was assessed with the subject sitting in an upright position in front of a half-spherical dome with the head fixed on a chin rest (38). A mean deviation of $>2.5^{\circ}$ from the true vertical was considered a pathological tilt of SVV.

The impairment of the vestibulo-ocular reflex (VOR) in higher frequencies was measured by HIT (39) using high-frame-rate VOG with EyeSeeCam [(40), EyeSeeTech, Munich, Germany]. A median gain during head impulses <0.6 (eye velocity in $^{\circ}$/s divided by head velocity in $^{\circ}$/s) was considered a pathological VOR (41). Furthermore, canal responsiveness in lower frequencies was assessed by caloric testing with VOG, which was performed for both ears with 30°C cold and 44°C warm water. Vestibular paresis was defined as >25% asymmetry between the right- and left-sided responses (42). The caloric asymmetry index (AI_C) was calculated based on the slow-phase velocity of the caloric nystagmus: $AI_C\,[\%] = \frac{(R_{33^{\circ}C}+R_{44^{\circ}C})-(L_{33^{\circ}C}+L_{44^{\circ}C})}{(R_{33^{\circ}C}+R_{44^{\circ}C})+(L_{33^{\circ}C}+L_{44^{\circ}C})} \times 100$.

Vestibular evoked myogenic potentials (VEMPs) are short-latency, mainly otolith-driven vestibular reflexes elicited by air-conducted sound (ACS), or bone-conducted vibration (BCV) and recorded from the inferior oblique eye muscle (ocular or oVEMPs) or the sternocleidomastoid muscle (cervical or cVEMPs). VEMPs were recorded with the Eclipse platform (Interacoustics, Middelfart, Denmark), as described previously (43, 44). Only those VEMP responses that were clearly discernible from background noise were included in the analysis. To avoid bias due to examiners, only the asymmetry index ($AI_{o/cV}$) of VEMP amplitudes and latencies was analyzed in detail (45).

Delayed Intravenous Gadolinium-Enhanced MRI of the Inner Ear

Data Acquisition

Four hours after intravenous injection of a standard dose (0.1–0.2 mmol/kg body weight, i.e., 0.1 −0.1 mmol/kg body weight) of Gadobutrol (Gadovist®, Bayer, Leverkusen, Germany), MR imaging (MRI) data were acquired in a whole-body 3 Tesla MRI scanner (Magnetom Skyra, Siemens Healthcare, Erlangen, Germany) with a 20-channel head coil. We used a 3D-FLAIR sequence to differentiate endolymph from perilymph and bone, and a CISS sequence to delineate the total inner ear fluid space from the surrounding bone. The T2-weighted, three-dimensional, fluid-attenuated inversion recovery sequence (3D-FLAIR) had the following parameters: TR 6,000 ms, TE 134 ms, TI 2,240 ms, FA 180°, FOV 160 × 160 mm^2, 36 slices, base resolution 320, averages 1, acceleration factor of 2 using a parallel imaging technique with a generalized auto-calibrating partially parallel acquisition (GRAPPA) algorithm, slice thickness 0.5 mm, acquisition time 15:08 min. The high-resolution, strongly T2-weighted, 3D constructive interference steady state (CISS) sequence of the temporal bones was performed to evaluate the anatomy of the whole-fluid-filled labyrinthine spaces and had the following parameters: TR 1,000 ms, TE 133 ms, FA 100°, FOV 192 × 192 mm^2, 56 slices, base resolution 384, averages 4, acceleration factor of 2 using GRAPPA algorithm, slice thickness of 0.5 mm and acquisition time 8:36 min. The presence of ELH was observed on the 3D-FLAIR images as enlarged negative-signal spaces inside the labyrinth, according to a previously reported method (18, 46).

Signal Quality Assessment

Signal quality was validated using signal-to-noise ratio (SNR) and signal-homogeneity (SH) in different regions of interest (ROIs). ROIs were labeled in the left and right inner ear within the "endolymph" and "perilymph" fluid, "cochlear basal turn," as well as in the surrounding tissue or subject matter, such as the "petrous bone," "cerebellum," "medulla," and "air."

In detail, the endolymph ROI consisted of 0.6 mm^2 circular 2D-selections of the left/right utricle. The perilymph ROIs consisted of multiple 0.6 mm^2 circular 2-D selections in the perilymphatic space (PLS) on both sides and were spread within the inner ear to obtain a signal intensity map. Said selections were placed in the vestibulum, twice inside the basal cochlea turn, the apex cochleae, the horizontal semicircular canal (hSCC) as well as the posterior SCC (pSCC). ROIs in the surrounding tissue or subject matter ("petrous bone," "cerebellum," "medulla oblongata," and "air") consisted of 60.8 mm^2 circular selections. Signal intensity extraction (mean, minimum, and maximum) was performed on axial slices of the FLAIR raw images via the "Analyze Regions" plugin of the "MorphoLibJ toolbox" (47) within ImageJ (48).

SNR was calculated in each ROI as $SNR\,(ROI) = \frac{S(ROI)}{std(air)}$, i.e., the fraction of mean signal intensity in an ROI S(ROI), and the standard deviation (STD) of the region labeled "air," std(air). The label "air" was defined as "MRI signal measure of background variations in the signal devoid of fluid." In other words, a region's SNR was calculated as a mean signal relative to the extent of the background variation.

The signal's statistical homogeneity was examined between ROIs for each group, and between groups for each ROI. SH was defined as the identical distribution of two samples except for shifts and scaling of the overall distribution. The median of each sample was removed and the interquartile range was scaled to the value of one. The two samples were then compared using *the minimum statistical energy* [*minEn*; (49)] and *the maximum mean discrepancy* [*MMD*; (50)], whilst adding 10,000 permutations with a threshold of maximally one failed test to reach statistical significance. Consequently, two samples were deemed to have different distributions if they diverged in shape, either due to kurtosis, skewness or the extent, and number of outliers. Note

that no correction for multiple testing was applied in these tests in order to be more sensitive toward violations of SH, i.e., significant differences.

Semi-quantitative Grading of the Endolymphatic Space

Semi-quantitative (SQ) grading of the endolymphatic space (ELS) was performed independently by three experienced head and neck radiologists or neurologists (BE-W, VK, and JG) who were blinded to the clinical patient data. Rater statistical homogeneity was calculated just as the signal's statistical homogeneity. The ELS's characterization in the vestibulum and cochlea was based on criteria previously described (22) and can be viewed in **Table 1** and is described in further detail in **Figures 1A,B**, grade 0–3.

The characterization describes a 4-point grading for the cochlear and vestibular ELH. The cochlear grading is done on the midmodiolar level (19) and the vestibular grading on the inferior

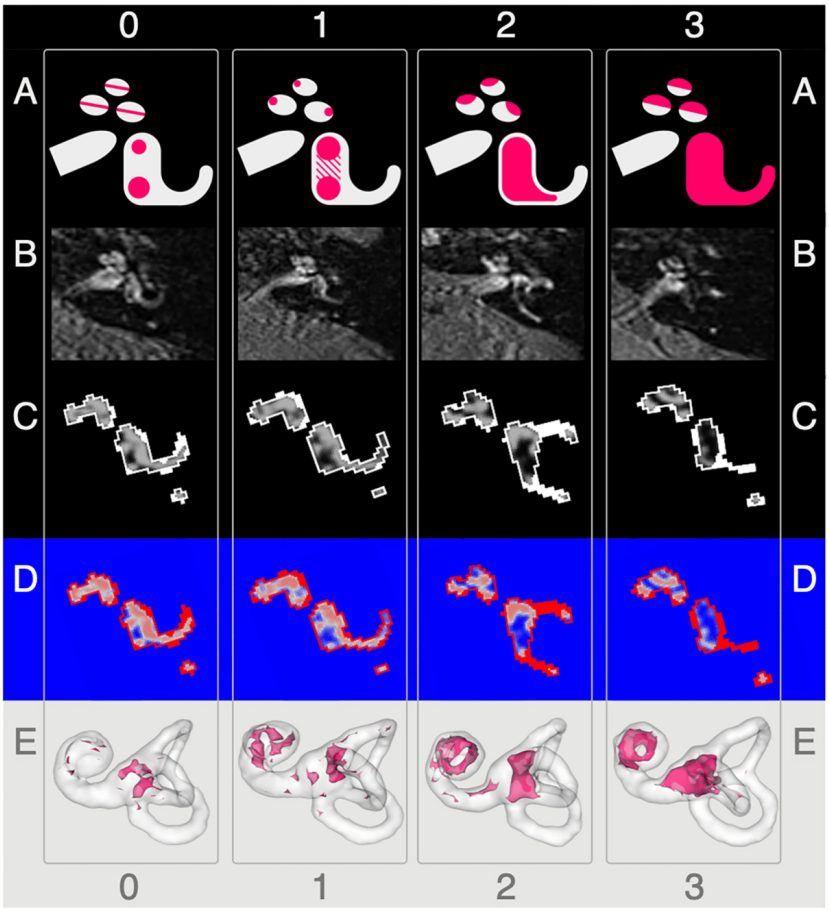

FIGURE 1 | Semi-quantitative (SQ) grading used for the endolymphatic hydrops. The vertical columns show the different semi-quantitative (SQ) grades from 0 to 3 used [cf. **Table 1**; according to a classification first described in Kirsch et al. (9)]. The horizontal rows each give an overview of how each grade looks **(A)**, in FLAIR raw data **(B)**, after VOLT processing **(C)**, as used for 2D quantification **(D)**, and as used for 3D quantification **(E)**. A detailed description of each grade is given in the second paragraph of subsection 'Semi-quantitative Grading of the Endolymphatic Space'.

part of the vestibulum, where the left semicircular canal (L-SCC) is still visible (19). The cochlear grading can be thought of as a fusion of previously described grading suggestions (21–24). Grade 0 (*no vestibular ELH*) can be reduced to "X-mas tree built from circles that are divided by "very thin, clear, hypointense lines" [cp. also Figure 1 of (23), Figure 1A in (21)] that represent the non-enhanced ELS (scala media) between the enhanced PLS (scala vestibuli and tympani). Grade 1 *(mild cochlear ELH)* can be reduced to "X-mas tree with lights," where the ELS is slightly enlarged and indirectly visible as a nodular black cut out of the scala vestibuli [cp. further Figure 2 in (24), Figure 1B in (21)]. Grade 2 (*marked cochlear ELH*) can be reduced to "X-mas tree with X-mas balls," where the ELS is bulging into the scala tympani whilst giving the PLS a semicircular appearance [cp. Figure 3 in (24)]. Grade 3 (*severe cochlear ELH*) can be reduced to "X-mas tree with garlands," where the severely distended ELS is causes a flattened appearance of the PLS [cp. also Figure 4 in (24), Figure 5A in (21), Figure 1C in (20)]. The vestibular grading is a fusion of previously described grading suggestions (21–23). Grade 0 (*no vestibular ELH*) can be reduced to "sacculus<utriculus," where the otolith organs are distinguishable and the sacculus is smaller than the utriculus [cp. also Figure 2A in (21), Figure 6 in (23)]. Grade 1 (*mild vestibular ELH*) can be reduced to "sacculus≥utriculus," where the sacculus is as large or larger than the utriculus [cp. also Figure 2B in (21), Figure 9 in (23)]. Grade 2 (*marked vestibular ELH*) can be reduced to "sacculus and utriculus are confluent," where the otoliths organs are no longer distinguishable with a surrounding PLS rim [cp. also Figure 2C in (21), Figure 7 in (23)]. Grade 3 (*severe vestibular ELH*) can be reduced to "otolith organs not distinguishable" with no PLS visible [cp. also Figure 2D in (21), Figure 8 in (23)].

2D- and 3D-Quantification of the Endolymphatic Space

Segmentation of the total fluid space (TFS) was based on a recently proposed (Ahmadi et al., under review) and pre-trained volumetric deep convolutional neural network (CNN) with V-net architecture (51) that was deployed via the TOMAAT module (52) in 3D–Slicer toolbox [version 4.11 (53)]. ELS and PLS were differentiated within the TFS using Volumetric Local Thresholding [VOLT; (31)] using ImageJ Fiji (48) with the "Fuzzy and artificial neural networks image processing toolbox" (54) and the "MorphoLibJ Toolbox" (47).

The resulting 3D volume can be regarded as a probabilistic map of the inner ear, which includes the classification into its two different compartments (ELS and PLS). The final classification strongly depends on the chosen cutoff. Based on empirical observations (31), 2D- and 3D-quantifications were examined at three cutoff variations (c6, c8, and c10). Each cutoff matches a percentage of positive classifications. For example, cutoff 6 (c6) corresponds to 79.2%, cutoff 8 (c8) to 70.8%, and cutoff 10 (c10) to 62.5% classifications into endolymphatic space. Examples of the pipeline outputs can be viewed in **Figure 1C**.

2D-quantification was done on axial slices of the VOLT volume. The mid-modiolar level was chosen for the cochlea and the inferior part of the vestibulum where the lateral semicircular canal (L-SCC) is still visible was selected for the vestibulum. However, the majority of volumes allowed for both a cochlear and vestibular measurement on the same slice. Easier visual selection was enabled by a look-up-table (LUT, "phase") included in ImageJ that was applied to the VOLT volumes. An example can be seen in **Figure 1D**. Areas were then measured using the "Analyze Regions" plugin which is part of the "MorpholibJ Toolbox" (47).

3D-quantification was done on the VOLT volume that included the entire inner ear. The cochlear volume was cropped using a cylindrical volumetric selection and applied to the VOLT volumes. The volume of the vestibulum including otolith organs and semicircular canals arose from subtracting the cochlear volume from the inner ear VOLT volume. Measurements were performed using the "Analyze Regions (3D)" plugin of the "MorpholibJ Toolbox" (47). A visualization can be seen in **Figure 1E**.

Parameters Derived From Endolymphatic Space Measures

The ELS ratio, $ER\ [\%] = \frac{ELS}{TFS} \times 100$, was calculated for 2D- and 3D-quantification of the ELS analogous to the area ratio (AR) in previous classification conventions (19–21). ER indicates the relative size of the ELH to the TFS and as such is independent of the absolute size which might differ between subjects (for example due to body size).

ELS symmetry between both inner ears was assessed via the ratio of ELS side differences $Diff - ER\ [\%] = ERi - ERc$, where *ERi* and *ERc*are the respective ipsilateral and contralateral ELS ratios in percent relative to the TFS. Another parameter was the asymmetry index, $AI\ [\%] = \frac{(ELSi\ ELSc)}{(ELSi + ELSc)} \times 100$, where ELS_i is the semi-, 2D- or 3D-quantification of the ipsilateral ELS and ELS_c of the contralateral ELS. The asymmetry index can be interpreted as a normalized difference and as such is also independent of the individual TFS.

Areas and volumes were normalized according to their TFS, if ${}_{c/v/a}TFS^{c8}_{e2D/3D} > {}_{c/v/a}TFS^{c8}_{mean\ 2D/3D} + 2.5 \times std\ (TFS)$, where "*e*" is the individual value and "*mean*" is the mean of the respective group (HC or MD). For an overview of TFS, see **Figure 6**.

Statistics and Validation Parameters

All statistics were implemented with self-written scripts in MATLAB version 7.19.0 (R2019b) using the "Statistics and Machine Learning" toolbox provided with MATLAB (Natick, Massachusetts: the MathWorks Inc.). ELS quantification measures were validated and compared using parameters describing different characteristics on different levels (i.e., between groups, ELS analysis methods, and diagnostic methods) and between different entities (i.e., inter-rater, inter-threshold, and inter-ROI). Parameters considered the ordering of subjects between samples (concordance), Spearman correlations between samples (rank-correlation), the form of the distribution of samples via "*minimum statistical energy*" and "*maximum mean discrepancy*" (statistical homogeneity), and covariance between samples via ANCOVA (analysis of covariance). All statistical tests used multiple comparison correction, if multiple tests (e.g., more than two regions or two thresholds) were compared

independently with each other. The FWE level was set at $p = 0.05/N$ with N being the number of tests (e.g., regions, thresholds), i.e., Bonferroni correction.

Influence of Gd Dosage, Gd Time Delay on SNR and via SNR on SQ Grading, 2D- or 3D-Quantitatification

The influence of Gd dosage and time delay (from Gd injection to MR measurement) on the SNR and signal intensity (SI), as well as SNR, Gd dosage and time delay on SQ grading, 2D- or 3D- quantification measures was evaluated using ANCOVA modeling. The model included interaction of the group with each individual variable as well as the interaction of group, dosage and time delay variables. Additionally, covariates of no interest, such as age and BMI, were included. In other words, we checked whether SNR, Gd dosage, and Gd time delay each had an influence on the ELH measure in question, as well as the interaction of Gd dosage and Gd time delay, allowing for the possibility that the relationship might be different for each group.

Interrelations Between SQ Gradings and 2D- or 3D Quantification

Statistical Homogeneity

Statistical homogeneity between SQ grading, and 2D- or 3D- quantification methods between groups was, in principle, calculated in the same way as the signal statistical homogeneity (cf. signal quality validation). First, the median of each group was removed and the interquartile range was scaled to the value of one. The two groups were then compared using *minEn* and *MMD test statistics* whilst using 10,000 permutations between groups. Any instance of a random permutation with a higher test-statistic than the unpermuted groups was considered a failure. The groups were deemed statistically homogeneous if at most one test failed, otherwise the groups were deemed inhomogeneous, as they could be distinguished based solely on their distribution shape (kurtosis and skewness or the extent and number of outliers). Note that no correction for multiple comparisons was performed here in order to be more sensitive to violations of SH, i.e., significant differences.

Rater Repeatability and Reliability

Repeatability and reliability of the three different raters for SQ grading, as well as of the three different thresholds (c6, c8, and c10) for 2D- or 3D-quantification were measured using rank-based correlations and Kendall's W measure for concordance (55). This assessment shows whether the ordering of subjects between raters is similar and therefore can be assumed to be repeatable over the raters. Furthermore, we compared ratings by subtracting the SQ grading scores between raters to see if the extent of differences in rating values differed. Correction for multiple comparisons, i.e., multiple tests was done over data types (SQ, 2D and 3D), therefore $p_{(\mathrm{FWE})} = 0.05$ was set to $p = 0.05/N$ with $N = 3$ for the three data types.

Interrelations Between SQ Grading, 2D- and 3D-Quantification

Interrelations between SQ grading, 2D- and 3D-quantification were examined via Spearman, i.e., rank-based correlations. Significant rank correlations indicated that the ordering of subjects was very similar or concordant across these measures. Rank-correlation was used so that linear as well as non-linear relationships could be examined and the gradings (ordinal measures) could be related to the quantitative measures. Correction for multiple comparisons $p_{(\mathrm{FWE})} = 0.05/N$, i.e., Bonferroni correction, was done over all pairs of correlations in each correlation matrix, i.e., for SQ-×-2D quantification and SQ-×-3D quantification $N = 12\text{-}\times 12 = 144$ and for the correlation of asymmetry indices $N = 6\text{-}\times 6 = 36$.

Influence of Thresholds on Quantitative Measures

The influence of VOLT thresholds (c6, c8, and c10) on group differences was assessed using general linear model (GLM) based two-sample *t*-tests (including age as a covariate of no interest). The resulting slopes for the effects of thresholds and their standard errors were used to calculate *t*-statistic values for each group comparison at each threshold. Furthermore, a slope difference test (56) was used to check if group differences depended on the VOLT thresholds. A slope difference test compares differences in slopes with standard errors for the group differences across thresholds to determine if group differences depended on the cutoff-threshold. Correction for multiple comparisons $p_{(\mathrm{FWE})} = 0.05/N$, i.e., Bonferroni correction, was done for three tests of between threshold comparisons resulting from three thresholds (c6,c8,c10), i.e., c6-vs-c8, c6-vs-c10, and c8-vs-c10, and therefore $N = 3$.

Covariance of Clinical Measures and iMRI

Clinical (e.g., disease duration, number of attacks) and diagnostic measures (e.g., HIT, calorics, and VEMPs), as well as parameters derived from ELS measures in SQ gradings and 2D- and 3-D quantifications (*ER*, *Diff-ER*, and *AI*) were included in an analysis of covariance (ANCOVA). An overview of clinical symptoms and diagnostic measures can be viewed in **Table 2**. Furthermore, the analysis accounted for categorical variables, such as symptoms like headache, and continuous covariates, such as body mass index (BMI) and the age of the patients. For detection of diverging trends between MD or HC, parameters derived from ELS measures were allowed interactions with the group. That means each group was allowed to have a different trend in the model. We used Bonferroni-correction for the *post-hoc* assessment of the individual factors in the ANCOVA.

Influence of ELH Presence on SNR and SI

The influence of the presence and extent of ELH on SNR and SI was examined with two approaches. First, SNR and SI data were investigated using classifications derived from SQ grades and 3D-quantification measures. The SQ grades were used to distinguish between "no ELH" and "ELH present," while the 3D-quantification was used to distinguish between "low/small ELH" and "high/large ELH." For the classification using SQ grades, all grades equal to zero (SQ grade == 0) were allocated to "no ELH" and the rest to "definite ELH present." For the classification using 3D-quantification, data values below the median were in the "low ELH" class and data values above the

TABLE 2 | Clinical syndrome and diagnostic characteristics.

		MD		HC
	All	Definite	Probable	All
	n = 75	*n* = 35	*n* = 40	*n* = 33
Age [in years]	55.2 ± 14.9	54.8 ± 14.1	55.6 ± 15.8	42.1 ± 18.9
Age range	22–81	27–77	22–81	20–84
Gender	36 females	14 females	22 females	19 females
Handedness	97% RH, 3% LH	100% RH	93% RH, 7% LH	97% RH, 3% LH
(A) Clinical syndrome				
Type of vertigo	73% Ro, 25% Sw, 2% Lh	83% Ro, 14% Sw, 3% Lh	64% Ro, 33% Sw, 3% Lh	–
Duration of illness [in months]	56.8 ± 88.7	49.0 ± 84.9	63.5 ± 92.4	–
Number of attacks altogether	48.7 ± 56.6	47.2 ± 49.1	49.8 ± 62.7	–
Number of attacks in the last 3 months	15.0 ± 37.8	18.5 ± 52.4	12.4 ± 21.2	–
Duration of attacks [in hours]	5.0 ± 6.9 (0.5–24)	3.2 ± 3.0 (0.5–12)	6.7 ± 8.7 (0.5–24)	–
Time since last attack [in days]	35.1 ± 44.7 (1–180)	36.1 ± 43.4 (1–180)	33.9 ± 47.0 (1–180)	–
Nausea, Vomiting	86.7%	97.1%	77.5%	–
VM-Headache	1.3%	0%	2.5%	–
Sensitivity to light or noise	9.7%	8.6%	10.0%	–
Focal neurological deficits	8.0%	0%	15%	–
History of migraine	1.7%	3.1%	0%	–
Family history of migraine	5.1%	0%	11.5%	–
Other-Headache	22.7%	28.6%	17.5%	–
MD-Ear-symptoms	84.0%	94.3%	75.0%	–
MD-bilateral	25.3%	31.4%	20.0%	–
MD-ipsilateral	81.3%	94.3%	70.0%	–
MD-contralateral	8.0%	11.4%	5.0%	–
Other-Ear-symptoms	8.0%	2.9%	12.5%	–
Other-bilateral	8.0%	2.9%	12.5%	–
Other-ipsilateral	9.3%	0%	15%	–
Other-contralateral	0%	0%	0%	–
(B) Diagnostic characteristics				
CEMD	9.3%	2.9%	15%	0%
PEMD ipsilateral	53.3%	60.0%	47.5%	0%
SVV ipsilateral, pathologic	28%	34.3%	22.5%	0%
Caloric ipsilateral, pathologic	83.6%	94.3%	73.7%	0%
Caloric contralateral, pathologic	0%	0%	0%	0%
Caloric bilateral, pathologic	1.4%	0%	2.6%	0%
Caloric ipsilateral [°/s]	7.6 ± 6.9 (0.8–40.6)	7.8 ± 7.8 (0.9–40.3)	7.5 ± 6.1 (0.8–34.4)	13.8 ± 4.5 (3.8–24.2)
Caloric contralateral [°/s]	12.8 ± 8.4 (1.6–55.0)	13.8 ± 9.7 (1.6–55.0)	11.9 ± 7.0 (2.7–32.5)	19 ± 11 (4.8–50.1)
Caloric Asymmetry-Index [%]	34.8 ± 22.7 (0.7–90.6)	36.4 ± 23.3 (0.9–40.6)	33.3 ± 22.2 (0.8–90.6)	0.2 ± 19.8 (0.8–48.3)
HIT ipsilateral, pathologic	48.4%	51.6%	45.5%	0%
HIT bilateral, pathologic	6.3%	6.5%	6.1%	0%
HIT ipsilateral [gain at 60ms]	0.8 ± 0.2 (0.2–1.1)	0.7 ± 0.2 (0.2–1.02)	0.8 ± 0.2 (0.4–1.1)	1 ± 0.1 (0.8–1.1)
HIT contralateral [gain at 60 ms]	0.8 ± 0.2 (0.4–1.1)	0.8 ± 0.2 (0.4–1.01)	0.9 ± 0.1 (0.6–1.09)	0.9 ± 0.1 (0.8–1.0)
Audio MD-typical ipsilateral	76.2%	93.3%	60.6%	0%
Audio MD-atypical ipsilateral	3.2%	0%	6.1%	0%
Audio Presbyacusis-typical	0%	0%	0%	0%
Audio low-frequency ipsilateral [dB]	41.3 ± 23.1 (8.0–110.0)	49.9 ± 20.3 (10.0–110.0)	33.7 ± 22.9 (8.0–92.0)	20.0 ± 3 (8.0–35.0)
Audio low-frequency contralateral [dB]	21.1 ± 14.4 (7.0–77.0)	20.3 ± 11.6 (7.0–63.0)	20.3 ± 11.6 (7.0–63.0)	18 ± 6 (15–33.0)

CEMD, central eye movement disorder; Lh, light-headedness; PEMD, peripheral eye movement disorder; Ro, rotational vertigo; Sw, swaying vertigo.

median in the "high ELH" class. The SNR and SI data were analyzed using two-sample *t*-tests and Wilcoxon rank-sum tests for differences from these classifications. The two tests (i.e., a parametric and non-parametric test), were used to ensure that any of the significant differences found were not purely dependent on the assumed distribution. Correction for multiple comparisons $p_{(\mathrm{FWE})} = 0.05/\mathrm{N}$, i.e., Bonferroni correction, was done for five tests between regions (split by ELH) comparisons, i.e., $N = 5$ (see **Figures 5A,B**).

Then, the inverse question was asked. This time SQ and 3D-quantification values were compared following SI or SNR value classification and then analyzed accordingly for differences with two-sample *t*-tests and Wilcoxon rank-sum tests. For both SI and SNR classification, "*low SI or SNR class*" was defined by their values below the respective median, and "*high SI or SNR class*" by their values above the respective median. Correction for multiple comparisons $p_{(\mathrm{FWE})} = 0.05/\mathrm{N}$, i.e., Bonferroni correction, was done separately for the test between SNR (split by ELH 3D-quantification) and 3D-quantification (split by SI). The number of tests for the SNR comparison was $N = 2$, and the number of tests for ELH 3D-quantification was $N = 4$ (see **Figures 5C,D**).

RESULTS

Descriptive Statistics

Seventy-five MD patients (35 females; aged 22–81 years, mean age 56.6 ± 14.9 years; 97% RH) and 33 HC participants (20 females; aged 20–84 years, mean age 42.1 ± 18.9 years; 94% RH) were included in the study. An overview of the most important clinical features in MD compared to HC can be seen in **Table 2**. An overview of the ELS grading for HC and MD can be viewed in **Table 3**.

Influences of Signal Quality on ELS Quantification Methods (i)

- The signal intensity (SI) of each region of interest significantly (FWE-corrected, $p < 0.05$) depended on Gd dosage (range: 0.08–0.28 ml/kg; mean ± std: 0.17 ± 0.05 ml/kg; 48% of subjects got 1 dose, 12% 1.5 doses; 40% got 2 doses of 0.1 ml/kg) and Gd time delay (range: 2 h and 51 min to 5 h and 20 min; mean ± std: 4 h and 24 ± 25 min; 25% are between 3 and 4 h, 50% are between 4 and 4 h and 31 min and the remaining 25% were longer). However, the effect sizes (eta-squared) were small (5–12%).
- The mean SNR (range: 24.8–130.49; mean ± std: 64.82 ± 20.64) was significantly related to Gd dosage and time delay (FWE-corrected, $p = 0.006$), but only 6.8% of the total variance (*r*-squared) could be explained. If looked at separately, Gd dosage (4.2%, FWE-corrected, $p = 0.03$) and Gd time delay (5.3%, FWE-corrected, $p = 0.02$) explained even less of the variance. See **Figure 2** for an overview of the minor influence of the iMRI acquisition parameters on SNR.
- The mean SNR was significantly different between the MD and HC group ($p < 0.05$). SNR asymmetry between left and right ear was not significantly related to Gd dosage, Gd time delay, or Gd dosage × Gd time delay.
- SQ gradings and 2D- or 3D- quantifications were not significantly related to Gd dosage, Gd time delay, Gd dosage × Gd time delay interaction, SI or SNR (FWE corrected, $p \leq 0.05$). There were some simple significant relationships ($p < 0.05$ uncorrected) for the iMRI variables with Gd dosage and SNR, but all these relationships were small in effect size (around 0.5–5% omega squared).

Interrelations Between ELS Quantification Methods (ii)

- Inter-rater SQ gradings (R1-3) were statistically homogeneous, as were 2D- and 3D- quantification values including ipsi- and contralateral or cochlea and vestibulum.
- Inter-rater SQ gradings (R1-3) were highly matched in the vestibular (v) and cochlear (c) part of the inner ear for all subjects (HC, MD) and slightly less for MD only. The results can be viewed in **Table 4** (column SQ) and suggest a high but imperfect reproducibility due to remaining variability.
- Inter-threshold (c6, c8, and c10) 2D- and 3D-quantification was highly concordant. These results can be viewed in **Table 4** (column 2D and 3D) and indicate an almost perfect agreement over VOLT thresholds with a basically perfect reproducibility.
- SQ grades correlated strongly with 2D-quantification values (range of correlation from 0.3 to 0.7) and 3D-quantification values (range of correlation from 0.3 to 0.7). The correlations of 2D- and 3D-quantification values with SQ grades was mainly driven by the MD group, due to the higher variability within the group, compared to HC group which did not vary much in grades or 2D- and 3D-quantification values (cp. **Figure 3**, plots on the left and in the middle).
- 2D- and 3D-quantification correlated substantially (range of correlation from 0.3 to 0.8) for the total inner ear, cochlea, and vestibulum on both the ipsilateral and contralateral side. However, there were no significant correlations of the ipsilateral with the contralateral sides (cp. **Figure 3**, plots on the right). AI_{SQ} (asymmetry-index of SQ quantification) correlated significantly (range of correlation from 0.3 to 0.7) with AI_{2D} and AI_{3D} (asymmetry-indices of 2D- and 3D-quantification) except for the cochlear *AI* in the 2D- and 3D-quantifications in the c6-cutoff (cAI^{c6}_{2D} and cAI^{c6}_{3D}, cp. **Figure 3**).
- Inter-rater SQ grading differences did not differ strongly between R1-3. **Figure 4** shows the results in more detail. For the vestibular part, the percentage of ratings that agreed, i.e., showed zero differences, was 54.6% (R2-R1), 50% (R3-R1), and 67.6% (R3-R2), while the percentage of differences of maximally one grade apart was 85.2% (R2-R1), 90.7% (R3-R1), and 98.2% (R3-R2). For the cochlear part, the percentage of ratings that agreed was 53.7% (R2-R1), 53.7% (R3-R1), and 71.3% (R3-R2), while the percentage of differences of maximally one grade apart was 88.9% (R2-R1), 90.7% (R3-R1), and 97.2% (R3-R2).
- Inter-threshold 2D- and 3D-quantification measures were statistically homogenous and showed group differences for each threshold.
- Clinical variables correlated with symmetry parameters derived from SQ grading and 2D- or 3D-quantification values such as the asymmetry index (*AI*) or the plain ELH

TABLE 3 | Semi-quantitative (SQ) grading, 2D- and 3D-quantification of the ELS.

			All (n = 75)				MD Definite (n = 35)				Probable (n = 40)				HC All (n = 33)			
(A) EH presence [%]			**R1**	**R2**	**R3**	**R1-3**	**R1**	**R2**	**R3**	**R1-3**	**R1**	**R2**	**R3**	**R1-3**	**R1**	**R2**	**R3**	**R1-3**
Ipsilateral	ELS		80%	69%	85%	78%	86%	83%	91%	87%	75%	57%	80%	71%	9%	39%	27%	25%
	cELS		65%	60%	67%	64%	74%	74%	74%	74%	57%	48%	60%	55%	6%	21%	9%	12%
	vELS		72%	61%	69%	68%	74%	74%	80%	76%	70%	50%	60%	60%	9%	33%	27%	23%
Contralateral	ELS		73%	44%	72%	63%	77%	37%	77%	64%	70%	50%	68%	63%	21%	27%	27%	25%
	cELS		59%	32%	40%	44%	57%	23%	37%	39%	60%	40%	43%	48%	15%	21%	9%	15%
	vELS		61%	36%	56%	51%	63%	34%	71%	56%	60%	38%	43%	47%	21%	24%	24%	23%
(B) SQ grading																		
Grades			**0**	**1**	**2**	**3**	**0**	**1**	**2**	**3**	**0**	**1**	**2**	**3**	**0**	**1**	**2**	**3**
Ipsilateral	ELS	R1-3	15%	15%	13%	5%	9%	14%	17%	3%	20%	15%	10%	8%	73%	9%	0%	0%
	cELS	R1-3	33%	35%	27%	5%	26%	34%	37%	3%	40%	35%	18%	8%	91%	9%	0%	0%
	vELS	R1-3	31%	31%	24%	15%	20%	26%	40%	14%	40%	35%	10%	15%	73%	27%	0%	0%
Contralateral	ELS	R1-3	28%	20%	8%	1%	23%	23%	9%	3%	33%	18%	8%	0%	73%	6%	0%	0%
	cELS	R1-3	60%	28%	11%	1%	63%	23%	11%	3%	57%	33%	10%	0%	91%	9%	0%	0%
	vELS	R1-3	44%	39%	15%	3%	29%	51%	17%	3%	57%	28%	13%	3%	76%	24%	0%	0%
Percentage		R1-3	**Min**	**25%**	**50%**	**75%**	**Min**	**25%**	**50%**	**75%**	**Min**	**25%**	**50%**	**75%**	**Min**	**25%**	**50%**	**75%**
AI [%]	ELS	R1-3	0	0	33	100	0	20	33	92	0	0	43	100	0	0	0	100
	cELS	R1-3	0	0	50	100	0	0	100	100	0	0	33	100	0	0	0	100
	vELS	R1-3	0	0	33	100	0	0	33	88	0	0	27	100	0	0	0	100
(C) 2D-quantification																		
			Mean	**Std**	**25%**	**50%**	**75%**	**Mean**	**Std**	**25%**	**50%**	**75%**	**Mean**	**Std**	**25%**	**50%**	**75%**	**Mean**	**Std**	**25%**	**50%**	**75%**
Ipsilateral	ELS	c8	5.5	2.7	3.4	5.2	7.4	6.3	2.8	4.5	6.2	8.5	4.7	2.4	3.1	4.4	6.5	3.4	1.3	2.5	3.3	4
[mm^2]	cELS	c8	1.4	0.9	0.8	1.2	1.9	1.6	0.9	0.9	1.4	2.3	1.2	0.9	0.5	1.2	1.5	1	0.5	0.7	1.1	1.3
	vELS	c8	4.1	2.2	2.6	3.6	5.8	4.7	2.4	3.3	4.9	6.2	3.5	1.9	2.3	3.2	4.8	2.4	1.1	1.7	2.3	2.9
Contralateral	ELS	c8	3.7	1.8	2.6	3.3	4.5	3.9	1.9	2.7	3.5	4.8	3.5	1.7	2.6	3.3	4	3.6	1.2	2.7	3.8	4.5
[mm^2]	cELS	c8	1	0.6	0.6	0.8	1.3	1.1	0.7	0.4	1	1.8	0.9	0.5	0.6	0.8	1.2	1.1	0.7	0.7	1	1.4
	vELS	c8	2.6	1.5	1.8	2.2	3.3	2.8	1.5	2	2.4	3.6	2.5	1.6	1.7	2.1	2.7	2.5	0.9	1.8	2.4	3.1
AI [%]	ELS	c8	16.1	28.2	0.2	14.8	34.6	20.7	27.2	5.1	22.7	45.8	12.1	28.7	0.7	14.7	31.1	4.0	20.4	17.3	7.02	12.7
	cELS	c8	13.2	40.4	5.6	17.9	34.2	17.3	41.4	5	14.3	46.1	9.6	39.8	6.6	18.8	33.3	2.5	32.5	27.0	0	22.9
	vELS	c8	17.9	33.8	0.9	21.4	38.6	20.5	34.8	0.9	28.6	45.7	15.7	33.2	0.6	21.4	30.0	3.2	24.6	16.5	1.5	9.5
ER [%]	ELS	c8	14.71	6.97	10.09	13.7	20.44	16.61	6.85	11.14	16.67	21.52	13.05	6.73	7.24	11.99	17.54	9.33	3.22	7.18	8.66	11.04
Ipsilateral	cELS	c8	8.4	5.1	4.8	7.9	11.6	9.4	5.1	5.5	8.6	13.2	7.6	5	3.3	7.3	9.7	6.3	2.8	4.5	6.3	7.9
	vELS	c8	19.7	10.3	11.9	19.2	27.7	22.3	10.7	13.8	23.1	30.3	17.4	9.5	11.1	16.1	23.8	11.7	4.8	8.8	10.7	15.1
ER [%]	ELS	c8	9.7	4.1	7.3	8.9	11.6	10.4	4.5	7.3	9.6	13	9.1	3.7	7.3	8.8	9.9	9.9	2.7	7.6	10.3	12.4

(Continued)

TABLE 3 | Continued

			All					MD				Definite				Probable				HC			
			(*n* = 75)					(*n* = 35)				(*n* = 40)				(*n* = 33)							
Contralateral	cELS	c8	6.2	3.7	3.4	5.3	8.3	6.8	4.2	2.7	6.3	10.8	5.7	3.1	3.8	5.1	7.4	7	4.1	4.6	6.3	8.2
	vELS	c8	12.3	6.4	9.1	10.5	14.2	13.4	6.7	9.2	12	17.4	11.4	6.1	8.2	9.9	13	12.1	3.9	9.3	11.7	14.9
ER [%]-	ELS	c8	5	7.4	0.3	3.2	9.9	6.2	8	−0.5	6.3	12.3	3.9	6.6	0.3	3.2	6.5	−0.6	3.7	−3	−0.7	2.3
Difference	cELS	c8	2.3	6.2	−0.4	2.1	6.5	2.7	6.8	−0.4	2.5	6.7	1.9	5.8	−0.7	2.1	5.1	−0.7	4.6	−2.6	0	1.9
	vELS	c8	7.3	10.8	0.2	6.2	12	8.9	12.5	1.1	9.9	18	6	9.1	0	6.2	9.8	−0.5	5.4	−4	−0.4	2.4
TFS	ELS	c8	36.9	3.8	34.5	36.6	39.3	37.2	3.6	35.3	37.1	39.6	36.6	3.9	34	36.5	38.5	36.2	3.7	34.1	37.1	39
Ipsilateral	cELS	c8	16.3	1.7	15.5	16.4	17.4	16.5	1.6	15.3	16.6	17.6	16.3	1.8	15.6	16.4	17.3	15.8	1.8	14.9	15.9	16.8
[mm^2]	vELS	c8	20.5	2.6	18.8	20.1	22.4	20.8	2.6	19.3	21.1	22.4	20.3	2.6	18.4	19.8	22.5	20.5	2.5	18.8	20.9	21.9
TFS	ELS	c8	37.3	3.9	35.3	37.1	39.4	37.1	3.5	35	36.6	39.4	37.5	4.2	35.3	37.1	39.4	36.6	3.3	34.2	37.1	37.9
Contralateral	cELS	c8	16.2	1.8	15.2	16.1	17.3	16.3	1.4	15.3	16.2	17.1	16.2	2.1	15.1	15.9	17.8	16.1	1.6	14.9	15.8	17.2
[mm^2]	vELS	c8	21.1	2.7	19.5	20.8	22.7	20.8	2.5	18.5	20.7	22.3	21.3	2.8	19.6	20.8	22.8	20.4	2.2	18.7	20.4	22.3
(D) 3D-quantification																						
			Mean	**Std**	**25%**	**50%**	**75%**	**Mean**	**Std**	**25%**	**50%**	**75%**	**Mean**	**Std**	**25%**	**50%**	**75%**	**Mean**	**Std**	**25%**	**50%**	**75%**
Ipsilateral	ELS	c8	23.5	8.4	17.7	20.9	30.1	26	9	17.8	26.9	32.1	21.2	7.2	16.9	19.8	23.4	16.1	5.6	12.1	15.4	18.5
[mm^3]	cELS	c8	6.8	3.5	4.4	5.4	9	7.8	3.6	4.8	7.2	10.7	5.9	3.1	4.4	4.9	6.9	5	2.4	3.5	4.6	6
	vELS	c8	16.6	6.1	12.4	15.3	20.5	18.2	7	13	19.3	22.2	15.3	4.9	12.2	14.8	17.2	11.1	3.6	9	11.6	12.9
Contralateral	ELS	c8	17.2	4.6	14.4	16.3	20	17.4	4.5	14.9	17.4	20	17.1	4.7	14.4	16.2	19.9	16.2	3.9	13.2	16.5	19.2
[mm^3]	cELS	c8	5	2	3.7	4.6	6.4	5.3	2.3	3.7	4.8	6.5	4.8	1.8	3.6	4.6	6	5	2	3.2	4.7	6.1
	vELS	c8	12.2	3.8	9.8	11.4	14.3	12.2	3.2	10	12.8	14.2	12.3	4.4	9.6	11.4	14.4	11.2	3	8.8	11.7	13.1
AI [%]	ELS	c8	13.4	16.1	1.1	10	22.8	17.5	17.0	2.9	17.5	32.0	9.7	14.5	0.3	10	18.8	1.9	15.9	12.3	0.6	5.9
	cELS	c8	11.9	25.8	5.4	7.94	29.4	17.6	27.1	3.1	20.8	31.7	6.9	23.9	10.6	2.5	26.6	0.8	23.9	15.1	6.8	13.1
	vELS	c8	13.5	16.9	1.1	12.7	25.9	16.4	18.3	0.52	18.4	32.9	10.7	15.3	1.5	9.1	14.7	1.6	17.12	12.0	3.8	7.4
ER [%]	ELS	c8	8.5	2.8	6.4	7.5	10.8	9.3	2.9	7	9.6	11.9	7.7	2.5	6	7.3	8.9	5.9	1.6	4.8	5.9	6.5
Ipsilateral	cELS	c8	7	3.3	4.7	6	9.8	8	3.3	5.2	7.4	11	6.2	3	4.6	5.2	6.5	5.5	2.2	4	5.1	6.6
	vELS	c8	9.2	3.1	7	8.8	11.3	10	3.4	8.4	10.6	12.7	8.5	2.7	6.2	8.1	10.2	6.2	1.7	5.4	6.2	7
ER [%]	ELS	c8	6.2	1.3	5.4	6.1	6.9	6.2	1.3	5.6	6.4	7.2	6.1	1.3	5.3	6	6.7	6	1.2	4.8	6	6.8
Contralateral	cELS	c8	5.3	1.9	4	5.1	6.2	5.4	2	4	5	6.7	5.2	1.9	4	5.1	5.7	5.4	2.1	3.9	5	7
	vELS	c8	6.7	1.8	5.4	6.3	7.8	6.7	1.7	5.3	7.2	7.9	6.6	1.9	5.6	6.2	7.2	6.2	1.4	5.4	6.5	7
ER [%]-	ELS	c8	2.3	2.8	0.2	1.3	4	3.1	2.9	0.7	2.5	6.1	1.6	2.4	−0.1	1.3	2.7	0	1.7	−1	0	0.8
Difference	cELS	c8	1.8	3.5	−0.6	1	3.8	2.6	3.6	−0.5	2.4	5	1	3.3	−0.6	0.1	2.1	0.1	2.4	−1.4	0	1.6
	vELS	c8	2.5	3	0	1.9	4.7	3.3	3.3	0.3	3.2	6.3	1.9	2.6	−0.1	1.6	2.9	−0.1	1.9	−1.3	−0.5	0.9
TFS	ELS	c8	275.7	29.2	258	271.4	295	276.9	26.8	259.2	275	296.4	274.8	31.5	252.8	271.4	295	267.4	37.2	251	271.1	291
Ipsilateral	cELS	c8	95.2	12.2	86.7	93.4	103	96.7	12.3	87.5	96.7	105.4	93.9	12.2	85.8	93.4	102	88.6	14.4	80.5	88.2	98.4
[mm^3]	vELS	c8	179.9	20.1	166	182	192	178.6	17.6	166.5	176.3	192.7	181	22.2	165.7	182	192	178.7	27.1	166	178.6	195
TFS	ELS	c8	276.5	31.2	257	269.1	298	277.3	30	256.8	275.1	300.9	275.8	32.5	258.6	269.1	298	269.9	25.7	248	270.6	290
Contralateral	cELS	c8	94.8	13.3	86.2	93	103	95.9	13.1	86.7	95	104.2	93.8	13.6	83	90.6	102	91.3	12.5	80.3	89.8	96.3
[mm^3]	vELS	c8	182.4	20.6	171	183.3	193	181.3	19.5	171.5	178.2	192.7	183.4	21.7	171.4	183.4	193	178.6	17.8	168	180.7	190

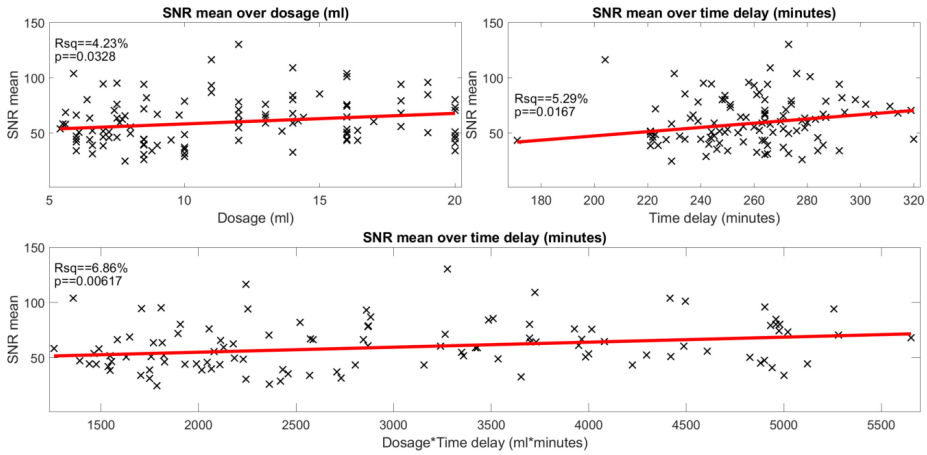

FIGURE 2 | Influence of gadolinium (Gd) dosage and Gd time delay on the signal-to-noise ratio (SNR) (belonging to question i). The scatter plot of the signal-to-noise ratio (SNR) over the gadolinium (Gd) dosage (in ml, plot in the top left), of the SNR over the time delay (in minutes, plot in the top right) and of the SNR over the interaction of Gd dosage×time delay (ml × minutes, plot in the bottom). SNR data points are plotted as black crosses and the trend lines of the fitted model are plotted as red lines. The SNR depended significantly on dosage, time delay as well as the interaction of dosage × time delay. However, the effect size was very small (4.2, 5.3, and 6.8% of explained variance, respectively). The SNR displayed here "SNR mean" is the mean of the SNRs calculated for each region of interest, i.e., the two inside the basal cochlear turn (CBT), the apex cochleae (AC), the horizontal semicircular canal (hSCC) as well as the posterior SCC (pSCC). For each region, the SNR is the mean signal divided by the standard deviation of the region labeled "air." The left and the right ear are averaged for each region, before regions are averaged to form "SNR mean".

TABLE 4 | Interrelations between ELS quantification methods.

	Vestibulum			Cochlea		
	3D	**2D**	**SQ**	**3D**	**2D**	**SQ**
(A) MD + HC						
W	0.99	0.99	0.74	0.99	0.97	0.70
p-Value	6e-180	7e-175	5e-26	1e-180	3e-124	1e-20
F-Value	238.1	213.3	5.7	242.2	69.9	4.7
(B) MD						
W	0.99	0.99	0.71	0.99	0.98	0.62
p-Value	4e-125	7e-129	2e-15	2e-128	2e-103	8e-09
F-Value	238.5	268.5	4.9	264.5	120.3	3.2

W = Kendall's coefficient of concordance between multiple rankings. Its value ranges from 0 to 1, unity being attained for perfect agreement between rankings.

difference between ipsilateral and contralateral side for the inner ear, vestibulum, and cochlea. The *AI* worked for un-normalized data and its results were comparable to the normalized data, while the pure differences between ipsilateral and contralateral sides were only useful when the data was first normalized to the fraction ER [%] of the total fluid space (TFS, cf. legend on standard values). This indicates that relative proportions of both ears, and the relative size of ELH are most useful for predicting quantitative clinical data from iMRI measures. Fittingly, vestibular AI for the 3D-quantification data explained 35% of the variance of the number of attacks in the 3 months prior to the examination and another 16% of variance could be explained by the AI for the 3D-quantification data of the whole of the inner ear (vestibular and cochlear parts combined). A more detailed clinical study and discussion can be found in another work (57).

Influences on Signal Quality (iii)

- There were significant differences in SI due to the presence of ELH in the following ROIs: cochlear basal turn [$p_{(t-\text{test})}$

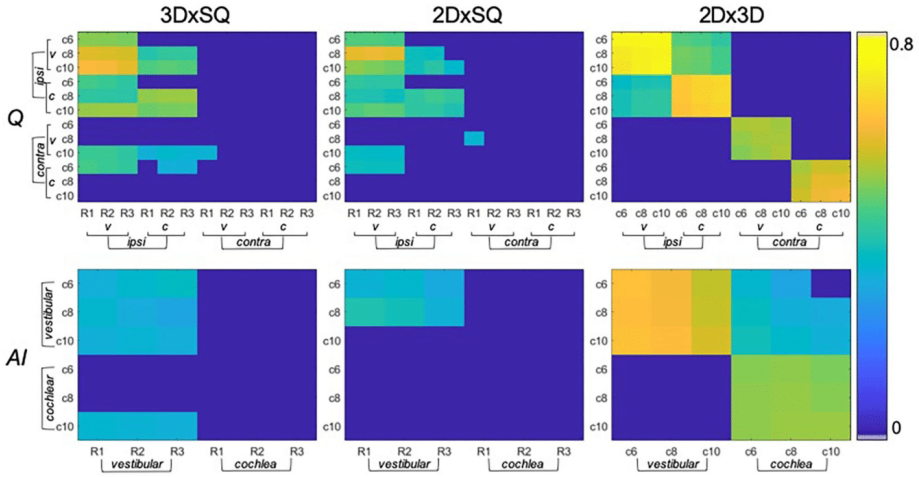

FIGURE 3 | Significant correlations between endolymphatic hydrops (ELH) quantification methods (belonging to question ii). The top row shows the correlations between semi-quantitative (SQ) gradings (x-axis) and 2D- or 3D- quantification values (y-axis) for vestibulum (v) or cochlea (c), and for the ipsilateral (ipsi) or contralateral side (contra). In addition, SQ gradings are rater-specific (R1-R3), and 2D- or 3D- quantification values are cutoff-specific (c6, c8, and c10). The higher the significant results ($p < 0.05$ FWE-corrected) correlated, the more they are colored in yellow (thresholded to 0–0.8). Overall, SQ gradings and 2D- or 3D-quantification values correlated with the respective other method, although to a higher extent on the ipsilateral side (on the contralateral side in c10) and vestibular part of the inner ear. The bottom row shows the corresponding correlations between methods (SQ gradings and 2D- or 3D- quantification values) for the respective asymmetry-index (*AI*).

$= 0.0009$ and $p_{(\text{rank-sum})} = 0.0003$], apex cochleae [$p_{(t\text{-test})} = 0.002$ and $p_{(\text{rank-sum})} = 0.001$], hSCC [$p_{(t\text{-test})} = 0.038$ and $p_{(\text{rank-sum})} = 0.022$], and pSCC [$p_{(\text{t-test})} = 0.046$ and $p_{(\text{rank-sum})} = 0.018$]. Generally, higher ELH 3D-quantification values had higher SI values. However, due to a significant spread, SI could not distinguish the presence of ELH from the absence of ELH (tested by means of the split of SI values based on defining "absence of ELH" as an SQ grading equal to zero and "presence of ELH" as all grades higher than zero). Fittingly, the opposite approach (splitting ELH values by SI brightness) did not show significant differences. For an overview, please see **Figure 5**. The signal intensity SI was significantly different between the MD and HC group for both ROIs in the cochlear basal turn, but not for the cochlear apex, hSCC, or pSCC ($p < 0.05$ FWE). The group differences in iMRI variables between the MD and HC groups persisted after removing effects of Gd dosage, time delay, and SNR, indicating that iMRI assessment was not significantly affected by the differences in Gd dosage, time delay, and SNR in the present dataset.

- SNR was not influenced significantly by the presence or absence of an ELH. Selecting SNR values for all SQ grades = 0 ("absence of ELH") and comparing them with the remaining SNR values (where SQ grades >0, "presence of ELH") led to two-sample t-test $p = 0.99$ and two-sample rank-sum test $p = 0.94$. Furthermore, comparing the SNR values for low ELH values (3D-quantification values below the median) with SNR values for high ELH values (3D-quantification values above the median) did not show any significant differences in SNR (two-sample t-test $p = 0.31$ and two-sample rank-sum test $p = 0.45$). Analog to this, splitting ELH values due to low SNR values vs. high SNR values did not result in significant differences [$p_{(t\text{-test})} = 0.66$ and $p_{(\text{rank-sum})} = 0.47$ on the ipsilateral side and $p_{(\text{t-testtest})} = 0.2$ and $p_{(\text{rank-sum})} = 0.16$ for the contralateral side]. For an overview, see **Figure 5**.

Standard Values

- Areas and volumes were normalized according to their TFS (total fluid space/surface) and can be viewed in **Figure 6**.
- Our calculations showed that the chosen threshold did not change the group differences between MD and HC. The grading-specific 2D- and 3D-quantification values, the TFS values and resulting ratios can be seen in **Figures 6**, **7**. Furthermore, we show the relationship of 2D- and 3D-quantification for the vestibular and cochlear part broken down by SQ grades in **Figure 8** and **Table 5**. While grades increase, one can observe that 2D- as well as 3D-quantification increased.
- ELH 3D-quantification values (see also **Figure 6**): The medians (ipsilateral, contralateral) of the vestibular data were (15 mm^3, 11 mm^3) for the MD group and (12 mm^3, 12 mm^3)

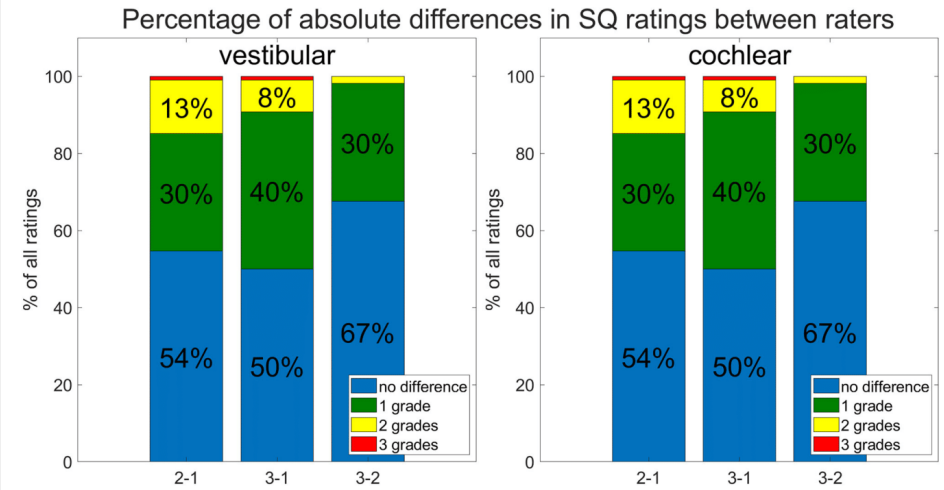

FIGURE 4 | Inter-rater and -threshold between ELH quantification methods (belonging to question ii). Shown are differences between the three raters. The differences between raters are shown as percentages of the total number of subjects rated. Most grades between raters agree (no difference; in blue), and the next largest difference was by 1 grade (in green), the remaining differences between raters were mostly 2 grades (in yellow) and rarely 3 grades (in red) apart.

for the vestibular healthy control (HC) group. The medians of the cochlear data were (5.4 mm^3, 4.6 mm^3) for the MD group and (4.6 mm^3, 4.7 mm^3) for the HC group.

- Total fluid space (TFS) 3D-quantification values of the vestibular and cochlear part of the inner ear [in mm^3] that were used for normalizing the data of each individual to generate ELS ratio (ER) [%], the percentage of the TFS occupied by the ELH. The medians (ipsilateral, contralateral) of the vestibular TFS data were (182 mm^3, 183 mm^3) for the MD group and (179 mm^3, 181 mm^3) for the HC group. The medians of the cochlear TFS data were (93 mm^3, 93 mm^3) for the MD group and (88 mm^3, 90 mm^3) for the HC group.
- Therefore, the medians (ipsilateral, contralateral) of the vestibular ER [%] data were (8.8%, 6.3%) for the MD group and (6.3%, 6.5%) for the HC group. The medians of the cochlear ER [%] data were (6.0%, 5.1%) for the MD group and (5.1%, 5.0%) for the HC group.
- ELH 2D-quantification values (see also **Figure 7**): The medians (ipsilateral, contralateral) of the vestibular data were (3.6 mm^2, 2.2 mm^2) for the MD group and (2.3 mm^2, 2.4 mm^2) for the vestibular healthy control (HC) group. The medians of the cochlear data were (1.2 mm^2, 0.8 mm^2) for the MD group and (1.1 mm^2, 1.0 mm^2) for the HC group.
- Total fluid surface (TFS) 2D-quantification values of the vestibular and cochlear part of the inner ear, in [mm^2] that were used for normalizing the data of each individual to generate ELS ratio (ER) [%], the percentage of the TFS occupied by the ELH. The medians (ipsilateral, contralateral) of the vestibular TFS data were (20.1 mm^2, 20.8 mm^2) for the MD group and (20.9 mm^2, 20.4 mm^2) for the HC group. The medians of the cochlear TFS data were (16.4 mm^2, 16.1 mm^2) for the MD group and (15.9 mm^2, 15.8 mm^2) for the HC group.
- Therefore, the medians (ipsilateral, contralateral) of the vestibular ER [%] data were (19.2%, 10.5%) for the MD group and (10.7%, 11.7%) for the HC group. The medians of the cochlear ER [%] data were (7.9%, 5.3%) for the MD group and (6.3%, 6.3%) for the HC group.

DISCUSSION

This methodological study with 108 participants (75 MD, 33 HC) focused on comparability and parametrization of different ELS quantification methods (SQ grading of three raters, 2D- or 3D-quantification of three cutoffs) used in iMRI and their (i) interrelations with subtle variations in data acquisition protocols (that influence SNR or SI); (ii) correlations to each other, clinical symptoms, or neurophysiological testing; and (iii) the influence of ELH on signal quality. The results were as follows: (i) Within the range of 0.1–0.2 mmol/kg (mean ± std: 0.16 ± 0.05 mmol/kg) Gd dosage and a 3 h 41 min to 5 h 19 min (mean ± std: 4 h 39 min ± 25 min) time delay, SQ gradings, and 2D- or 3D-quantifications were independent of signal intensity (SI) and signal-to-noise ratio (SNR), but they were found to be significantly related to Gd dosage and time delay themselves. (ii) The ELS quantification methods used were highly

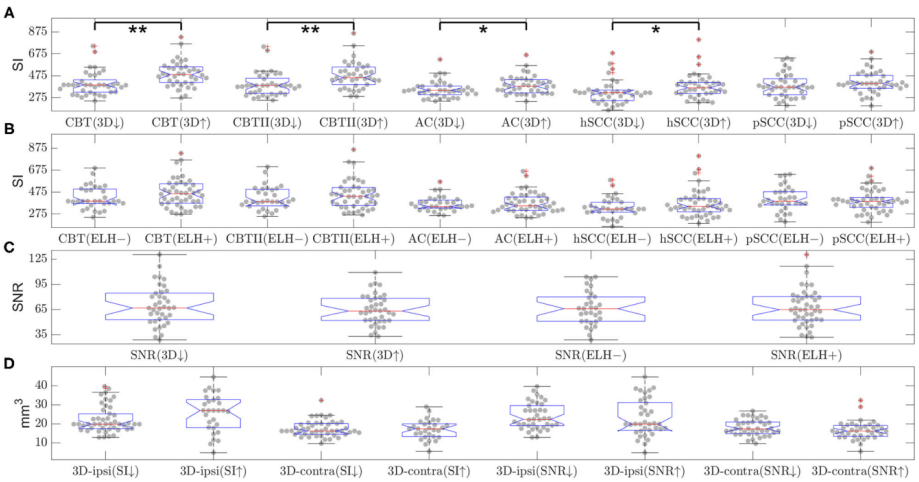

FIGURE 5 | Influence of endolymphatic hydrops (ELH) on signal intensity (SI) or signal-to-noise ratio (SNR) and vice versa (belonging to question iii). The top two rows **(A,B)** show the signal intensity (SI) in various areas of the inner ear. The SI values are split by either **(A)** 3D-quantification values (below or above median, indicated by a downward-arrow or an upward-arrow) or **(B)** endolymphatic hydrops (ELH) being absent ["−"] or present ["+"]. Here, "ELH absence" is defined as the average semi-quantitative (SQ) rating being zero and "ELH presence" is defined as the average rating being non-zero. Significant differences are indicated by black lines and p-values for the group differences evaluated with two-sample *t*-test or rank-sum test (**$p < 0.001$ and *$p < 0.05$). The third row **(C)** shows the mean SNR split by 3D-quantification values (below or above median; indicated by a downward-arrow or an upward-arrow), as well as the mean SNR split by ELH being absent ["−"] or present ["+"], where presence is defined as ELH being non-zero and absence as ELH rating being zero. The group differences were evaluated with the two-sample *t*-test and the rank-sum test; neither of these was significant. The fourth row **(D)** shows the 3D-quantification values split by mean SI values (below or above median; indicated by a downward-arrow or an upward-arrow), as well as the 3D-quantification values split by SNR values (below or above median; indicated by a downward-arrow or an upward-arrow). The group differences were evaluated with the two-sample *t*-test and the rank-sum test; neither of these was significant.

reproducible across raters (SQ gradings) or thresholds (2D- and 3D-quantification), although 3D-quantifications showed least variability in comparison to 2D-quantifications and SQ gradings. The relative proportions of both ears, and the relative size of ELH proved to be most useful for predicting quantitative clinical data from iMRI measures. (iii) ELH size significantly influenced SI but not SNR. In contrast, SI could not predict ELH size. In the following, results (i–iii) will be discussed.

Within a Specific Dosage and Time Delay Range ELS Quantification Methods Remain Independent of Signal Intensity (i)

The 3D fluid-attenuated inversion recovery (3D- FLAIR) imaging used has high sensitivity to low concentrations of Gd-based contrast agents (GBCA) in fluid compared with conventional T_1-weighted imaging (58). In particular, the heavily T_2-weighted 3D-FLAIR imaging with a long effective echo time is very sensitive to subtle T1 shortening and can detect low concentrations of GBCAs in the perilymphatic space after intravenous administration of a single dose of GBCA (18, 59, 60). In the tested Gd dosage and Gd time delay range (see above), at most weak influences on SNR and no influence on ELS quantification methods were found. It can therefore be assumed that, although Gd dosage and Gd time delay certainly have an influence on iMRI quality parameters, the sweet spot for ELH quantification by iMRI is within the range of the tested parameters. These results tie in well with earlier studies that showed strongest enhancement in 3D FLAIR sequences between 3 and 6 h (61), and optimally 4 h (62) after intravenous administration of 0.1 mmol/kg gadolinium diethylenetriaminepentaacetic acid (standard dose Gd-DTPA, Magnevist®), or 4.5 h (63) after intravenous administration of a standard dose gadoteridol (0.1 mmol/kg Gd-HP-DO3A, ProHance®), double dose (0.2 mmol/kg) Gd-HP-DO3A (64) or triple dose (0.3 mmol/kg) of Gd-DTPA-BMA, Omniscan® (65).

Another feature of the good performance within the chosen ranges may be the homogeneous distribution of the contrast agent in the entire volume of the inner ear (66, 67).

Further improvement of SNR and visualization in terms of rapid, morphological enhancement for analysis of the temporal and spatial distribution in the PLS of the inner ear can be achieved through careful selection of MR sequences (59, 68),

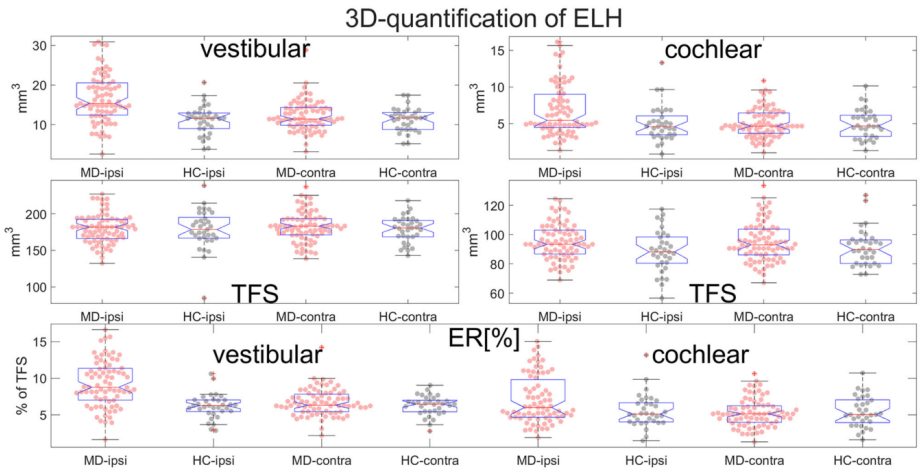

FIGURE 6 | Normalization and group differences for 3D-quantification of endolymphatic hydrops (ELH). 3D-quantification values of endolymphatic hydrops (ELH) in the vestibular and cochlear part of the inner ear [in mm^3] (top). 3D-quantification values of the total fluid space (TFS) of the vestibular and cochlear part of the inner ear [in mm^3] (middle row) that were used for normalizing the data of each individual to ELS ratio (ER) [%], the percentage of the TFS occupied by the ELH (bottom row).

combination (69, 70), and post-processing (14) of MR sequences, MR Gd complex (71), MR coil, and MR field strength (72).

Is There a Hierarchy Within ELS Quantification Methods? (ii)

In line with the only comparative methodological study of ELS quantification methods published to date in 11 participants (9 patients and 2 healthy controls) (26), SQ grading and 2D- or 3D- quantification methods were found to be reliable and useful for the diagnosis of endolymphatic hydrops. However, the degree of reliability based on comparisons between raters or thresholds increased from SQ grading to 2D- and again to 3D-quantification methods. The increase in repeatability corresponds to the decrease in dependency of human decision (visually > specific slice in 2D > whole volume in 3D) and increase of automatization and data points (semi-quantitative < area < volume).

Another aspect that makes relying solely on SQ grading tricky is the comparability of methods between different research groups, besides inter-rater disparities. SQ grading conventions (cf. **Table 1**) vary in grading resolution from three [in cochlea (19–21, 23) and vestibulum (19, 24, 25)] to four steps [in cochlea (22, 24, 25) and vestibulum (21–23)]. Accordingly, not all ELH grade results in cochlea or vestibulum correspond to each other due to the usage of different conventions [as an example grade 1 in (19, 20, 24)], or not at all [as an example (73)]. Based on either manually drawn (28, 74) regions of interest (ROIs) or a convolutional neural network (CNN) segmentation (32), 2D quantification methods already offer an increased comparability and variability of information. However, the comparability of the results remains limited by the slice selection for the calculation of the ratio and the differing slices emerging from slice planning or MRI setup (sequence type, slice thickness, slice resolution). Concerning these issues, 3D-quantification can be a solution (no slice selection, independent of slice planning) or at least an improvement (sequence type, slice thickness, slice resolution). In addition, more information (data points) enables better fitting of diagnostic and clinical parameters (75). Yet here, too, methodological variations affect reproducibility and availability of results. The critical points are the segmentation of the inner ear from the background [manually (29), via atlas (76, 77), or CNN (31); (Ahmadi et al., under review)] and the ELS and PLS from the TFS [manually (26), semi-automatic (29), automatic (31)], as well as the availability of the software solutions [commercial (26, 28, 29, 78) vs. open source (31)]. The less human-dependent and the more automated, the more reproducible the method in most cases. Therefore, the usefulness of the available quantification methods depends on its intended application. While visual SQ grading is highly useful in a clinical setting, automated 3D-quantification seems most suitable for research.

ELS Patterns in MD, HC (ii)

Significant differences between groups could especially be found for the ipsilateral (or affected) side of the MD group vs. HC group, as was already shown for 4-point [cochlea: (24, 25)] and 3-point [cochlea: (79); vestibulum: (80); sacculum (81)] ELS SQ

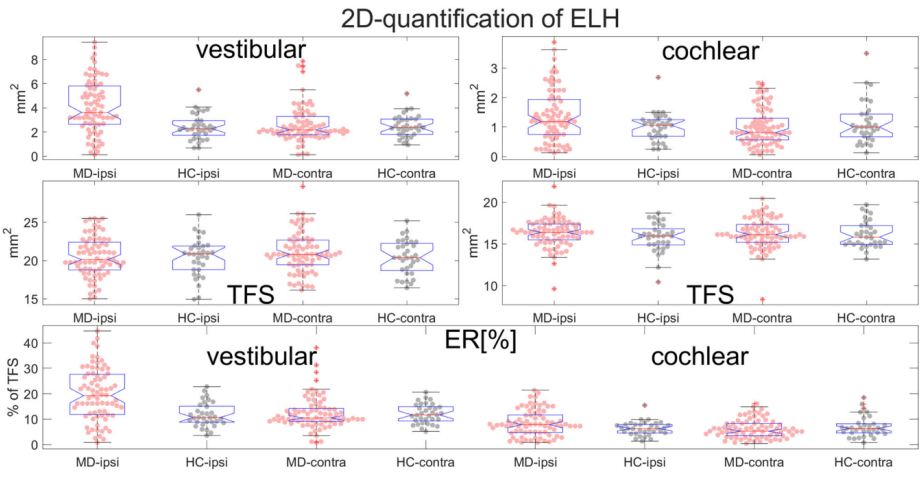

FIGURE 7 | Normalization and group differences for 2D-quantification of endolymphatic hydrops (ELH). 2D-quantification values of endolymphatic hydrops (ELH) in the vestibular and cochlear part of the inner ear, in [mm^2] (top row). 2D-quantification values of the total fluid surface (TFS) of the vestibular and cochlear part of the inner ear, in [mm^2] (middle row) that were used for normalizing the data of each individual to ELS ratio (ER) [%], the percentage of the TFS occupied by the ELH (bottom row).

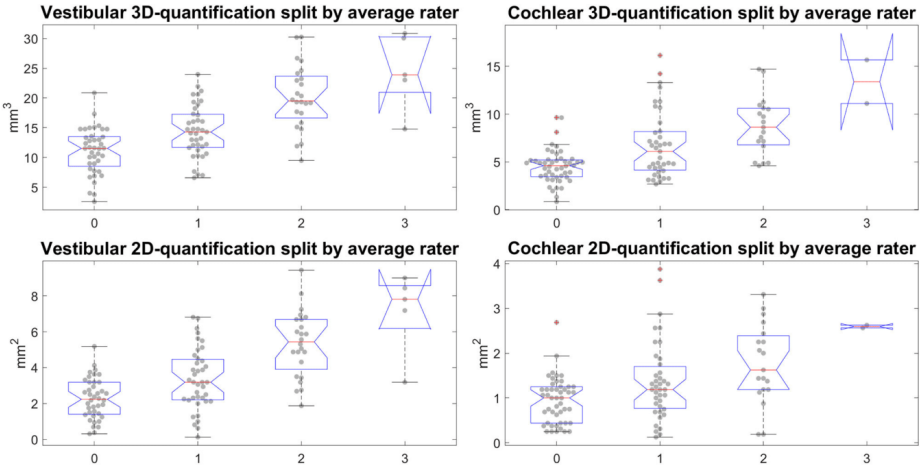

FIGURE 8 | Semi-quantitative (SQ) grade-specific 2D- and 3D-quantification values. These four plots show the quantitative endolymphatic hydrops (ELH) measures (3D-quantification in the top row and 2D-quantification in the bottom row) split up along the semi-quantitative visual grading steps (from grade 0 to grade 3 in steps of 1). This means each boxplot with data points overlaid shows the distribution of quantitative measures that correspond to the respective grading. The grading here is of the average over the three raters, rounded to the nearest integer to preserve gradings going from 0 to 3 in steps of 1. The top row shows the distributions for the 3D-quantification of ELH for vestibular and cochlear parts of the inner ear, left and right, respectively, while the bottom row shows the distributions for the 2D-quantification of ELH for vestibular and cochlear parts of the inner ear.

TABLE 5 | SQ-specific 2D- and 3D-quantification of the ELS.

			Grade 0 No hydrops Mean ± std (min–max)	Grade 1 Mild hydrops Mean ± std (min–max)	Grade 2 Marked hydrops Mean ± std (min–max)	Grade 3 Severe hydrops Mean ± std (min–max)
(A) 2D-quantification						
c6	Inner ear [mm^2]	R1-3	2.15 ± 1.32 (0.25–4.81)	3.57 ± 1.81 (0.19–6.81)	5.91 ± 1.92 (2.44–9.75)	6.31 ± 2.75 (3.19–8.38)
	Cochlea [mm^2]	R1-3	0.56 ± 0.40 (0–1.31)	0.96 ± 0.77 (0–3)	1.29 ± 0.72 (0.06–2.56)	1.78 ± 0.13 (1.69–1.88)
	Vestibulum [mm^2]	R1-3	1.88 ± 1.24 (0.13–4.25)	2.67 ± 1.62 (0–5.63)	4.18 ± 1.68 (1.13–8.63)	5.89 ± 2.04 (2.56–8)
c8	Inner ear [mm^2]	R1-3	3.08 ± 1.54 (0.63–6.00)	4.77 ± 2.07 (0.5–8.5)	7.59 ± 2.20 (3.25–11.13)	8.19 ± 3.32 (4.38–10.44)
	Cochlea [mm^2]	R1-3	0.89 ± 0.51 (0.25–1.94)	1.38 ± 0.92 (0.13–3.88)	1.76 ± 0.89 (0.19–3.31)	2.59 ± 0.04 (2.56–2.63)
	Vestibulum [mm^2]	R1-3	2.45 ± 1.39 (0.31–5.19)	3.45 ± 1.84 (0.13–6.81)	5.34 ± 1.84 (1.88–9.44)	7.13 ± 2.30 (3.19–9)
c10	Inner ear [mm^2]	R1-3	4.46 ± 1.87 (1.44–7.63)	6.01 ± 2.27 (1.19–10.63)	9.07 ± 2.28 (4.38–12.75)	9.77 ± 3.26 (6.06–12.19)
	Cochlea [mm^2]	R1-3	1.31 ± 0.54 (0.56–2.13)	1.84 ± 1.00 (0.44–4.44)	2.25 ± 1.00 (0.44–3.88)	3.22 ± 0.04 (3.19–3.25)
	Vestibulum [mm^2]	R1-3	3.21 ± 1.64 (0.56–6.38)	4.24 ± 1.98 (0.56–8)	6.25 ± 1.98 (2.19–10.13)	8.10 ± 2.56 (3.81–10.31)
TFS	Cochlea [mm^2]	R1-3	15.54 ± 1.49 (12.63–18.63)	16.64 ± 1.20 (14.13–9.63)	16.59 ± 2.48 (9.63–21.88)	16.50 ± 1.24 (15.63–17.38)
	Vestibulum [mm^2]	R1-3	19.45 ± 2.92 (15.00–24.63)	20.63 ± 2.66 (15.63–25.5)	20.78 ± 2.13 (17.31–25.19)	21.74 ± 3.03 (18–25.5)
c6	Inner ear ER [%]	R1-3	6.10 ± 3.74 (0.85–13.68)	9.54 ± 4.72 (0.64–17.76)	15.71 ± 4.90 (5.58–25.12)	16.99 ± 7.20 (8.73–21.93)
	Cochlea ER [%]	R1-3	3.51 ± 2.43 (0.00–7.78)	5.67 ± 4.33 (0–16.78)	7.93 ± 4.35 (0.29–14.96)	10.80 ± 0.01 (10.79–10.8)
	Vestibulum ER [%]	R1-3	9.50 ± 6.43 (0.82–21.79)	12.78 ± 7.61 (0–25.07)	20.09 ± 7.76 (5.96–40.83)	27.02 ± 8.95 (12.97–37.10)
c8	Inner ear ER [%]	R1-3	8.78 ± 4.36 (2.12–17.05)	12.75 ± 5.29 (1.71–21.55)	20.20 ± 5.64 (6.91–28.50)	22.10 ± 8.95 (11.99–29.00)
	Cochlea ER [%]	R1-3	5.65 ± 3.09 (1.44–11.48)	8.22 ± 5.14 (0.78–21.38)	10.83 ± 5.34 (0.86–18.90)	15.75 ± 0.91 (15.11–16.4)
	Vestibulum ER [%]	R1-3	12.49 ± 7.18 (2.08–26.60)	16.46 ± 8.52 (0.79–30.36)	25.71 ± 8.55 (9.93–44.67)	32.72 ± 10.1 (16.14–41.74)
c10	Inner ear ER [%]	R1-3	12.70 ± 5.20 (4.88–21.67)	16.10 ± 5.75 (4.06–27.96)	24.16 ± 5.91 (9.30–31.88)	26.35 ± 8.60 (16.61–32.90)
	Cochlea ER [%]	R1-3	8.34 ± 3.33 (3.94–15.25)	10.95 ± 5.58 (2.23–24.49)	13.84 ± 6.11 (2.57–21.99)	19.57 ± 1.74 (18.35–20.80)
	Vestibulum ER [%]	R1-3	16.34 ± 8.41 (3.75–32.69)	20.31 ± 9.01 (3.54–37.85)	30.07 ± 9.20 (11.59–47.93)	37.15 ± 10.9 (19.30–47.83)
(B) 3D-quantification						
c6	Inner ear [mm^3]	R1-3	11.17 ± 3.85 (2.70–19.11)	14.52 ± 4.97 (7.48–27.97)	22.78 ± 5.54 (13.50–32.76)	23.13 ± 8.61 (13.50–30.10)
	Cochlea [mm^3]	R1-3	3.15 ± 1.23 (0.76–6.20)	4.65 ± 2.93 (1.5–12.91)	6.49 ± 2.51 (2.89–11.80)	10.62 ± 2.62 (8.77–12.46)
	Vestibulum [mm^3]	R1-3	8.27 ± 3.25 (1.38–14.53)	10.43 ± 3.63 (4.52–17.96)	14.81 ± 4.68 (5.56–25.53)	18.23 ± 5.43 (10.19–24.39)
c8	Inner ear [mm^3]	R1-3	16.59 ± 5.24 (4.81–26.95)	20.73 ± 6.03 (11.02–36.47)	30.61 ± 6.78 (19.10–44.54)	31.16 ± 10.2 (19.78–39.56)
	Cochlea [mm^3]	R1-3	4.58 ± 1.60 (1.31–8.11)	6.57 ± 3.51 (2.67–16.14)	8.73 ± 3.00 (4.59–14.70)	13.39 ± 3.22 (11.11–15.67)
	Vestibulum [mm^3]	R1-3	12.29 ± 4.39 (2.56–20.86)	14.78 ± 4.48 (7–23.98)	20.12 ± 5.42 (9.48–30.26)	24.53 ± 6.49 (14.78–30.87)
c10	Inner ear [mm^3]	R1-3	23.06 ± 6.63 (7.97–35.78)	27.87 ± 6.83 (15.34–44.95)	38.85 ± 8.05 (24.97–56.85)	39.68 ± 11.5 (27.13–49.73)
	Cochlea [mm^3]	R1-3	6.38 ± 2.03 (2.05–10.05)	8.74 ± 3.96 (4.02–18.84)	11.12 ± 3.38 (6.19–18.26)	16.15 ± 4.24 (13.16–19.15)
	Vestibulum [mm^3]	R1-3	17.10 ± 5.45 (4.64–27.53)	19.78 ± 5.19 (9.52–29.81)	25.78 ± 6.15 (14.06–36.55)	31.28 ± 7.41 (20.41–38.59)
TFS	Cochlea [mm^3]	R1-3	90.0 ± 10.6 (68.96–105.82)	95.4 ± 11.2 (74.25–117.52)	99.90 ± 14.1 (75.5–124.47)	97.1 ± 17.6 (84.63–109.56)
	Vestibulum [mm^3]	R1-3	178.6 ± 18.3 (149.7–219.7)	181.2 ± 23.3 (132.2.0.0.221.7)	176.8 ± 18.2 (140.3–227.3)	190.4 ± 11.2 (175.0–199.6)
c6	Inner ear ER [%]	R1-3	4.12 ± 1.23 (1.15–6.25)	5.32 ± 1.83 (2.90–9.82)	8.05 ± 1.68 (4.46–10.73)	8.25 ± 2.84 (4.98–9.94)
	Cochlea ER [%]	R1-3	3.49 ± 1.48 (1.10–8.19)	4.76 ± 2.67 (1.49–12.02)	6.55 ± 2.46 (2.59–11.11)	10.87 ± 0.72 (10.36–11.38)
	Vestibulum ER [%]	R1-3	4.57 ± 1.63 (0.87–7.07)	5.82 ± 2.04 (2.43–9.62)	8.30 ± 2.26 (3.57–13.20)	9.51 ± 2.51 (5.60–12.22)
c8	Inner ear ER [%]	R1-3	6.13 ± 1.66 (2.04–8.82)	7.60 ± 2.21 (4.44–12.81)	10.83 ± 2.04 (6.18–14.11)	11.12 ± 3.32 (7.29–13.15)
	Cochlea ER [%]	R1-3	5.07 ± 1.86 (1.90–10.71)	6.76 ± 3.17 (2.78–15.03)	8.81 ± 2.90 (3.88–13.85)	13.71 ± 0.83 (13.13–14.3)
	Vestibulum ER [%]	R1-3	6.79 ± 2.17 (1.62–10.14)	8.24 ± 2.54 (3.99–12.84)	11.30 ± 2.53 (6.09–16.61)	12.81 ± 2.96 (8.12–15.47)
c10	Inner ear ER [%]	R1-3	8.53 ± 2.07 (3.38–11.71)	10.20 ± 2.47 (6.19–15.79)	13.75 ± 2.42 (8.28–17.95)	14.16 ± 3.61 (10.0–16.25)
	Cochlea ER [%]	R1-3	7.04 ± 2.25 (2.98–13.26)	9.03 ± 3.52 (4.21–17.54)	11.24 ± 3.29 (5.36–16.24)	16.51 ± 1.37 (15.55–17.48)
	Vestibulum ER [%]	R1-3	9.48 ± 2.66 (2.94–13.39)	11.01 ± 2.95 (5.99–15.97)	14.50 ± 2.79 (9.03–20.09)	16.35 ± 3.29 (11.22–19.42)

grading, 2D-quantification [cochlea: (82); vestibulum: (82)] and 3D-quantification [cochlea: (30, 57); vestibulum: (30, 57)] results.

Clinical variables correlated highest with symmetry parameters derived from SQ grading and 2D- or 3D-quantification values such as the asymmetry index (*AI*) or the plain ELH difference between ipsilateral and contralateral side for the inner ear, vestibulum, and cochlea. Recent studies using ELS asymmetry indexes confirm this inclination (57). A more detailed clinical study and discussion can be found in another work (76). To date, correlations were found for

SQ grades 3-point [electrocochleography (EcochG) (83, 84)] and 4-point ordinal cochlear scale [PTA (24–26, 79); auditory symptoms (85, 86); disease duration (24, 79); but not for the glycerol test (25)]. Furthermore, correlations were found for 3-point ordinal vestibular scale [cVEMP-side difference (SD) (24); PTA (11, 25, 87); oVEMP-amplitudes (88), but not with VOG during caloric stimulation SD (24, 89) or the glycerol test (25)]. SQ correlations coincided with 2D-quantification [cochlea: PTA (82); vestibulum: SP/AP ratio of ECoG (82)] and 3D-quantification [cochlea: PTA (26); vestibulum: duration of illness >30 months (26), side difference in response to caloric irrigation (57)] correlation results.

ELH Extent Influences Signal Intensity in the Basal Cochlear Turn (iii)

Zhang et al. (90) investigated 19 MD patients following double-dose iMRI and found that the signal intensity ratio of the cochlear basal turns in the affected ear was significantly higher than in the unaffected ear and that there was a positive correlation between the signal intensity ratio of the cochlear basal turn and the grades of cochlear and vestibular hydrops in the affected ear. The SNR was assessed and calculated manually according to (91) using the signal in perilymph of both cochlear basal turns and noise in coplanar circular 50 mm^2 ROIs in the cerebellum. The interpretation of these findings was that increased permeability of the blood-labyrinth barrier (higher SNR) may play a role in the process of endolymphatic hydrops in MD.

The results of the current study suggest, however, a general pathophysiological effect tied to the extent of the ELH and not MD as a pathology, since higher ELH 3D-quantification values had higher signal intensity (SI) values in the cochlear basal turn, apex cochlea, and hSCC ROIs. Within MD, SI only in the cochlear basal turn was significantly higher on the ipsilateral side when compared to the contralateral side. The SI was generally different between the MD and HC groups, indicating an effect of ELH also on signal presentation. SNR differed between the MD and HC groups; however, the effect was small and the group differences in ELH were not significantly affected by SNR, indicating that the group differences are a persistent effect of the underlying condition and not related to the imaging settings that were used in the current study.

Normalization and Standardization of ELS Values

Clinical variables correlated better and more correctly with relative (AI) or normalized values [to the fraction ER [%] of the total fluid space]. This indicates that relative proportions of both ears, and the relative size of ELH are most useful for predicting quantitative clinical data from iMRI measures (57).

However, to date not many iMRI ELS values have been published in absolute (26, 30, 92) and relative sizes (26, 28, 85, 93–95); those that have been published were mostly group-specific but not grade-specific, and one grade-specific but relative (26). In **Table 5**, 2D- and 3D-quantifications, relative, and normalized to TFS are presented.

Recommendations for Future iMRI Studies

The following methodological recommendations for future studies can be derived from the present work and the current available literature:

- MR setup: Improved hybrid of reversed image of positive endolymph signal and native image of positive perilymph signal (iHYDROPS-Mi2) (15) or 3D-real inversion recovery (3D-real IR) (28, 96), highest possible MRI field strength (72), smallest possible isotropic voxel size, deep learning reconstruction denoising (14) if applicable.
- MR measurement: 4 h ±30 min after single-dose (0.1 mmol/kg) intravenous application (64) of Dotarem (Gd-DOTA, 100% morphological enhancement) or Gadovist (Gd-Do3A, 88% morphological enhancement) (71).
- SQ grading: 4-point ordinal scale (0: no hydrops, 1: mild hydrops, 2: marked hydrops, 3: severe hydrops) for cochlear and vestibular SQ grading (cp. **Table 1**), preferably with a level of evaluation reconstructed to distinctive anatomical fixpoints.
- Scalar ELS values: 3D-quantification, optimally using algorithm-based segmentation of both the TFS (Seyed-Ahmad et al., under review); (76, 77) and ELS (31, 32) should be included. 2D-quantification if 3D-quantification is not available. Reported values should be normalized for TFS size.
- Correlations with clinical variables should include both ears and are most promising in symmetry parameters, such as asymmetry-indices for un-normalized data and relative size ELS for normalized data.

Methodological Limitations and Outlook

There are methodological limitations in the current study that need to be considered in the interpretation of the data. First, despite the comparatively wide range of contrast agent dosage and delay time within this study, the results should be (to some degree) considered specific to the study's MR settings (MR sequence, MR contrast agent, intravenous application). Second, despite the extensive analyses within this study, it was not possible to try all, but only representations of the methods used in this study [SQ following **Figure 1** and (22), 2D- and 3D-quantification using VOLT (31)]. Third, the study lacks histological confirmation of endolymphatic hydrops. However, the *in-vivo* acquisition of histological specimens in Menière's disease is currently not possible. Fourth, the size of the control group ($n = 33$) was small in comparison to the MD group ($n = 105$). However, due to findings of signal intensity in the dendate nucleus and globus pallidus on unenhanced T1-weighted MR images (97–99) that are still under investigation, measurements were restricted to inpatients of the Department of Neurology that underwent MRI with a contrast agent as part of their diagnostic workup and agreed to undergo iMRI sequences after 4 h.

CONCLUSION

The current comparative methodological study has shown that: (1) A Gd dosage of 0.1–0.2 mmol/kg after 4 h ± 30 min Gd time delay will provide sufficient SNR when using recommended MR sequences and contrast agents. (2) An agreed upon clinical SQ

grading classification including a standardized level of evaluation reconstructed to anatomical fixpoints is needed to provide unambiguous comparability between labs. (3) 3D-quantification methods of the ELS using algorithm-based segmentation of the TFS and ELS seem to be best suited for research purposes. Correlations with clinical variables should include both ears and ELS values reported relative or normalized to size. (4) The presence of ELH increases signal intensity in the basal cochlear turn weakly, but cannot predict the presence of ELH.

DATA AVAILABILITY STATEMENT

The original contributions presented in the study are included in the article/supplementary material, further inquiries can be directed to the corresponding author/s.

ETHICS STATEMENT

The studies involving human participants were reviewed and approved by Ethics Committee of the Medical Faculty of the Ludwig-Maximilians-Universität, Munich, Germany. The patients/participants provided their written informed consent to participate in this study.

AUTHOR CONTRIBUTIONS

RB: conception and design of the study, analysis of the data, and drafting the manuscript. JG, EK, SB-B, and BE-W: acquisition, analysis of the data, and drafting of the manuscript. MD: conception and design of the study, drafting the manuscript, and providing funding. VK: conception and design of the study, acquisition, analysis of the data, drafting the manuscript, and providing funding. All authors contributed to the article and approved the submitted version.

FUNDING

This work was partially funded by the Friedrich-Baur-Stiftung (FBS), the German Federal Ministry of Education and Research (BMBF) in connection with the foundation of the German Center for Vertigo and Balance Disorders (DSGZ; grant number 01 EO 0901) and the German Research Foundation (DFG) in connection with the Munich Cluster for Systems Neurology (SyNergy; grant number: EXC2145, project ID: 390857198), and the German Foundation for Neurology (DSN).

ACKNOWLEDGMENTS

This was part of the dissertation of JG. We thank K. Göttlinger for copyediting the manuscript.

REFERENCES

1. Strupp M, Brandt T, Dieterich M. *Vertigo - Leitsymptom Schwindel*. 3rd ed. Berlin Heidelberg: Springer-Verlag (2021). doi: 10.1007/978-3-662-61397-9
2. Pyykkö I, Zou J, Gürkov R, Naganawa S, Nakashima T. Imaging of temporal bone. *Adv Otorhinolaryngol.* (2019) 82:12–31. doi: 10.1159/000490268
3. van der Lubbe MFJA, Vaidyanathan A, Van Rompaey V, Postma AA, Bruintjes TD, Kimenai DM, et al. The "hype" of hydrops in classifying vestibular disorders: a narrative review. *J Neurol.* (2020) 267:197–211. doi: 10.1007/s00415-020-10278-8
4. Rauch SD, Merchant SN, Thedinger BA. Meniere's syndrome and endolymphatic hydrops. Double-blind temporal bone study. *Ann Otol Rhinol Laryngol.* (1989) 98:873–83. doi: 10.1177/000348948909801108
5. Nakashima T, Pyykkö I, Arroll MA, Casselbrant ML, Foster CA, Manzoor NF, et al. Meniere's disease. *Nat Rev Dis Prim.* (2016) 2:16028. doi: 10.1038/nrdp.2016.28
6. Nakada T, Yoshida T, Suga K, Kato M, Otake H, Kato K, et al. Endolymphatic space size in patients with vestibular migraine and Ménière's disease. *J Neurol.* (2014) 261:2079–84. doi: 10.1007/s00415-014-7458-9
7. Suga K, Kato M, Yoshida T, Nishio N, Nakada T, Sugiura S, et al. Changes in endolymphatic hydrops in patients with Ménière's disease treated conservatively for more than 1 year. *Acta Oto-Laryngologica.* (2015) 135:866–70. doi: 10.3109/00016489.2015.1015607
8. Attyé A, Eliezer M, Galloux A, Pietras J, Tropres I, Schmerber S, et al. Endolymphatic hydrops imaging: differential diagnosis in patients with Meniere disease symptoms. *Diagn Interv Imaging.* (2017) 98:699–706. doi: 10.1016/j.diii.2017.06.002
9. Kirsch V, Ertl-Wagner B, Berman A, Gerb J, Dieterich M, Becker-Bense S. High-resolution MRI of the inner ear enables syndrome differentiation and specific treatment of cerebellar downbeat nystagmus and secondary endolymphatic hydrops in a postoperative ELST patient. *J Neurol.* (2018) 265:48–50. doi: 10.1007/s00415-018-8858-z
10. Zwergal A, Kirsch V, Gerb J, Dlugaiczyk J, Becker-Bense S, Dieterich M. Neurootologie: Grenzfälle zwischen Ohr und Gehirn. *Nervenarzt.* (2018) 89:1106–14. doi: 10.1007/s00115-018-0598-x
11. Attyé A, Eliezer M, Medici M, Tropres I, Dumas G, Krainik A, et al. In vivo imaging of saccular hydrops in humans reflects sensorineural hearing loss rather than Meniere's disease symptoms. *Eur Radiol.* (2018) 28:2916–22. doi: 10.1007/s00330-017-5260-7
12. Eliezer M, Hautefort C, Van Nechel C, Duquesne U, Guichard J-P, Herman P, et al. Electrophysiological and inner ear MRI findings in patients with bilateral vestibulopathy. *Eur Arch Otorhinolaryngol.* (2020) 277:1305–14. doi: 10.1007/s00405-020-05829-8
13. Jerin C, Krause E, Ertl-Wagner B, Gürkov R. Clinical features of delayed endolymphatic hydrops and intralabyrinthine schwannoma : an imaging-confirmed comparative case series. English version. *HNO.* (2017) 65:41–5. doi: 10.1007/s00106-016-0199-6
14. Naganawa S, Nakamichi R, Ichikawa K, Kawamura M, Kawai H, Yoshida T, et al. MR imaging of endolymphatic hydrops: utility of iHYDROPS-Mi2 combined with deep learning reconstruction denoising. *Magn Reson Med Sci.* (2020) doi: 10.2463/mrms.mp.2020-0082. [Epub ahead of print].
15. Naganawa S, Kawai H, Taoka T, Sone M. Improved HYDROPS: Imaging of endolymphatic hydrops after intravenous administration of gadolinium. *Magn Reson Med Sci.* (2017) 16:357–61. doi: 10.2463/mrms.tn.2016-0126
16. Yamazaki M, Naganawa S, Tagaya M, Kawai H, Ikeda M, Sone M, et al. Comparison of contrast effect on the cochlear perilymph after intratympanic and intravenous gadolinium injection. *Am J Neuroradiol.* (2012) 33:773–8. doi: 10.3174/ajnr.A2821
17. Naganawa S, Satake H, Iwano S, Fukatsu H, Sone M, Nakashima T. Imaging endolymphatic hydrops at 3 tesla using 3D-FLAIR with intratympanic Gd-DTPA administration. *Magn Reson Med Sci.* (2008) 7:85–91. doi: 10.2463/mrms.7.85
18. Naganawa S, Yamazaki M, Kawai H, Bokura K, Sone M, Nakashima T. Visualization of endolymphatic hydrops in Ménière's disease with single-dose intravenous gadolinium-based contrast media using heavily T(2)-weighted 3D-FLAIR. *Magn Reson Med Sci.* (2010) 9:237–42. doi: 10.2463/mrms.9.237

19. Nakashima T, Naganawa S, Pyykko I, Gibson WPR, Sone M, Nakata S, et al. Grading of endolymphatic hydrops using magnetic resonance imaging. *Acta Otolaryngol Suppl.* (2009) 560:5–8. doi: 10.1080/00016480902729827
20. Baráth K, Schuknecht B, Naldi AM, Schrepfer T, Bockisch CJ, Hegemann SCA. Detection and grading of endolymphatic hydrops in Menière disease using MR imaging. *Am J Neuroradiol.* (2014) 35:1387–92. doi: 10.3174/ajnr.A3856
21. Bernaerts A, Vanspauwen R, Blaivie C, van Dinther J, Zarowski A, Wuyts FL, et al. The value of four stage vestibular hydrops grading and asymmetric perilymphatic enhancement in the diagnosis of Menière's disease on MRI. *Neuroradiology.* (2019) 61:421–9. doi: 10.1007/s00234-019-02155-7
22. Kirsch V, Becker-Bense S, Berman A, Kierig E, Ertl-Wagner B, Dieterich M. Transient endolymphatic hydrops after an attack of vestibular migraine: a longitudinal single case study. *J Neurol.* (2018) 265(Suppl. 1):51–3. doi: 10.1007/s00415-018-8870-3
23. Bernaerts A, De Foer B. Imaging of Ménière disease. *Neuroimaging Clin North Am.* (2019) 29:19–28. doi: 10.1016/j.nic.2018.09.002
24. Gürkov R, Flatz W, Louza J, Strupp M, Ertl-Wagner B, Krause E. *In vivo* visualized endolymphatic hydrops and inner ear functions in patients with electrocochleographically confirmed Ménière's disease. *Otol Neurotol.* (2012) 33:1040–5. doi: 10.1097/MAO.0b013e31825d9a95
25. Yang S, Zhu H, Zhu B, Wang H, Chen Z, Wu Y, et al. Correlations between the degree of endolymphatic hydrops and symptoms and audiological test results in patients with Menière's disease: a reevaluation. *Otol Neurotol.* (2018) 39:351–6. doi: 10.1097/MAO.0000000000001675
26. Homann G, Vieth V, Weiss D, Nikolaou K, Heindel W, Notohamiprodjo M, et al. Semi-quantitative vs. volumetric determination of endolymphatic space in Menière's disease using endolymphatic hydrops 3T-HR-MRI after intravenous gadolinium injection. *PLoS ONE.* (2015) 10:e0120357. doi: 10.1371/journal.pone.0120357
27. Naganawa S, Suzuki K, Nakamichi R, Bokura K, Yoshida T, Sone M, et al. Semi-quantification of endolymphatic size on MR imaging after intravenous injection of single-dose gadodiamide: comparison between two types of processing strategies. *Magn Reson Med Sci.* (2013) 12:261–9. doi: 10.2463/mrms.2013-0019
28. Ohashi T, Naganawa S, Takeuchi A, Katagiri T, Kuno K. Quantification of endolymphatic space volume after intravenous administration of a single dose of gadolinium-based contrast agent: 3D-real inversion recovery versus HYDROPS-Mi2. *Magn Reson Med Sci.* (2019) 19:119–24. doi: 10.2463/mrms.mp.2019-0013
29. Gürkov R, Berman A, Dietrich O, Flatz W, Jerin C, Krause E, et al. MR volumetric assessment of endolymphatic hydrops. *Eur Radiol.* (2015) 25:585–95. doi: 10.1007/s00330-014-3414-4
30. Inui H, Sakamoto T, Ito T, Kitahara T. Magnetic resonance-based volumetric measurement of the endolymphatic space in patients with Meniere's disease and other endolymphatic hydrops-related diseases. *Auris Nasus Larynx.* (2019) 46:493–7. doi: 10.1016/j.anl.2018.11.008
31. Gerb J, Ahmadi SA, Kierig E, Ertl-Wagner B, Dieterich M, Kirsch V. VOLT: a novel open-source pipeline for automatic segmentation of endolymphatic space in inner ear MRI. *J Neurol.* (2020) 267:185–96. doi: 10.1007/s00415-020-10062-8
32. Cho YS, Cho K, Park CJ, Chung MJ, Kim JH, Kim K, et al. Automated measurement of hydrops ratio from MRI in patients with Ménière's disease using CNN-based segmentation. *Sci Rep.* (2020) 10:7003. doi: 10.1038/s41598-020-63887-8
33. Lopez-Escamez JA, Carey J, Chung W-H, Goebel JA, Magnusson M, Mandalà M, et al. Diagnostic criteria for Menière's disease. *J Vestib Res.* (2015) 25:1–7. doi: 10.3233/VES-150549
34. Oldfield RC. The assessment and analysis of handedness: the Edinburgh inventory. *Neuropsychologia.* (1971) 9:97–113. doi: 10.1016/0028-3932(71)90067-4
35. Salmaso D, Longoni AM. Problems in the assessment of hand preference. *Cortex.* (1985) 21:533–49. doi: 10.1016/s0010-9452(58)80003-9
36. Dill T. Contraindications to magnetic resonance imaging. *Heart.* (2008) 94:943–8. doi: 10.1136/hrt.2007.125039
37. Matsumoto M, Nishimura T. Mersenne twister: a 623-dimensionally equidistributed uniform pseudo-random number generator. *ACM Trans Model Comput Simul.* (1998) 8:3–30. doi: 10.1145/272991.272995
38. Dieterich M, Brandt T. Ocular torsion and tilt of subjective visual vertical are sensitive brainstem signs. *Ann Neurol.* (1993) 33:292–9. doi: 10.1002/ana.410330311
39. Halmagyi GM, Curthoys IS. A clinical sign of canal paresis. *Arch Neurol.* (1988) 45:737–9. doi: 10.1001/archneur.1988.00520310043015
40. Schneider E, Villgrattner T, Vockeroth J, Bartl K, Kohlbecher S, Bardins S, et al. EyeSeeCam: an eye movement-driven head camera for the examination of natural visual exploration. *Ann N Y Acad Sci.* (2009) 1164:461–7. doi: 10.1111/j.1749-6632.2009.03858.x
41. Strupp M, Kim J-S, Murofushi T, Straumann D, Jen JC, Rosengren SM, et al. Bilateral vestibulopathy: diagnostic criteria consensus document of the classification committee of the Bárány society. *J Vestib Res.* (2017) 27:177–89. doi: 10.3233/VES-170619
42. Jongkees LB, Maas JP, Philipszoon AJ. Clinical nystagmography. A detailed study of electro-nystagmography in 341 patients with vertigo. *Pract Otorhinolaryngol.* (1962) 24:65–93.
43. Dlugaiczyk J, Habs M, Dieterich M. Vestibular evoked myogenic potentials in vestibular migraine and Menière's disease: cVEMPs make the difference. *J Neurol.* (2020) 267(Suppl. 1):169–80. doi: 10.1007/s00415-020-09902-4
44. Curthoys IS, Dlugaiczyk J. Physiology, clinical evidence and diagnostic relevance of sound-induced and vibration-induced vestibular stimulation. *Curr Opin Neurol.* (2020) 33:126–35. doi: 10.1097/WCO.0000000000000770
45. Ertl M, Boegle R, Kirsch V, Dieterich M. On the impact of examiners on latencies and amplitudes in cervical and ocular vestibular-evoked myogenic potentials evaluated over a large sample (N = 1,038). *Eur Arch Otorhinolaryngol.* (2016) 273:317–23. doi: 10.1007/s00405-015-3510-3
46. Nahmani S, Vaussy A, Hautefort C, Guichard J-P, Guillonet A, Houdart E, et al. Comparison of enhancement of the vestibular perilymph between variable and constant flip angle-delayed 3D-FLAIR sequences in Menière disease. *Am J Neuroradiol.* (2020) doi: 10.3174/ajnr.A6483
47. Legland D, Arganda-Carreras I, Andrey P. MorphoLibJ: integrated library and plugins for mathematical morphology with ImageJ. *Bioinformatics.* (2016) 32:3532–4. doi: 10.1093/bioinformatics/btw413
48. Schindelin J, Arganda-Carreras I, Frise E, Kaynig V, Longair M, Pietzsch T, et al. Fiji: an open-source platform for biological-image analysis. *Nat Methods.* (2012) 9:676–82. doi: 10.1038/nmeth.2019
49. Székely GJ, Rizzo ML. Energy statistics: a class of statistics based on distances. *J Statist Plan Inference.* (2013) 143:1249–72. doi: 10.1016/j.jspi.2013.03.018
50. Gretton A, Borgwardt K, Rasch M, Schölkopf B, Smola A. A kernel two-sample test. *J Mach Learn Res.* (2012) 13:723–73. doi: 10.5555/2503308.2188410
51. Milletari F, Navab N, Ahmadi S-A. V-Net: fully convolutional neural networks for volumetric medical image segmentation. *arXiv:160604797.* (2016). Available online at: http://arxiv.org/abs/1606.04797
52. Milletari F, Frei J, Aboulatta M, Vivar G, Ahmadi S-A. Cloud deployment of high-resolution medical image analysis with TOMAAT. *IEEE J Biomed Health Inform.* (2019) 23:969–77. doi: 10.1109/JBHI.2018.2885214
53. Fedorov A, Beichel R, Kalpathy-Cramer J, Finet J, Fillion-Robin J-C, Pujol S, et al. 3D slicer as an image computing platform for the quantitative imaging network. *Magn Reson Imaging.* (2012) 30:1323–41. doi: 10.1016/j.mri.2012.05.001
54. Nizamutdinov V. *Neural Network and Fuzzy Logic Based Plugins for ImageJ.* (2015). Available online at: https://github.com/astartes91/imagej-neural-fuzzy-plugins
55. Kendall MG, Smith BB. The problem of m rankings. *Ann Math Statist.* (1939) 10:275–87. doi: 10.1214/aoms/1177732186
56. Armitage P, Berry G, Matthews JNS. Modelling continuous data. In: *Statistical Methods in Medical Research.* 4th edn. Oxford: John Wiley & Sons, Ltd. (2002). p. 312–77. doi: 10.1002/9780470773666.ch11
57. Oh S-Y, Dieterich M, Lee BN, Boegle R, Kang J-J, Lee N-R, et al. Endolymphatic hydrops in patients with vestibular migraine and concurrent Meniere's disease. *Front. Neurol.* (2021) 12:594481. doi: 10.3389/fneur.2021.594481
58. Fukuoka H, Takumi Y, Tsukada K, Miyagawa M, Oguchi T, Ueda H, et al. Comparison of the diagnostic value of 3 T MRI after intratympanic injection of GBCA, electrocochleography, and the glycerol test in patients with Meniere's disease. *Acta Oto-Laryngol.* (2012) 132:141–5. doi: 10.3109/00016489.2011.635383

59. Naganawa S, Kawai H, Sone M, Nakashima T. Increased sensitivity to low concentration gadolinium contrast by optimized heavily T2-weighted 3D-FLAIR to visualize endolymphatic space. *Magn Reson Med Sci.* (2010) 9:73–80. doi: 10.2463/mrms.9.73
60. Naganawa S. The technical and clinical features of 3D-FLAIR in neuroimaging. *Magn Reson Med Sci.* (2015) 14:93–106. doi: 10.2463/mrms.2014-0132
61. Hirai T, Ando Y, Yamura M, Kitajima M, Hayashida Y, Korogi Y, et al. Transthyretin-related familial amyloid polyneuropathy: evaluation of CSF enhancement on serial T1-weighted and fluid- attenuated inversion recovery images following intravenous contrast administration. *Am J Neuroradiol.* (2005) 26:2043–8.
62. Naganawa S, Komada T, Fukatsu H, Ishigaki T, Takizawa O. Observation of contrast enhancement in the cochlear fluid space of healthy subjects using a 3D-FLAIR sequence at 3 Tesla. *Eur Radiol.* (2006) 16:733–7. doi: 10.1007/s00330-005-0046-8
63. Naganawa S, Suzuki K, Yamazaki M, Sakurai Y. Serial scans in healthy volunteers following intravenous administration of gadoteridol: time course of contrast enhancement in various cranial fluid spaces. *Magn Reson Med Sci.* (2014) 13:7–13. doi: 10.2463/mrms.2013-0056
64. Suzuki H, Teranishi M, Sone M, Yamazaki M, Naganawa S, Nakashima T. Contrast enhancement of the inner ear after intravenous administration of a standard or double dose of gadolinium contrast agents. *Acta Otolaryngol.* (2011) 131:1025–31. doi: 10.3109/00016489.2011.598552
65. Naganawa S, Koshikawa T, Nakamura T, Fukatsu H, Ishigaki T, Aoki I. High-resolution T1-weighted 3D real IR imaging of the temporal bone using triple-dose contrast material. *Eur Radiol.* (2003) 13:2650–8. doi: 10.1007/s00330-003-1922-8
66. Yamazaki M, Naganawa S, Kawai H, Sone M, Nakashima T. Gadolinium distribution in cochlear perilymph: differences between intratympanic and intravenous gadolinium injection. *Neuroradiology.* (2012) 54:1161–9. doi: 10.1007/s00234-012-1078-9
67. Iida T, Teranishi M, Yoshida T, Otake H, Sone M, Kato M, et al. Magnetic resonance imaging of the inner ear after both intratympanic and intravenous gadolinium injections. *Acta Oto-Laryngol.* (2013) 133:434–8. doi: 10.3109/00016489.2012.753640
68. Mamourian AC, Hoopes PJ, Lewis LD. Visualization of intravenously administered contrast material in the CSF on fluid-attenuated inversion-recovery MR images: an *in vitro* and animal-model investigation. *Am J Neuroradiol.* (2000) 21:105–111.
69. Naganawa S, Yamazaki M, Kawai H, Bokura K, Sone M, Nakashima T. Imaging of Ménière's disease by subtraction of MR cisternography from positive perilymph image. *Magn Reson Med Sci.* (2012) 11:303–9. doi: 10.2463/mrms.11.303
70. Naganawa S, Yamazaki M, Kawai H, Bokura K, Sone M, Nakashima T. Imaging of Ménière's disease after intravenous administration of single-dose gadodiamide: utility of multiplication of MR cisternography and HYDROPS image. *Magn Reson Med Sci.* (2013) 12:63–8. doi: 10.2463/mrms.2012-0027
71. Counter SA, Nikkhou-Aski S, Damberg P, Berglin CE, Laurell G. Ultra-high-field (9.4 T) MRI analysis of contrast agent transport across the blood-perilymph barrier and intrastrial fluid-blood barrier in the mouse inner ear. *Otol Neurotol.* (2017) 38:1052–9. doi: 10.1097/MAO.0000000000001458
72. Counter SA. MRI evidence of endolymphatic impermeability to the gadolinium molecule in the in vivo mouse inner ear at 9.4 Tesla. *Open Neuroimag J.* (2013) 7:27–31. doi: 10.2174/1874440001307010027
73. Naganawa S, Yamazaki M, Kawai H, Bokura K, Sone M, Nakashima T. Imaging of Ménière's disease after intravenous administration of single-dose gadodiamide: utility of subtraction images with different inversion time. *Magn Reson Med Sci.* (2012) 11:213–9. doi: 10.2463/mrms.11.213
74. Naganawa S, Kanou M, Ohashi T, Kuno K, Sone M. Simple estimation of the endolymphatic volume ratio after intravenous administration of a single-dose of gadolinium contrast. *Magn Reson Med Sci.* (2016) 15:379–85. doi: 10.2463/mrms.mp.2015-0175
75. Sepahdari AR, Ishiyama G, Vorasubin N, Peng KA, Linetsky M, Ishiyama A. Delayed intravenous contrast-enhanced 3D FLAIR MRI in Meniere's disease: correlation of quantitative measures of endolymphatic hydrops with hearing. *Clinical Imaging.* (2015) 39:26–31. doi: 10.1016/j.clinimag.2014.09.014
76. Kirsch V, Nejatbakhshesfahani F, Ahmadi S-A, Dieterich M, Ertl-Wagner B. A probabilistic atlas of the human inner ear's bony labyrinth enables reliable atlas-based segmentation of the total fluid space. *J Neurol.* (2019) 266(Suppl. 1):52–61. doi: 10.1007/s00415-019-09488-6
77. Ahmadi S-A, Raiser T, Ruehl RM, Flanagin VL, zu Eulenburg P. IE-map: a novel *in-vivo* atlas template of the human inner ear. *Sci Rep.* (2021) 11:3293. doi: 10.1038/s41598-021-82716-0
78. Ito T, Inui H, Miyasaka T, Shiozaki T, Matsuyama S, Yamanaka T, et al. Three-Dimensional magnetic resonance imaging reveals the relationship between the control of vertigo and decreases in endolymphatic hydrops after endolymphatic sac drainage with steroids for Meniere's disease. *Front Neurol.* (2019) 10:46. doi: 10.3389/fneur.2019.00046
79. Shi S, Guo P, Li W, Wang W. Clinical features and endolymphatic hydrops in patients with MRI evidence of hydrops. *Ann Otol Rhinol Laryngol.* (2019) 128:286–92. doi: 10.1177/0003489418819551
80. Shimono M, Teranishi M, Yoshida T, Kato M, Sano R, Otake H, et al. Endolymphatic hydrops revealed by magnetic resonance imaging in patients with acute low-tone sensorineural hearing loss. *Otol Neurotol.* (2013) 34:1241–6. doi: 10.1097/MAO.0b013e3182990e81
81. Attyé A, Eliezer M, Boudiaf N, Tropres I, Chechin D, Schmerber S, et al. MRI of endolymphatic hydrops in patients with Meniere's disease: a case-controlled study with a simplified classification based on saccular morphology. *Eur Radiol.* (2017) 27:3138–46. doi: 10.1007/s00330-016-4701-z
82. Cho YS, Ahn JM, Choi JE, Park HW, Kim Y-K, Kim H-J, et al. Usefulness of intravenous gadolinium inner ear MR imaging in diagnosis of Ménière's disease. *Sci Rep.* (2018) 8:17562. doi: 10.1038/s41598-018-35709-5
83. Hornibrook J, Flook E, Greig S, Babbage M, Goh T, Coates M, et al. MRI inner ear imaging and tone burst electrocochleography in the diagnosis of Ménière's disease. *Otol Neurotol.* (2015) 36:1109–14. doi: 10.1097/MAO.0000000000000782
84. He B, Zhang F, Zheng H, Sun X, Chen J, Chen J, et al. The correlation of a 2D volume-referencing endolymphatic-hydrops grading system with extra-tympanic electrocochleography in patients with definite Ménière's disease. *Front Neurol.* (2021) 11:595038. doi: 10.3389/fneur.2020.595038
85. Gürkov R, Kantner C, Strupp M, Flatz W, Krause E, Ertl-Wagner B. Endolymphatic hydrops in patients with vestibular migraine and auditory symptoms. *Eur Arch Otorhinolaryngol.* (2014) 271:2661–7. doi: 10.1007/s00405-013-2751-2
86. Jerin C, Floerke S, Maxwell R, Gürkov R. Relationship between the extent of endolymphatic hydrops and the severity and fluctuation of audiovestibular symptoms in patients with Menière's disease and MRI evidence of hydrops. *Otol Neurotol.* (2018) 39:e123–30. doi: 10.1097/MAO.0000000000001681
87. Eliezer M, Poillon G, Maquet C, Gillibert A, Horion J, Marie J-P, et al. Sensorineural hearing loss in patients with vestibular schwannoma correlates with the presence of utricular hydrops as diagnosed on heavily T2-weighted MRI. *Diagn Interv Imaging.* (2019) 100:259–68. doi: 10.1016/j.diii.2019.01.006
88. Katayama N, Yamamoto M, Teranishi M, Naganawa S, Nakata S, Sone M, et al. Relationship between endolymphatic hydrops and vestibular-evoked myogenic potential. *Acta Oto-Laryngol.* (2010) 130:917–23. doi: 10.3109/00016480903573187
89. Kato M, Teranishi M, Katayama N, Sone M, Naganawa S, Nakashima T. Association between endolymphatic hydrops as revealed by magnetic resonance imaging and caloric response. *Otol Neurotol.* (2011) 32:1480–5. doi: 10.1097/MAO.0b013e318235568d
90. Zhang W, Hui L, Zhang B, Ren L, Zhu J, Wang F, et al. The correlation between endolymphatic hydrops and clinical features of Meniere disease. *Laryngoscope.* (2020) 131:E144–50. doi: 10.1002/lary.28576
91. Shi S, Guo P, Wang W. Magnetic resonance imaging of Ménière's disease after intravenous administration of gadolinium. *Ann Otol Rhinol Laryngol.* (2018) 127:777–82. doi: 10.1177/0003489418794699
92. Inui H, Sakamoto T, Ito T, Kitahara T. Volumetric measurements of the inner ear in patients with Meniere's disease using three-dimensional magnetic resonance imaging. *Acta Oto-Laryngol.* (2016) 136:888–93. doi: 10.3109/00016489.2016.1168940
93. Naganawa S, Ohashi T, Kanou M, Kuno K, Sone M, Ikeda M. Volume quantification of endolymph after intravenous administration of a single dose of gadolinium contrast agent: comparison of 18- versus

8-minute imaging protocols. *Magn Reson Med Sci.* (2015) 14:257–62. doi: 10.2463/mrms.2014-0118

94. Ito T, Inui H, Miyasaka T, Shiozaki T, Hasukawa A, Yamanaka T, et al. Endolymphatic volume in patients with Meniere's disease and healthy controls: three-dimensional analysis with magnetic resonance imaging. *Laryngoscope Investig Otolaryngol.* (2019) 4:653–8. doi: 10.1002/lio2.313
95. Ito T, Kitahara T, Inui H, Miyasaka T, Kichikawa K, Ota I, et al. Endolymphatic space size in patients with Meniere's disease and healthy controls. *Acta Oto-Laryngol.* (2016) 136:879–82. doi: 10.3109/00016489.2016.1169556
96. Naganawa S, Satake H, Kawamura M, Fukatsu H, Sone M, Nakashima T. Separate visualization of endolymphatic space, perilymphatic space and bone by a single pulse sequence; 3D-inversion recovery imaging utilizing real reconstruction after intratympanic Gd-DTPA administration at 3 Tesla. *Eur Radiol.* (2008) 18:920–4. doi: 10.1007/s00330-008-0854-8
97. Adin ME, Kleinberg L, Vaidya D, Zan E, Mirbagheri S, Yousem DM. Hyperintense dentate nuclei on T1-weighted MRI: relation to repeat gadolinium administration. *Am J Neuroradiol.* (2015) 36:1859–65. doi: 10.3174/ajnr.A4378
98. Barbieri S, Schroeder C, Froehlich JM, Pasch A, Thoeny HC. High signal intensity in dentate nucleus and globus pallidus on unenhanced T1-weighted MR images in three patients with impaired renal function and vascular calcification. *Contrast Media Mol Imaging.* (2016) 11:245–50. doi: 10.1002/cmmi.1683
99. Errante Y, Cirimele V, Mallio CA, Di Lazzaro V, Zobel BB, Quattrocchi CC. Progressive increase of T1 signal intensity of the dentate nucleus on unenhanced magnetic resonance images is associated with cumulative doses of intravenously administered gadodiamide in patients with normal renal function, suggesting dechelation. *Investigat Radiol.* (2014) 49:685–90. doi: 10.1097/RLI.0000000000000072

Conflict of Interest: The authors declare that the research was conducted in the absence of any commercial or financial relationships that could be construed as a potential conflict of interest.

4. Abschließende Bemerkungen und Ausblick

In dieser Arbeit konnte gezeigt werden, warum Innenohr-MRT-Diagnostik mit Darstellung der Flüssigkeitskompartimente im Innenohr bei bestimmten Schwindelsyndromen indiziert ist. Dabei wurde auch auf die Schwierigkeiten der Interpretation der Ergebnisse hingewiesen. Ein untersucherunabhängiger, schneller und verlässlicher Algorithmus, der diese Schwierigkeiten in Bezug auf kontrastmittelverstärkte Darstellung der Innenohr-Flüssigkeitskompartimente adressiert, wurde entwickelt und validiert[1].

Diese neue Methode wurde an einem größeren Datensatz klinischer Daten mit etablierten 2D-Quantifizierungsmethoden verglichen; weiterhin wurden in dieser Arbeit grundsätzliche Aspekte der Innenohrbildgebung analysiert[3]. Die Methode korrelierte stark mit der klinischen Graduierung eines Endolymphhydrops beim MM und war erfreulicherweise unabhängig von Signal-Rausch-Verhältnis und Signalintensität anwendbar.

Basierend auf den Ergebnissen der klinischen Anwendung konnten allgemeine Empfehlungen zur optimalen Bildgebung mittels kontrastmittelunterstützter Innenohr-MRT definiert werden. Wichtig sind neben der applizierten KM-Dosis (0.1-0.2 mmol/kg Körpergewicht) und der ausreichenden Zeit zwischen Applikation und Bildakquise (4h ± 30 min) auch die Verwendung optimaler Sequenzen und der Einsatz einer standardisierten Auswertung. Hier gibt es weiterhin konkurrierende und untereinander begrenzt kompatible, semiquantitative, 2D-schnittbasierte Graduierungs-Methoden, wodurch die Vergleichbarkeit internationaler Studien eingeschränkt wird.

Zum besseren Verständnis des Endolymphhydrops sind sowohl klinische Forschung mit Patient:innen, individuellen Krankheitsverläufen und wenig invasiven Untersuchungsmethoden als auch Grundlagenarbeiten (bspw. am Tiermodell oder i.R. von post-mortem-Untersuchungen) notwendig. Weder der zeitliche Verlauf noch die Pathogenese oder die eigentliche pathophysiologische Relevanz eines erweiterten Endolymphraumes konnte bislang abschließend geklärt werden. Es scheint, wie wir zeigen konnten, einen physiologischen Alterungsprozess mit einer leichten altersabhängigen Erweiterung der Endolymphräume bei einigen Individuen ohne Symptome zu geben[80].

Während die im Rahmen dieser Dissertation beschriebene Methodik einen wertvollen Beitrag zur Vergleichbarkeit und Standardisierung der klinischen MRT-Daten liefert und bereits i.R. internationaler Kollaborationen Anwendung fand [2], sind mittelfristig Next-Generation-MR-Applikationen notwendig, die eine noch höhere räumliche Auflösung bis hin zur tatsächlichen Darstellung der Reißnerschen Membran ermöglichen, eventuell kontrastmittelunabhängig funktionieren [81,82] oder mittels Anwendung neuroinformatischer Technologien wie deep learning, Radiomics oder komplexerer Algorithmen noch weiter automatisierte Auswertungen erlauben, um größere Datensätze zu analysieren.

5. Literaturverzeichnis

1. Gerb J, Ahmadi SA, Kierig E, et al. VOLT: a novel open-source pipeline for automatic segmentation of endolymphatic space in inner ear MRI. J Neurol. 2020;267:185–196.
2. Oh S-Y, Dieterich M, Lee BN, et al. Endolymphatic Hydrops in Patients With Vestibular Migraine and Concurrent Meniere's Disease. Front Neurol. 2021;12:594481.
3. Boegle R, Gerb J, Kierig E, et al. Intravenous Delayed Gadolinium-Enhanced MR Imaging of the Endolymphatic Space: A Methodological Comparative Study. Front Neurol. 2021;12:647296.
4. Ahmadi S-A, Raiser TM, Rühl RM, et al. IE-Map: a novel in-vivo atlas and template of the human inner ear. Sci Rep. 2021;11:3293.
5. Brandt T, Strupp M, Dieterich M. Five keys for diagnosing most vertigo, dizziness, and imbalance syndromes: an expert opinion. J Neurol. 2014;261:229–231.
6. Murdin L, Schilder AGM. Epidemiology of balance symptoms and disorders in the community: a systematic review. Otol Neurotol. 2015;36:387–392.
7. Du Y, Qin H, Liu C, et al. Automatic Measurement of Inner Ear in Different Mammals 1. bioRxiv. 2020:2020.09.30.317941.
8. Nakashima T, Naganawa S, Sugiura M, et al. Visualization of endolymphatic hydrops in patients with Meniere's disease. Laryngoscope. 2007;117:415–420.
9. Ito T, Kitahara T, Inui H, et al. Endolymphatic space size in patients with Meniere's disease and healthy controls. Acta Otolaryngol. 2016;136:879–882.
10. Brandt T, Dieterich M. The vestibular cortex. Its locations, functions, and disorders. Ann N Y Acad Sci. 1999;871:293–312.
11. Felten DL, O'Banion MK, Maida MS. Netter's atlas of neuroscience. Philadelphia, PA: Elsevier; 2016.
12. Guild SR. The circulation of the endolymph. Am J Anat 1927;39:57–81.
13. Nordström CK, Li H, Ladak HM, Agrawal S, et al. A Micro-CT and Synchrotron Imaging Study of the Human Endolymphatic Duct with Special Reference to Endolymph Outflow and Meniere's Disease. Sci Rep. 2020;10:8295.
14. Salt AN, Rask-Andersen H. Responses of the endolymphatic sac to perilymphatic injections and withdrawals: evidence for the presence of a one-way valve. Hear Res. 2004;191:90–100.
15. Athanasiadou D, Jiang W, Reznikov N, et al. Nanostructure of mouse otoconia. J Struct Bio. 2020;210:107489.
16. Bradshaw AP, Curthoys IS, Todd MJ, et al. A mathematical model of human semicircular canal geometry: a new basis for interpreting vestibular physiology. JARO. 2010;11:145–159.
17. Abadie V, Wiener-Vacher S, Morisseau-Durand MP, et al. Vestibular anomalies in CHARGE syndrome: investigations on and consequences for postural development. Eur J Pediatr. 2000;159:569–574.
18. Hurd EA, Micucci JA, Reamer EN, et al. Delayed fusion and altered gene expression contribute to semicircular canal defects in Chd7 deficient mice. Mech Dev. 2012;129:308–323.

19. Barany R. Untersuchungen über den vom Vestibularapparat des Ohres reflektorisch ausgelösten rhythmischen Nystagmus und seine Begleiterscheinungen: ein Beitrag zur Physiologie und Pathologie des Bogengangapparates: Coblentz; 1906.

20. Halmagyi GM, Curthoys IS. A clinical sign of canal paresis. Arch Neurol. 1988;45:737–739.

21. van de Berg R, Rosengren S, Kingma H. Laboratory examinations for the vestibular system. Curr Opin Neurol. 2018;31:111–116.

22. Colebatch JG, Rosengren SM, Welgampola MS. Vestibular-evoked myogenic potentials. Handb Clin Neurol. 2016;137:133–155.

23. Noij KS, Rauch SD. Vestibular Evoked Myogenic Potential (VEMP) Testing for Diagnosis of Superior Semicircular Canal Dehiscence. Front Neurol 2020;11:695.

24. Leigh RJ, Zee DS. The neurology of eye movements, 5th ed. Contemporary neurology series, Vol 70. New York [etc.]: Oxford University Press; op. 2015.

25. Dieterich M, Brandt T. Ocular torsion and tilt of subjective visual vertical are sensitive brainstem signs. Ann Neurol. 1993;33:292–299.

26. Zwergal A, Dieterich M. Vertigo and dizziness in the emergency room. Curr Opin Neurol. 2020;33:117–125.

27. Lopez-Escamez JA, Carey J, Chung W-H, et al. Diagnostic criteria for Menière's disease. J Vestib Res. 2015;25:1–7.

28. Lempert T, Olesen J, Furman J, et al. Vestibular migraine: diagnostic criteria. J Vestib Res. 2012;22:167–172.

29. Dieterich M, Obermann M, Celebisoy N. Vestibular migraine: the most frequent entity of episodic vertigo. J Neurol. 2016;263 Suppl 1:S82-9.

30. Neff BA, Staab JP, Eggers SD, et al. Auditory and vestibular symptoms and chronic subjective dizziness in patients with Ménière's disease, vestibular migraine, and Ménière's disease with concomitant vestibular migraine. Otol Neurotol. 2012;33:1235–1244.

31. Beh SC, Masrour S, Smith SV, et al. The Spectrum of Vestibular Migraine: Clinical Features, Triggers, and Examination Findings. Headache. 2019;59:727–740.

32. Ishiyama G, Lopez IA, Sepahdari AR, et al. Meniere's disease: histopathology, cytochemistry, and imaging. Ann N Y Acad Sci. 2015;1343:49–57.

33. Li H, Rajan GP, Shaw J, et al. A Synchrotron and Micro-CT Study of the Human Endolymphatic Duct System: Is Meniere's Disease Caused by an Acute Endolymph Backflow? Front Surg 2021;8:662530.

34. Lewis RF, Priesol AJ, Nicoucar K, et al. Abnormal motion perception in vestibular migraine. Laryngoscope. 2011;121:1124–1125.

35. Huang T-C, Wang S-J, Kheradmand A. Vestibular migraine: An update on current understanding and future directions. Cephalalgia. 2020;40:107–121.

36. Ashina M, Hansen JM, Do TP, et al. Migraine and the trigeminovascular system—40 years and counting. Lancet Neurol. 2019;18:795–804.

37. Byun YJ, Levy DA, Nguyen SA, et al. Treatment of Vestibular Migraine: A Systematic Review and Meta-analysis. Laryngoscope. 2021;131:186–194.

38. Varkey E, Cider A, Carlsson J, et al. Exercise as migraine prophylaxis: a randomized study using relaxation and topiramate as controls. Cephalalgia. 2011;31:1428–1438.

39. Peikert A, Wilimzig C, Köhne-Volland R. Prophylaxis of migraine with oral magnesium: results from a prospective, multi-center, placebo-controlled and double-blind randomized study. Cephalalgia. 1996;16:257–263.

40. Rosenbaum A, Winter M. ¿Es efectiva la betahistina en la enfermedad de Ménière? Medwave. 2017;17:e7068.

41. Yaz F, Ziylan F, Smeeing DPJ, et al. Intratympanic Treatment in Menière's Disease, Efficacy of Aminoglycosides Versus Corticosteroids in Comparison Studies: A Systematic Review. Otol Neurotol. 2020;41:1–10.

42. Portmann G. The Saccus Endolymphaticus and an Operation for Draining the Same for the Relief of Vertigo. J Laryngol Otol. 1927;42:809–817.

43. Reichmayr C, Sterrer E, Bachtiar A, et al. Tenotomy of the middle ear muscles : An unknown surgical approach in Meniere's disease. Wien Klin Wochenschr. 2019;131:87–91.

44. Baier G, Ott I. Die chirurgische Therapie des M. Menière. Historische Entwicklung und heutiger Stand. HNO. 2008;56:553-64; quiz 565-6.

45. Møller MN, Kirkeby S, Vikeså J, et al. Expression of histamine receptors in the human endolymphatic sac: the molecular rationale for betahistine use in Menieres disease. Eur Arch Otorhinolaryngol. 2016;273:1705–1710.

46. Zingler VC, Cnyrim C, Jahn K, et al. Causative factors and epidemiology of bilateral vestibulopathy in 255 patients. Ann Neurol. 2007;61:524–532.

47. Lauterbur PC. Image formation by induced local interactions. Examples employing nuclear magnetic resonance. 1973. Clin Orthop Relat Res. 1989:3–6.

48. Bottomley PA, Edelstein WA, Leue WM, et al. Head and body imaging by hydrogen nuclear magnetic resonance. J Magn Reson Imaging. 1982;1:69–74.

49. Weinmann HJ, Brasch RC, Press WR, et al. Characteristics of gadolinium-DTPA complex: a potential NMR contrast agent. Am J Roentgenol. 1984;142:619–624.

50. Carr DH, Brown J, Bydder GM, et al. Gadolinium-DTPA as a contrast agent in MRI: initial clinical experience in 20 patients. Am J Roentgenol. 1984;143:215–224.

51. Weishaupt D, Köchli VD, Marincek B, et al. Wie funktioniert MRI?: Eine Einführung in Physik und Funktionsweise der Magnetresonanzbildgebung, 7th ed. Berlin, Heidelberg: Springer Berlin Heidelberg; 2014.

52. Strasilla C, Sychra V. Bildgebende Diagnostik des Vestibularisschwannoms. HNO. 2017; 65:373–380.

53. Pennybacker JB, Cairns H. Results in 130 cases of acoustic neurinoma. J Neurol Neurosurg Psychiatry. 1950;13:272–277.

54. Apicella G, Paolini M, Deantonio L, et al. Radiotherapy for vestibular schwannoma: Review of recent literature results. Rep Pract Oncol Radiother. 2016;21:399–406.

55. Brandt T, Strupp M, Dieterich M. Vestibular paroxysmia: a treatable neurovascular cross-compression syndrome. J Neurol. 2016;263 Suppl 1:S90-6.

56. Kasahara S, Miki Y, Kanagaki M, et al. "Hot cross bun" sign in multiple system atrophy with predominant cerebellar ataxia: a comparison between proton density-weighted imaging and T2-weighted imaging. Eur J Radiol. 2012;81:2848–2852.

57. Choi K-D, Lee H, Kim J-S. Ischemic syndromes causing dizziness and vertigo. Handb Clin Neurol. 2016;137:317–340.

58. Barry RL, Vannesjo SJ, By S, et al. Spinal cord MRI at 7T. NeuroImage. 2018;168:437–451.

59. Kiselev VG. Microstructure with diffusion MRI: what scale we are sensitive to? J Neurosci Methods. 2021;347:108910.

60. Kimitsuki T, Nakagawa T, Hisashi K, et al. Gadolinium blocks mechano-electric transducer current in chick cochlear hair cells. Hear Res. 1996;101:75–80.

61. Nakashima T, Naganawa S, Teranishi M, et al. Endolymphatic hydrops revealed by intravenous gadolinium injection in patients with Ménière's disease. Acta Otolaryngol. 2010;130:338–343.

62. Trune DR. Ion homeostasis in the ear: mechanisms, maladies, and management. Curr Opin Otolaryngol Head Neck Surg . 2010;18:413–419.

63. Pålbrink A-K, Kopietz F, Morén B, et al. Inner ear is a target for insulin signaling and insulin resistance: evidence from mice and auditory HEI-OC1 cells. BMJ Open Diab Res Care. 2020;8:e000820.

64. Frisina RD, Bazard P, Bauer M, et al. Translational implications of the interactions between hormones and age-related hearing loss. Hear Res. 2021;402:108093.

65. Wang P, Yu D, Wang H, et al. Contrast-Enhanced MRI Combined With the Glycerol Test Reveals the Heterogeneous Dynamics of Endolymphatic Hydrops in Patients With Menière's Disease. J Magn Reson Imaging. 2020;52:1066–1073.

66. Lopez-Escamez JA, Attyé A. Systematic review of magnetic resonance imaging for diagnosis of Meniere disease. J Vestib Res. 2019;29:121–129.

67. Baráth K, Schuknecht B, Naldi AM, et al. Detection and grading of endolymphatic hydrops in Menière disease using MR imaging. AJNR Am J Neuroradiol. 2014;35:1387–1392.

68. Gürkov R, Berman A, Dietrich O, et al. MR volumetric assessment of endolymphatic hydrops. Eur Radiol. 2015;25:585–595.

69. van der Lubbe MFJA, Vaidyanathan A, van Rompaey V, et al. The "hype" of hydrops in classifying vestibular disorders: a narrative review. J Neurol. 2020;267:197–211.

70. Chapman CM. Troubleshooting in the histology laboratory. J Histotechn. 2019;42:137–149.

71. Kirsch V, Becker-Bense S, Berman A, et al. Transient endolymphatic hydrops after an attack of vestibular migraine: a longitudinal single case study. J Neurol. 2018;265:51–53.

72. Jerin C, Krause E, Ertl-Wagner B, et al. Longitudinal assessment of endolymphatic hydrops with contrast-enhanced magnetic resonance imaging of the labyrinth. Otol Neurotol. 2014;35:880–883.

73. Manni JJ, Kuijpers W, van Wichem P. Experimental endolymphatic hydrops in the rat. Arch Otolaryngol Head Neck Surg. 1986;112:423–427.

74. Degerman E, Zandt R in 't, Pålbrink A-K, et al. Vasopressin induces endolymphatic hydrops in mouse inner ear, as evaluated with repeated 9.4 T MRI. Hear Res. 2015;330:119–124.

75. Shapiro LG, Stockman GC. Computer vision. Upper Saddle River, NJ: Prentice Hall; 2001.

76. Glasbey CA. An Analysis of Histogram-Based Thresholding Algorithms. CVGIP. 1993;55:532–537.

77. Sankur B. Survey over image thresholding techniques and quantitative performance evaluation. J Electron Imaging. 2004;13:146.

78. Bernsen J. Dynamic thresholding of grey-level images. In: Eighth International Conference on Pattern Recognition. Proceedings; 1986. p. 1251–55.

79. Zou KH, Warfield SK, Bharatha A, et al. Statistical validation of image segmentation quality based on a spatial overlap index. Acad Radiol. 2004;11:178–189.

80. Dieterich M, Hergenroeder T, Boegle R, et al. Endolymphatic space is age-dependent. J Neurol. 2023;270:71–81.

81. Fukutomi H, Hamitouche L, Yamamoto T, et al. Visualization of the saccule and utricle with non-contrast-enhanced FLAIR sequences. Eur Radiol. 2022;32:3532–3540.

82. Simon F, Guichard J-P, Kania R, et al. Saccular measurements in routine MRI can predict hydrops in Menière's disease. Eur Arch Otorhinolaryngol. 2017;274:4113–4120.

Danksagung

Als erstes möchte ich meiner Betreuerin Dr. med. Valerie Kirsch (VK) für die fruchtbare Zusammenarbeit über viele Jahre und die tatkräftige Hilfe in dieser und in anderen Arbeiten danken.

Auch meiner Doktormutter Frau Prof. Marianne Dieterich danke ich, die mich vor allem in den letzten Jahren in neuen, gemeinsamen Forschungsprojekten gefördert hat und deren Rückmeldung und Fachwissen mich auf vielen Ebenen weitergebracht haben, und ohne die der Abschluss dieser Dissertation nicht möglich gewesen wäre.

Für die umfassende Hilfe in allen Teilbereichen der wissenschaftlichen Arbeit danke ich unserer *study nurse* Geraldine Tauber (GT).

Weiterhin möchte ich meiner Familie danken, die mein Studium und meine wissenschaftliche Arbeit immer unterstützt hat, sowie meinen Freunden und Freundinnen.

Lebenslauf

In dieser Version nicht enthalten.